HAL
open science

Transport d'un électron unique dans des nanostructures

Sylvain Hermelin

To cite this version:

Sylvain Hermelin. Transport d'un électron unique dans des nanostructures. Physique [physics]. Université de Grenoble, 2012. Français. NNT : 2012GRENY011 . tel-00721761

HAL Id: tel-00721761

https://theses.hal.science/tel-00721761v1

Submitted on 30 Jul 2012

HAL is a multi-disciplinary open access archive for the deposit and dissemination of scientific research documents, whether they are published or not. The documents may come from teaching and research institutions in France or abroad, or from public or private research centers.

L'archive ouverte pluridisciplinaire **HAL**, est destinée au dépôt et à la diffusion de documents scientifiques de niveau recherche, publiés ou non, émanant des établissements d'enseignement et de recherche français ou étrangers, des laboratoires publics ou privés.

UNIVERSITÉ DE GRENOBLE

THÈSE

Pour obtenir le grade de

DOCTEUR DE L'UNIVERSITÉ DE GRENOBLE

Spécialité : **Physique**

Arrêté ministériel : 7 Août 2006

Présentée par

Sylvain HERMELIN

Thèse dirigée par **Christopher BÄUERLE**
et codirigée par **Tristan MEUNIER**

préparée au sein de l' **Institut NÉEL**
et de l'**école doctorale de Physique de Grenoble**

Transport d'un électron unique dans des nanostructures

Thèse soutenue publiquement le **12 mars 2012**,
devant le jury composé de :

Mr. Christian GLATTLI
Dr., directeur de recherche CEA, SPEC, CEA Saclay, Rapporteur
Mr. Chris FORD
Dr., Cavendish Laboratory, University of Cambridge, Rapporteur
Mr. Frank HEKKING
Pr., Université Joseph Fourier, Examinateur
Mr. Klaus ENSSLIN
Pr., Eidgenössische Technische Hochschule Zürich, Examinateur
Mr Christopher BÄUERLE
Dr., directeur de recherche CNRS, Institut Néel, CNRS, Directeur de thèse
Mr. Tristan MEUNIER
Dr., chargé de recherche CNRS, Institut Néel, CNRS, Co-Directeur de thèse

Contents

List of figures **3**

Notice **9**

Introduction (Français) **11**

Introduction **17**

1 Quantum dots **25**
Résumé 25
Introduction 27
1.1 GaAs heterostructure 27
1.2 Quantum dots 29
1.2.1 Model and characterisation 30
1.2.2 Charge detection 35
1.2.3 Stability diagram 42
1.3 Qubit implementation 44
1.3.1 Single-electron spin qubit 44
1.3.2 Other implementations 55
1.3.3 Three electron spins 57

2 Surface acoustic waves **59**
Résumé 59
Introduction 61
2.1 Description and generation 61
2.2 SAW assisted transport 66
2.3 SAW characterisation 68
2.4 Dynamical quantum dots 71
2.4.1 Spectrum 73
2.4.2 Spin of ensembles of electrons 73
Conclusion 76

3 Experimental setup **77**
Résumé . . . 77
Introduction . . . 79
3.1 Cryogenics . . . 79
3.2 Electronics . . . 82
3.2.1 Voltage sources . . . 83
3.2.2 High frequency generators . . . 83
3.2.3 Measure . . . 84
3.3 Software . . . 85
3.3.1 FPGA code organisation . . . 88
3.3.2 Host-computer software . . . 89

4 On demand single-electron transport **91**
Résumé . . . 91
Introduction . . . 93
4.1 Sample . . . 93
4.2 Few electron regime and tunnelling times . . . 94
4.3 Electron injection . . . 104
4.4 On demand single-electron transport . . . 106
4.5 Note about the spin . . . 111
4.6 Nanosecond triggering . . . 113
4.7 Influence of the SAW parameters . . . 118
Conclusion . . . 121

5 Two-electron transport **123**
Résumé . . . 123
Introduction . . . 125
5.1 Electrons separation 125
5.2 Singlet-triplet relaxation . . . 127
5.3 ... and recombination . . . 137
5.3.1 Theory . . . 137
5.3.2 Technical limitations . . . 140
Conclusion . . . 141

Conclusion and perspectives **143**

Conclusion et perpectives (Français) **147**

References **151**

A Nanofabrication **159**
A.1 Alignment marks . . . 159
A.2 Mesa . . . 160
A.3 Ohmic contacts . . . 160
A.4 Gates . . . 162

A.5 Micro-bonding 162
A.6 Recipes 162

B Article **167**

List of Figures

1 Quantum parallelism 19

1.1 GaAs heterostructure: layers and manipulation principles . . 28
1.2 Band structure of a GaAs heterostructure 29
1.3 Formation of a quantum dot 31
1.4 Scanning electron microscope (SEM) image of the sample . . 31
1.5 Coulomb blockade (principle) 36
1.6 Coulomb blockade and charge detection 36
1.7 Coulomb diamond (schematic) 37
1.8 Coulomb diamond 37
1.9 QPC characteristic (4 K) 38
1.10 QPC plateaus 38
1.11 Model for the QPC 39
1.12 Potential landscape of the QPC 40
1.13 Coulomb blockaded QPC 42
1.14 Stability diagram; last electron. 43
1.15 Single-electron spin readout 45
1.16 Electron spin resonance 49
1.17 Bloch sphere for (S-T_0)-qubit 51
1.18 Energy diagram for an (S-T_0)-qubit 53
1.19 Sample for controlled rotation 56

2.1 Rayleigh wave 62
2.2 SAW generation (principle) 63
2.3 Dynamical dot parabolic approximation 65
2.4 Principle of an acoustoelectric transport experiment 67
2.5 SAW-assisted transport 68
2.6 Reflection of an IDT in a 50 Ω system. 68
2.7 Close-up on the resonance. 69
2.8 Determination of the resonance 70
2.9 SAW broadening of the levels 70
2.10 SAW amplitude calibration 71
2.11 RF signal losses and attenuation 72

2.12 Sample for dynamical quantum dot energy spectrum investigation, Astley *et al.* . . . 74
2.13 Coherent rotation of spin ensembles . . . 74

3.1 Principle of a dilution fridge . . . 80
3.2 Thermal anchoring of electrical lines . . . 81
3.3 SAW excitation gating scheme . . . 84
3.4 SAW signal envelope . . . 85
3.5 SAW signal envelope (details) . . . 86
3.6 FPGA block diagram . . . 87

4.1 SEM image of the sample . . . 94
4.2 Detail of an IDT . . . 95
4.3 Pinch off of the one-dimensional channel . . . 96
4.4 Coulomb diamond of the 1D channel . . . 97
4.5 Stability diagram (schematic) and coupling side . . . 98
4.6 Stability diagrams . . . 99
4.7 Stability diagram (reversed sweep direction) . . . 100
4.8 Injection dot potentail profiles . . . 101
4.9 Expected QPC trace . . . 101
4.10 Metastable charge states scan . . . 102
4.11 Charge state decay . . . 103
4.12 Traces of injection . . . 105
4.13 Metastable charge number tuning . . . 105
4.14 Charge state decay and forced exit . . . 106
4.15 Transfer potential landscape (schematic) . . . 107
4.16 Superposition of electron transfer time traces . . . 108
4.17 Typical time traces . . . 109
4.18 Magnetic field dependence of the resistance . . . 112
4.19 Electronic temperature determination . . . 113
4.20 Nanosecond triggering . . . 114
4.21 Fit on the send events $N_{10\mathrm{xx}}$. . . . 116
4.22 Success rate *vs.* pulse amplitude . . . 116
4.23 Injection potential gradient . . . 117
4.24 Transfer rates *vs.* SAW amplitude . . . 118
4.25 Transfer rates *vs.* SAW duration . . . 119
4.26 Influence of SAW duration and SAW amplitude . . . 120

5.1 Transfer counts for a two-electron dot. . . . 126
5.2 Two electrons transfer/separation *vs.* P_{RF} . . . 127
5.3 Tunnel-rate-read-out principle . . . 128
5.4 Tunnel rate read-out schematic time traces . . . 129
5.5 Singlet *vs.* triplet tunnelling times . . . 130
5.6 Energy dependent tunnelling readout (principle) . . . 131

5.7 Energy-dependent singlet-triplet measurement: exit and reload times . . . 131
5.8 Singlet–triplet readout traces (schematic) . . . 132
5.9 Singlet and triplet sample traces . . . 133
5.10 Signature of spin . . . 134
5.11 Triplet to singlet relaxation time (control) . . . 135
5.12 Triplet to singlet relaxation time . . . 136
5.13 Singlet probability *vs.* separation time . . . 138
5.14 Recombination statistics . . . 139
5.15 Hanbury Brown and Twiss type interferometer . . . 144
5.16 Sample entanglement test . . . 145
5.17 Échantillon pour la réalisation d'expériences d'optique quantique électronique . . . 148
5.18 Échantillon pour le test des inégalité de Bell . . . 149

A.1 Main fabrication techniques . . . 161

Note sur l'organisation du texte

Le lecteur trouvera un résumé en français de chaque chapitre au début de celui-ci. Les chapitres d'introduction et de conclusion sont présentés dans les deux langues dans leur intégralité.

Note on the organisation of the text

The reader will find a French summary of each chapter at the beginning of the corresponding chapter, under the section named "Résumé". The introduction and conclusion chapters will also appear in French respectively before and after their English twins.

Introduction (Français)

Le siècle dernier a vu les physiciens pourchasser les limites de la mécanique quantique. Une part de cet effort provient de la simple curiosité scientifique, une autre de la surprise que chaque étudiant ressent lorsque ses « mystères » lui sont présentés. Cependant, un nouvel objectif a émergé au cours des deux ou trois dernières décades : la démonstration et l'implémentation d'un ordinateur quantique universel. L'idée, d'abord introduite par Feynman en 1982 [1], repose sur le fait qu'une machine capable d'utiliser le parallélisme quantique devrait pouvoir simuler efficacement un système quantique, là où une machine classique souffre un ralentissement exponentiel dû à l'existence de superpositions d'états. D Deutsch poussa l'idée plus loin et démontra que « chaque système physique réalisable de manière finie peut être parfaitement simulé par une machine modèle universelle qui opère par des moyens finis » [2], grâce au parallélisme quantique. Cependant, la preuve est générale et Deutsch n'a pas fourni d'exemples d'algorithmes utiles. Ce manque a été comblé par P.W. Shor qui a décrit des algorithmes pour calculer les logarithmes discrets et factoriser des entiers en nombre premiers en 1994 [3]. Grover a publié un autre algorithme en 1996 [4], lequel permet de chercher plus rapidement dans une base de donnée non triée et en utilisant moins de mémoire que par des moyens classiques. Au cours des dernières années, un quatrième algorithme a été proposé par Harrow et coauteurs qui accélère la résolution de certains systèmes d'équations linéaires. Comparé aux algorithmes classiques — classique ici s'entend au sens « non quantique » — le nombre d'étapes de calcul d'un algorithme quantique peut être diminué de manière significative. Par exemple, la décomposition en facteurs premiers est polynomiale en le nombre de chiffres du nombre à factoriser au lieu d'être exponentiel. Aujourd'hui, les systèmes de cryptographie à clef publique s'appuient sur cette dépendance exponentielle : pour remonter de la clef publique (utilisée pour encoder un message) à la clef privée (celle nécessaire pour décoder le message), il est nécessaire de factoriser la clef publique. Cette factorisation prend aujourd'hui un temps exponentiel en la longueur de la clef. Cette cryptographie repose sur l'incapacité (supposée) de quiconque à réaliser cette factorisation en un temps « court ». La mise en place de l'algorithme de Shor permettrait de casser une large part des transactions sécurisées réalisées à ce jour. Pour implémenter des algorithmes

quantiques, un système de bits quantiques (ou qubits) est nécessaire. Ce sont des système à deux niveaux que l'on peut complètement manipuler de manière cohérente. En d'autres termes, il est nécessaire de pouvoir appliquer au qubit n'importe quelle rotation dans la représentation de la sphère de Bloch [1] et de contrôler les interactions entre deux qubits. Ou encore, il est nécessaire de pouvoir préparer n'importe quelle superposition d'états pour un système à deux niveaux et de pouvoir intriquer deux tels systèmes préalablement préparés.

Nous allons maintenant illustrer comment une telle accélération est possible. Considérons un ordinateur classique. Prenons pour exemple un état en entrée $(a_n a_{n-1} \cdots a_2 a_1)$, où $a_i \in \{0, 1\}$ sont les bits qui composent la donnée et $n \in \mathbb{N}^*$ en est le nombre de bits. La machine applique une série de transformations physiques à cette donnée afin de lui appliquer des opérations logiques. De telles opérations sont appelées « portes ». La séquence exacte de portes appliquées dépend de la tâche que la machine doit accomplir et est appelée « programme ». Une question de première importance pour la mise en œuvre du programme est : combien d'opérations logiques sont nécessaires, en fonction de la longueur de la donnée entrée, pour obtenir le résultat ? Ce nombre est la complexité du programme. Les chercheurs en algorithmique travaillent à trouver de nouvelles façons de traiter des problèmes afin de diminuer leur complexité. La classe des problèmes non-polynomiaux est d'importance, puisque le temps de calcul nécessaire à l'obtention du résultat diverge exponentiellement avec la longueur de l'entrée. Comme nous l'avons déjà évoqué, le problème mathématique de la factorisation d'entiers en nombres premiers, déjà fort ancien, est l'un de ces problèmes. Notons $C(n)$ la complexité du programme que nous considérons. Après $C(n)$ opérations (en moyenne), l'ordinateur fournit la sortie $F(a_n \cdots a_1 a_0) = (f_n(a_n \cdots a_0) \cdots f_1(a_n \cdots a_0))$. Si nous considérons maintenant une machine quantique qui implémente le même programme, nous pouvons lui fournir une entrée beaucoup plus subtile qui utilise la possibilité de superposer des états quantiques. Par exemple, nous pouvons utiliser la superposition de tous les états possibles pour n bits :

$$\begin{aligned} \alpha_{2^n}(1 \cdots 11) &+ \alpha_{2^n-1}(1 \cdots 10) + \cdots \\ &+ \alpha_3(0 \cdots 10) + \alpha_2(0 \cdots 01) + \alpha_1(0 \cdots 00). \end{aligned} \tag{1}$$

Si la machine (quantique) applique le même nombre d'opérations que précédem-

1. Un système à deux niveaux $|\uparrow\rangle$, $|\downarrow\rangle$ peut être placé dans une superposition d'états $\alpha\,|\uparrow\rangle + \beta\,|\downarrow\rangle$ où α et β sont deux complexes tels que $|\alpha|^2 + |\beta|^2 = 1$. Une représentation équivalente d'un tel système est connue sous le nom de sphère de Bloch : le système évolue sur une sphère à 3 dimensions dont les pôles sont $|\uparrow\rangle$ et $|\downarrow\rangle$. Une coordonnée particulière sur la sphère de Bloch — (latitude, longitude) par exemple — correspond à un couple (α, β) donné.

ment, nous obtenons après $C(n)$ opérations l'état sortant :

$$\begin{aligned} \alpha_{2^n} F(1\cdots 11) \quad &+ \quad \alpha_{2^n-1} F(1\cdots 10) + \cdots \\ &+ \quad \alpha_2 F(0\cdots 01) + \alpha_1 F(0\cdots 00). \end{aligned} \tag{2}$$

En d'autres termes, grâce aux propriétés quantiques, le même nombre $C(n)$ d'opérations nous a permis d'appliquer la même fonction F à 2^n états ! Notez cependant que cet exemple n'a pour but que de capturer l'essence du phénomène : nous devons encore prendre en compte quelques limitations... Tout d'abord, la préparation d'une superposition d'états de nombreux qubits est un processus complexe qui ajoutera un nombre d'étapes important. De plus, si nous souhaitons appliquer F à une valeur d'entrée particulière, nous n'avons que faire du résultat pour les autres $2^n - 1$ états. Finalement, la mesure d'un état est destructive : l'état superposé est projeté sur le $i^{\text{ème}}$ état possible du système $(a_n^{(i)} \cdots a_2^{(i)} a_1^{(i)})$ avec la probabilité $|\alpha_i|^2$. Autrement dit, afin de connaître l'état de sortie du système, il faut répéter le calcul un nombre exponentiel de fois. Ces trois remarques expliquent pourquoi seul un nombre limité d'algorithme quantiques existent à ce jour : si le résultat pour une seule valeur d'entrée est souhaitée, l'algorithme doit donner un état mesurable en une seule fois.

Physiquement, toute machine ne peut être un ordinateur quantique. DiVincenzo a proposé un jeu de 5 critères qui doivent être remplis pour qu'un système soit qualifiable d'ordinateur quantique [5]. Ces critères sont les suivants :

un système bien défini l'espace de Hilbert dans lequel évoluent les porteurs de l'information quantique doit être connu avec une grande exactitude ; si l'on considère des systèmes à deux niveaux comme porteur, appelés des qubits, la nature et les propriétés du qubit doivent être définis avec une grande précision.

initialisation il doit être possible de préparer le système quantique dans un état particulier, connu. L'état fondamental est souvent considéré puisque généralement aisé à préparer en refroidissant suffisamment le système.

faible décohérence le système ne doit pas souffrir de décohérence. Un taux de perte d'information est admissible grâce à des codes correcteurs d'erreur. Cependant, au plus la décohérence est faible au plus le temps de calcul sera limité, du fait du surcoût de calcul induit par les codes correcteurs. À ce jour, le taux d'erreur admissible est estimé à 10^{-5} [6], ce qui rend ce critère très strict.

jeu de portes quantique universel il doit être possible d'appliquer des transformations unitaires arbitraires au système et le jeu de de transformations doit également permettre d'intriquer des qubits distincts. Les taux d'erreur de ces transformations doivent bien entendu tomber en dessous du seuil précédemment cité.

mesure forte il est nécessaire de pouvoir réaliser une mesure forte du système. Le résultat d'une telle mesure est une valeur unique, valeur propre d'un opérateur hermitique qui correspond à la mesure effectuée, le système est projeté sur l'état propre correspondant et le système doit enregistrer l'état résultant de chaque qubit avec une grande fiabilité.

Côté expériences, les avancées les plus significatives sont venues de la communauté de la RMN. Cette communauté a été pionnière dans la manipulation des cohérences d'objets quantiques : le spin nucléaire d'atomes et de molécules. Ceci a permis à L. Vandersypen et ses coauteurs [7] d'implémenter pour la première fois l'algorithme de recherche de Grover à un système de 3 qubits en 2000 et d'implémenter l'algorithme de Shor pour la factorisation en 2001 [8]. De dernier travail, le nombre 15 est factorisé en 3×5 en utilisant 7 spins $\frac{1}{2}$ des noyaux d'une molécule. L'avance technologique en RMN permet en effet de manipuler ces spins indépendemment et d'obtenir une calibration fine des couplages entre les spins. Ce dernier point est très important pour maîtriser l'interaction entre les qubits. Cependant, cette expérience clef reste une preuve de concept : comme il a été dit précédemment, l'ordinateur quantique prend tout son intérêt pour des valeurs d'entrée qui sont grandes. Puisque la méthode par RMN s'appuie sur des molécules, l'extensibilité de la méthode pour passer à un grand nombre de qubits est compromise.

Dans un article publié en 1998, Loss et DiVincenzo [9] décrivent un jeu universel de portes à 1 et 2 qubits implémentées par des spins électroniques dans des boîtes quantiques. Un avantage majeur de cette idée tient en son extensibilité : si le principe est démontré expérimentalement, des décades d'expérience et de développement technologique de l'industries de la microélectronique permettront rapidement de produire un ordinateur quantique avec un grand nombre de qubits. Le travail de thèse de doctorat qui suit prend place dans ce contexte. Cette voie de recherche a été très active ces 20 dernières années et toutes les portes logiques nécessaires ont été démontrées pour les qubits de spin. Ceci sera détaillé au cours du chapitre 1. Cependant, les portes à 2 qubits nécessitent à ce jour une grande proximité des deux qubits. Comme il est difficile de concevoir un réseau de boîtes quantiques dans lequel les qubits interagissent deux à deux, une idée alternative prend forme : un réseau de boîtes nettement plus espacées les unes des autres peut être construit et une information transportée d'une boîte à l'autre. Cette information permettra d'intriquer les qubits distants. Cette capacité d'intriquer les qubits est au cœur de la notion d'ordinateur quantique.

Il faut alors trouver une méthode pour passer cette information entre des qubits distants. Un candidat naturel est la lumière, ou des champs électromagnétique en général, puisque celle-ci est connue pour pouvoir transporter de l'information de manière cohérente sur de grandes distances [10]. Puisqu'il est nécessaire que la méthode puissent être mise à l'échelle (en termes de

nombre de qubits), un résonateur sur puce (*onchip*), semble un choix approprié. Le domaine de fréquence typiquement mis en jeu est le GHz. La technologie est connue et les résonateurs peuvent avoir de faible pertes en étant fabriqué à base de supraconducteurs. Le principe qui peut être utilisé pour intriquer deux qubits distants est le suivant. Les deux qubits, A et B, sont placés dans le même résonateur ; le qubit A est préparé dans l'état $|\downarrow\rangle$ par exemple. Le couplage du qubit A à la cavité induit une oscillation cohérente entre le qubit et le résonateur, qui va donc être périodiquement peuplé par un photon. Puisque le qubit B, préparé dans l'état $|\uparrow\rangle$, est également couplé à la cavité, il va osciller de manière cohérente avec celle-ci. Le processus complet permet d'échanger l'état des deux qubits A et B. L'arrêt du processus à mi-chemin de l'échange permet d'intriquer les deux qubits. Cette méthode n'est cependant pas facilement applicable aux qubits de spin : le résonateur permet d'accroître le champ électrique mais le spin n'est que très faiblement couplé à celui-ci. Nous avons donc besoin d'un ingrédient supplémentaire pour coupler le spin au champ électrique. Cet ingrédient est directement disponible dans certains semiconducteurs : l'interaction spin-orbite induit un couplage entre le déplacement des électrons au sein du matériau et leur spin. Le chaînon manquant pour passer du champ électrique au déplacement est fourni par l'interaction Coulombienne. De tels systèmes ont été décrits théoriquement [11] et devraient permettre d'intriquer deux qubits de spin distants de quelques mm en des temps bien inférieurs à leur temps de cohérence. On peut cependant s'attendre à ce que cette méthode présente des limites quant à l'ajustabilité du couplage entre le qubit et le résonateur. Cette propriété est fondamentale afin de pouvoir controler l'interaction entre les qubits.

Comme solution alternative, nous avons envisagé la solution suivante, dont nous pensons qu'elle présente toutes les propriétés requises pour permettre une intrication efficace de qubits distants. L'idée est d'utiliser une particle de même nature que les qubits pour transporter l'information d'un qubit à l'autre. Autrement dit, nous voulons transporter un qubit lui-même. Les électrons sont aisés à transporter : il suffit d'appliquer une polarisation de tension sur une structure conductrice et les électrons sont mis en mouvement. Cependant, pour des qubits, la situation est plus subtile puisque l'information est codée sur un seul spin. De ce fait, nous devons *absolument* empêcher l'électron sur lequel ce précieux élément d'information est codé de se mélanger avec d'autres électrons. Le transport devient alors nettement plus délicat : nous devons transporter un électron donné, bien séparé des autres, d'une position (une boîte quantique) vers une autre position (une autre boîte quantique).

Pendant ma thèse, nous avons exploré la possibilité de transporter un qubit de spin électronique d'une boîte quantique vers une autre, distante de quelques microns. Le premier pas consiste en l'étude du transport d'un seul électron dans des nanostructures. Cette réalisation constitue une étape

majeure : la propagation le long d'un canal unidimensionnel entièrement dépeuplé souffre du phénomène de localisation. Le canal 1D est nécessaire au guidage (de manière analogue à une fibre optique) et à l'isolation de l'électron. Afin de surmonter la localisation, nous utilisons des ondes acoustiques de surface (SAWs pour Surface Acoustic Waves) pour transporter l'électron. De plus, le temps de cohérence d'un spin dans des structures équivalentes à celle utilisée ici est de l'ordre de 10 ns. Le moyen de transport utilisé devra donc remplir un cahier des charges stricte du point de vue des durées : la synchronisation de l'envoi et le transport de l'électron doivent tous deux être inférieurs à 10 ns. De plus, le transport ne doit pas faire perdre sa cohérence au spin électronique. La vitesse des SAWs dans l'AsGa, $3000\,\mathrm{m\,s^{-1}}$, assure un déplacement d'une boîte à l'autre sur des temps de l'ordre de la nanoseconde [12], c'est à dire plus vite que le temps de cohérence du spin. Le confinement de l'électron pendant le transport ainsi que le phénomène de *motional narrowing* protègent le spin de la décohérence pendant son déplacement [13, 14, 15]. Mon travail de thèse, décrit dans le mémoire qui suit, a consisté en l'étude de la première étape vers le transport d'un spin électronique unique : un transport à la demande d'un unique (et de deux) électron(s) a été réalisé. Le transport est obtenu grâce à la partie électrique d'une onde acoustique de surface qui se propage dans l'échantillon.

Ce rapport est organisé de la manière suivante. Dans un premier chapitre, les boîtes quantiques latérales sont décrites. L'état de l'art de la manipulation d'un spin électronique unique dans de telles boîtes est exposé. Dans un second chapitre, les ondes acoustiques de surface utilisées pour transporter l'électron sont introduites. Leurs propriétés et leur génération sont discutées. Ensuite, nous détaillons les recherches précédentes qui ont ouvert le chemin suivi pendant cette thèse. Dans le troisième chapitre, le dispositif expérimental développé pendant ma thèse est décrit. Ensuite, les résultats obtenus sur le transport d'un électron unique sont exposés. Il est montré que le transfert d'un électron d'une boîte à l'autre est effectué avec une grande fiabilité et peut être synchronisé à la nanoseconde, soit plus rapidement que le temps de cohérence du spin. Finalement, un travail sur un dot avec deux électron est présenté. Celui-ci a permis de réaliser des premières mesures sur le spin électronique. La possibilité de transférer un seul des deux électrons est également démontrée. Celle-ci ouvre la voie à la génération de paires d'électrons intriqués.

Sylvain Hermelin, Ph.D. Thesis

Introduction

Over the last century or so, physicists have been chasing the limits of quantum mechanics. Part of this effort comes from simple curiosity, part comes from the surprise any student gets when first introduced to its "mysteries". A new goal arose two to three decades ago. This goal is to implement a universal quantum computer. The idea, first introduced by Feynman in 1982 [1] is that a machine that uses quantum parallelism should be able to efficiently simulate a quantum system, when a classical machine would suffer an exponential slowdown due to the large number of possible superposed states. The idea was pushed further and demonstrated by D. Deutsch who showed that "every finitely realizable physical system can be perfectly simulated by a universal model computing machine operating by finite means" [2], thanks to quantum parallelism. However, the proof is general and Deutsch did not give examples of everyday-use algorithms. This gap has been filled by P.W. Shor who described algorithms for finding discrete logarithms and factoring integers into prime numbers in 1994 [3]. Grover described another algorithm in 1996 [4] that allows to search an unsorted database faster and with a lower memory usage compared to classical means. In recent years, a fourth algorithm has been proposed by Harrow and co-workers to speed up the solving of (some) systems of coupled linear equations [16]. Compared to classical algorithms—classical here means implemented on a classical-mechanics computer—the number of steps for a quantum algorithm can be lowered significantly. For example, the decomposition in prime factors is polynomial in the number of digits of the input instead of exponential. Today, any public-key cryptographic system relies on this exponential behaviour: to go from the public key to the private key, one needs to fully factorise the key, but today, this factorisation takes an exponential time in the number of digits of the key. In other words, for a key of a few hundreds of bits no one is supposed to be able today to factorise the key in a short amount of time—the exact amount of time needed depending on the available computational power. Implementing Shor's algorithm for such a key would allow to break up a huge part of the secured transactions realised today. In order to implement such algorithms, a system of quantum bits or qubits is necessary, *i.e.* quantum-coherent two-level systems, that should be fully transformable: one should be able to apply any rotation in the

Bloch sphere representation of the qubit [2] and control the interactions of two qubits. In other words, it requires to be able to prepare any superposition of states for a two-level system and to be able to entangle two particles previously prepared.

Let us try to illustrate why such an improvement should work. Consider a classical computer. Let its input state be $(a_n a_{n-1} \cdots a_2 a_1)$, where $a_i \in \{0, 1\}$ are the bits composing the input data and $n \in \mathbb{N}^*$ its number of bits. The machine then applies a series of physical transformations to this data in order to compute logical operations on them. Such operations are called gates. The exact sequence of gates applied will depend on the purpose of the machine and is called its program. A very important question for practical purposes is the complexity of a given program: how many logical operations are needed, as a function of the input length, in order to get the result? Researchers in algorithms work hard to find new ways of treating problems that should lower their complexity. The class of non-polynomial problems is particularly at stake since the computational time to get the answer will diverge exponentially with the length of the input. As we said, the old mathematics problem of factoring a number into prime factors is one of them. Let us denote $C(n)$ as the complexity of the program we are considering. After $C(n)$ operations (on average), the computer gives an output $F(a_n \cdots a_1 a_0) = (f_n(a_n \cdots a_0) \cdots f_1(a_n \cdots a_0))$. If we now consider a quantum machine running the same program, we can now input a state that is much more subtle and uses the possibility to superpose quantum states. For example, we can use a superposition of all possible n-qubits states:

$$\begin{aligned} \alpha_{2^n}(1 \cdots 11) \quad &+ \quad \alpha_{2^n-1}(1 \cdots 10) + \cdots \\ &+ \quad \alpha_3(0 \cdots 10) + \alpha_2(0 \cdots 01) + \alpha_1(0 \cdots 00). \end{aligned} \tag{3}$$

If we now apply the same number of operations to these qubits, we get after $C(n)$ operations the output state:

$$\begin{aligned} \alpha_{2^n} F(1 \cdots 11) \quad &+ \quad \alpha_{2^n-1} F(1 \cdots 10) + \cdots \\ &+ \quad \alpha_2 F(0 \cdots 01) + \alpha_1 F(0 \cdots 00). \end{aligned} \tag{4}$$

In other words, thanks to quantum properties, $C(n)$ operations allowed to apply the function F to 2^n states, as schematically summed up in figure 1. Note that this is just to get the grasp of what happens: we should here take into account a few more things ... First, the preparation of such a superposed state is a complex process that will add an overhead to the

2. a two-level system $|\uparrow\rangle$, $|\downarrow\rangle$ can be put in a superposed state $\alpha\,|\uparrow\rangle + \beta\,|\downarrow\rangle$ where α and β are complex numbers such that $|\alpha|^2 + |\beta|^2 = 1$. An equivalent representation of such a system is known as the Bloch sphere: the system evolves on a 3-dimensional sphere whose poles are $|\uparrow\rangle$ and $|\downarrow\rangle$. A given coordinate—(longitude, latitude) for example—of the system on the Bloch sphere corresponds to a given set (α, β). The Bloch sphere representation is commonly used since it is much easier to apprehend than the (α, β)-set of coordinates.

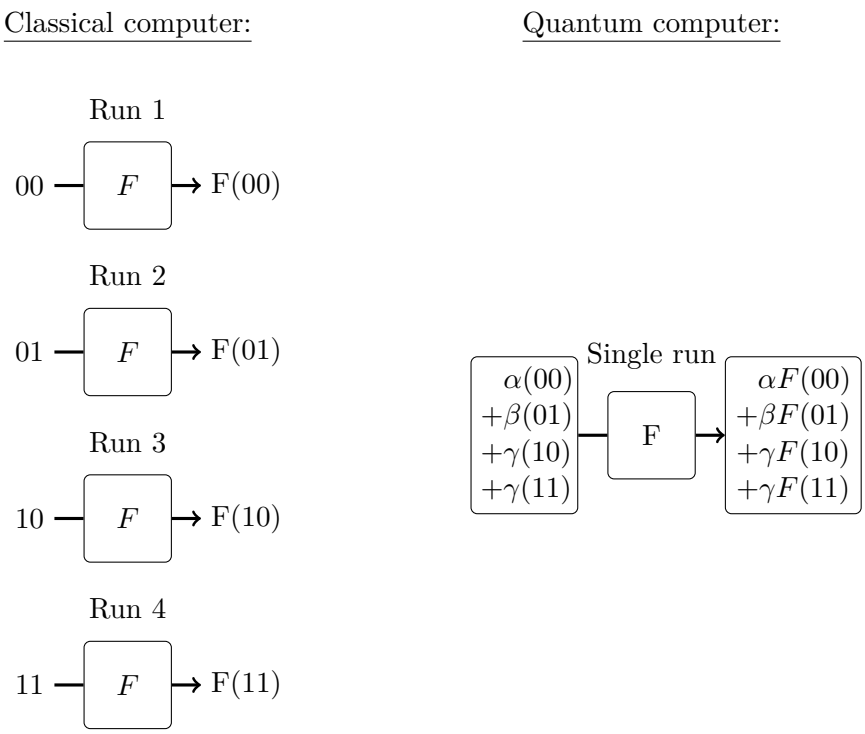

Figure 1: Illustration of quantum parallelism. In the classical case, the program has to be run on each input. In the quantum case, the program can be applied in parallel to all the states of a superposition.

computation. Second, if we want to apply F to a particular input, do we care about the result for the $2^n - 1$ other states? Finally, assuming that we do care, one still has to measure the output state ... and the measure of such a state is so far destructive: the superposed state is projected onto the ith possible state $(a_n^{(i)} \cdots a_2^{(i)} a_1^{(i)})$ with the probability $|\alpha_i|^2$. In other words, in order to get some information out of the output state, one has to repeat the whole process an exponential number of times ... These three remarks are the keys why only a few quantum algorithms exist today: if only the result for one given input state is wanted the algorithm has to give an output state that can be fully known with a *single* measurement.

Physically, any machine cannot be a quantum computer. DiVincenzo proposed a set of 5 criteria that have to be fulfilled by a system in order to qualify for quantum computation [5]. These criteria are the following:

well defined system: the Hilbert space in which will evolve the quantum information carriers has to be known with a very high precision; in other words, if we consider two-level systems as carriers, called qubits, the nature and properties of the qubit have to be defined with high accuracy.

initialisation: it should be possible to prepare the quantum system in a particular state. One often considers the ground state of the system since it should usually be the easiest state that one can prepare with certainty by cooling the system.

low decoherence: the system should not suffer from decoherence. Some amount of information loss is permissible thanks to error correction codes, but the lower the better since error correction consumes computation time. Up to now, the estimated permissible error rate is on the order of 10^{-5} [6], which makes it a very stringent criterion.

universal set of quantum gates: it must be possible to apply perfectly known unitary transformations to the system and the available set of transformations should allow to entangle the different qubits of the system. Once again, the errors on these transformations should fall below the previously stated threshold.

strong measurement: it is necessary to be able to perform a strong measurement to the system. The outcome of such a measurement is the one expected from the quantum mechanics textbook: the system should end up in an eigenstate of a given Hermitian operator and the measuring apparatus should register each of the qubits states with high reliability.

On the experimental side the most significant progress came from the NMR community. They were the first to manipulate the coherence of objects, namely the nuclear spins of atoms and molecules. This allowed L. Vandersypen and co-workers to first implement a three bit quantum search

algorithm in 2000 [7] and to implement Shor's algorithm for factorisation in 2001 [8]. In this work, the number 15 is factorised into 3 and 5 using 7 spin-$\frac{1}{2}$ nuclei of a molecule. The development of NMR indeed allowed to address these spins independently and to have a fine calibration of the couplings between them, which is needed to master the interactions between qubits. However, this key experiment stays a proof of concept: as stated previously the concept of a quantum computer is mostly interesting for large entries! Since the NMR relies on the use of molecules, the scalability of this system seems compromised.

In an article published in 1998, Loss and DiVincenzo [9] described a universal set of one- and two-qubit gates implemented in electron spins in quantum dots. A major advantage of this scheme lies in its scalability: if demonstrated experimentally, decades of technological developments of the microelectronic industry should allow to quickly scale up the quantum computer. The current Ph.D. work takes place in that context. This way of research has been very active in the past 20 years and all the basic gates needed have been proven for spin qubits. This point will be detailed in chapter 1. However, all the two-qubits gates presented to date in lateral quantum dots necessitate the two qubits to be very near to each other. Since it is quite difficult to design an array of dots in which they interact two-by-two, a competing idea arises: an array of qubits much further from each other could be built and some information transported from qubit to qubit in order to entangle the distant qubits. This last point is a key requirement for a quantum computer.

One then has to find a way to entangle distant spin qubits. A natural candidate is light, or electromagnetic fields in general, since it is known to have the ability to transport information quantum coherently on very large distances [10]. Since we want the method to be scalable, we can consider the use of an on-chip resonator. Note that the relevant frequency domain is the radio frequencies, around a few GHz. The technology is well known and can be made with low loss if the resonator is fabricated with a superconducting material. The entangling principle is as follows. Two qubits, A and B, are placed within the resonator (or in its vicinity), qubit A is prepared for instance in the state $|\downarrow\rangle$. The coupling of qubit A to the cavity will induce coherent oscillations between the qubit and the cavity, which will periodically be populated by one photon. Since the qubit B, prepared in state $|\uparrow\rangle$, is coupled to the cavity too, it will coherently oscillate with the cavity when this one is populated. The total process swaps the states of the two qubits. If we now stop midway through the swap, the two qubits end up entangled. This seems promising, except that the coupling from a spin to light is weak and that the onchip resonators are mostly enhancing the electrical component of the electromagnetic field. We hence need an additional ingredient to couple the spin of the electron to the electromagnetic field, preferably to the electric field. This ingredient is readily available

in some semiconductors: the spin-orbit interaction couples the motion of the electrons to their spins. The extra step of coupling the motion to the electric field is taken care of by Coulomb interaction. Such systems have been described theoretically [11] and are expected to be able to entangle two spin qubits a few mm apart on time scales much faster than the coherence time of the qubits. However, this scheme presents limitations in the tunability of the coupling from the cavity to the qubits. This point is fundamental in order to be able to control the interaction between the qubits and to address the different qubits.

As an alternative, we turn towards a direction which, we believe, fulfills all the requirements for an efficient entanglement of distant qubits. The idea is to use a particle of the same nature as the qubit to transport the information from qubit to qubit. In other words, we want to transport a qubit itself. Electrons are easy to transport: just add a voltage bias on the structure and electrons flow. However, for qubits, things get a bit more complicated, since the information is coded onto a single electron. Hence, we *absolutely* do not want the electron on which the precious bit of information is coded to mix with other electrons. The requirements then get more stringent: we need to transport a given electron, protected from mixing with others, from one given place (a specific quantum dot) to another given place (another specific quantum dot).

During my Ph.D. we investigated the possibility to transport a single-electron spin qubit itself from one quantum dot to another quantum dot, micrometers away. The first step lies in the investigation of the transport of a single electron in nanostructures. This alone is a major milestone: the propagation along a depleted one-dimensional channel, needed to address the transported qubit (analogous to optical fibres used in optics), suffers from the localisation phenomenon. In order to overcome localisation, we resort to using surface acoustic waves (SAWs) to transport the electron. In addition, the coherence time for a spin in the types of semiconductor nano-structures used here is on the order of 10 ns. Therefore, the transport mechanism will have to fulfill stringent timing requirements: it should be possible to trigger the transport of the electron faster than 10 ns and the transport mean itself should neither be too slow, nor get the spin to decohere. SAWs propagate at $3000\,\mathrm{m\,s^{-1}}$ in GaAs. This ensures that the electron is dragged from dot to dot—a few microns apart—in a matter of ns [12], that is faster than its spin coherence time. Moreover the electron stays confined during the travel, which enhances the spin coherence length compared to the free displacement case [13, 14, 15]. During my Ph.D. work, described in the following report, we investigated a first step towards the transport of a single-electron spin qubit: an on-demand transport of a single (and two) electron(s) is demonstrated. The transport is realised thanks to a surface acoustic wave propagating through the wafer.

The following report is organised as follows. In the first chapter, lateral

quantum dots will be described. In addition, we will discuss the current state of research in the field of electron-spin qubits based in quantum dots. In the second chapter, the surface acoustic waves we use to transport the electron will be introduced. Their basic properties and generation are discussed. We detail as well previous research that paved the way to this Ph.D. In the following chapter, the experimental setup developed during my Ph.D. will be described. Afterwards, the results obtained on the transport of a single electron will be exposed. These results feature the on-demand transfer of one electron from one dot, that can be electrically selected, to another dot. It is shown that the transfer is highly efficient and triggered on a time scale much below the coherence time usually observed for spin qubits in lateral quantum dots. Finally, some work on two-electron dots and the possibility to transfer one out of two electrons is presented. The former allowed us to do the first measurements of spin in the system. The latter paves the way to the generation of distant entangled particles.

Chapter 1

Spin qubits in lateral quantum dots

Résumé

Dans ce chapitre, nous présentons les boîtes quantiques latérales basées sur des hétérostructures d'arséniure de gallium (la succession des couches d'AsGa, AlAsGa et AlAsGa dopé négativement est présentée figure 1.2). Les variations de bande interdite donnent naissance à un gaz bidimensionnel d'électrons, typiquement 100 nm sous la surface. Ces électrons peuvent être manipulés par l'application de tensions (relativement au potentiel de gaz 2D) sur des grilles métalliques déposées en surface. Une géométrie type de boîte est alors introduite (figure 1.3), à la suite de quoi le modèle à interaction constante est présenté : l'interaction électrostatique avec les réservoirs et les grilles sont modélisés par des capacités constantes et le spectre des états excités est supposé indépendant du nombre d'électrons présents dans la boîte. Ce modèle sert usuellement à décrire les boîtes quantiques et permet de rendre compte du phénomène de blocage de Coulomb, ainsi que des propriétés de remplissage des boîtes. Munis du modèle, nous pouvons décrire les expériences de spectroscopies réalisées sur de telles boîtes (figures 1.7, 1.8), en nous appuyant sur des données expérimentales recueillies durant ma thèse. Celles-ci nous permettent de connaître le couplage des grilles aux électrons et les échelles d'énergie caractéristiques des boîtes utilisées : les énergies de charges sont de l'ordre de 2.5 meV et les états excités sont espacés de quelques centaines de µeV.

Une fois les caractéristiques des boîtes connues, celles-ci sont vidées de leurs électrons. Leur conductance diminuant dans la manœuvre, la technique de détection de charge est mise en place et expliquée (figure 1.6). Celle-ci nous permet de mesurer les diagrammes de stabilité des boîtes et de

montrer que le régime de l'électron unique est atteint (figure 1.14). De plus, la méthode de détection de charge permettra de déterminer l'état de charge des boîtes quantiques de manière non destructive et de manière sûre. Ces deux aspects seront cruciaux pour la réussite de ce travail.

Dans une dernière partie nous décrirons les implémentations de qubits de spin réalisées dans des boîtes latérales. Plus particuliérement, nous expliciterons comment sont réalisées les rotations arbitraires d'un spin électronique unique ainsi que l'échange de deux spins adjacents, ces deux manipulations étant des éléments de base pour la réalisation d'un processeur quantique. L'avancement de la recherche pour différentes technologies — qubit à un seul, deux ou trois spins électroniques — ainsi que leur intérêts et inconvénients sont discutés.

Sylvain Hermelin, Ph.D. Thesis

Introduction

The development of semiconductor technology gave physicists access to a very powerful tool, namely high electron mobility transistors or HEMTs. These structures embed a two-dimensional electron gas or 2DEG, whose density can be tuned during the growth process. In addition, micro fabrication techniques allow one to electrically contact the electrons and to define specific geometries, leading to the emergence of novel properties.

One geometry of interest is the lateral quantum dot, in which a few electrons—one to a few hundred—are isolated from the electronic reservoirs. The electron spin in such a dot has proven to be a good candidate for qubit implementation. We will see in this chapter how such qubits are implemented. First, the heterostructure used will be described. In the second part, we will examine how quantum dots can be realised on such structures and how their properties can be accessed. In the third part, we will discuss the physical implementation of electron spin qubits in quantum dots.

1.1 GaAs heterostructure

The GaAs heterostructures used during my Ph.D. were fabricated by molecular beam epitaxy by our collaborator A.D. Wieck from the Ruhr-University Bochum, Germany. These structures are grown on top of a gallium arsenide (GaAs) wafer. The different layers of GaAs, AlGaAs and silicon-doped AlGaAs of the structure used during my Ph.D. are presented in figure 1.1. This stacking leads to the band structure shown in figure 1.2, that will allow the formation of a two dimensional electron gas 125 nm below the surface. The latter has a mobility of $1.5\times10^6\,\mathrm{cm^2\,V^{-1}\,s^{-1}}$ and a charge density of $1.35\times10^{11}\,\mathrm{cm^{-2}}$, values measured at 4 K in a Hall configuration. Knowing that the 2D density of states for a system is $\rho_{2\mathrm{D}} = \frac{dn_{2\mathrm{D}}}{dE} = \frac{m}{\pi\hbar^2}$, where $\hbar$ is Planck's constant, $n_{2\mathrm{D}}$ the sheet density, $m = 0.067m_\mathrm{e}$ the mass of the particle, m_e the mass of a bare electron and where the spin degeneracy has been taken into account, we obtain the Fermi energy of 4 meV for the 2DEG. This corresponds to a temperature $T_\mathrm{F} = \frac{E_\mathrm{F}}{k_\mathrm{B}} \simeq 40\,\mathrm{K}$. Hence, below 4 K, the 2DEG will behave as a degenerate quantum gas of electrons; in other words, it is a metal. The Fermi wavelength of the electrons is approximately 70 nm. This gives the relevant length scale at which the potential landscape seen by the electrons will have to be modelled in order to see quantum effects appear.

The high mobilities reached by HEMTs are only reachable thanks to the remote-doping technique which consists in placing a spacer layer (40 nm in our case) between the doped layer and the 2DEG plane. Indeed, the potential landscape seen by the electrons of the 2DEG will have irregularities

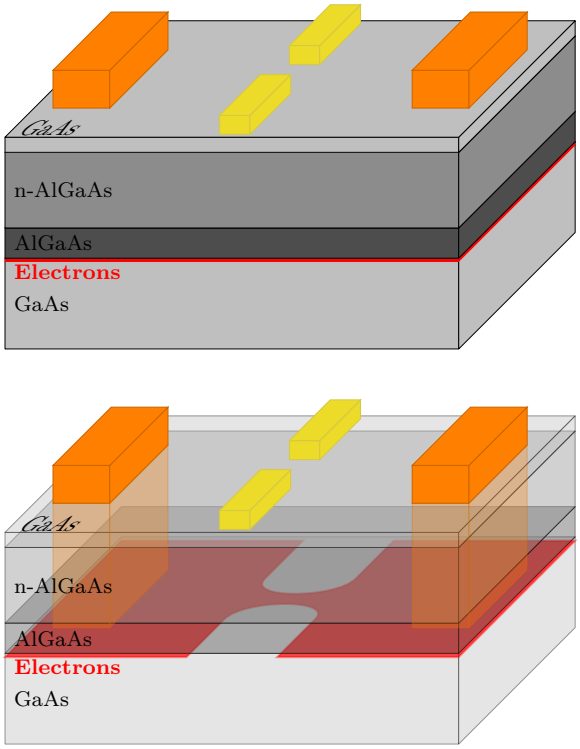

Figure 1.1: Layers of the GaAs heterostructure used for the described work. The layers of the structures are, from bottom to top: 650 nm GaAs, 40 nm spacer layer of aluminium gallium arsenide ($Al_{0.34}Ga_{0.66}As$). The substitution of part of the gallium atoms by aluminium atoms allows to reach a higher band gap than that of GaAs, thus generating the trap in the growth direction to form the 2DEG, while keeping a low lattice mismatch (<0.05 %) with GaAs. 80 nm of silicon-doped (negative doping) $Al_{0.34}Ga_{0.66}As$, providing the electrons for the 2DEG. 5 nm GaAs as capping layer to prevent direct electrical contact from the 2DEG to the metallic gates on top. The metallic gates (yellow) will allow to manipulate the potential profile seen by the electrons. Ohmic contact-pads (orange) allow to circumvent the capping layer and contact electrically the electrons; this will allow to modify the chemical potential of the 2DEG and apply an electrical bias to the 2DEG. The lower panel shows the ohmic contacts and the depletion profile of the electron-gas underneath negatively polarised gates.

coming from the presence of the donors, inducing scattering events. Note that the high mobility is not necessary in itself for the present work. Nevertheless, the low amount of irregularities in the potential of HEMTs—on the order of one every few microns—will be of importance for the dots to be fully tunable, as shall be discussed further. The amount of significant irregularities can be estimated from the measured mobility. Starting from the mobility of the electrons μ, the diffusion coefficient D of the electrons in the metal is obtained from Einstein's relation $\sigma = e^2\rho(E_\mathrm{F})D$, where $\rho = \frac{m}{\pi\hbar^2}$ is the 2D density of states and $\sigma = en_\mathrm{2D}\mu$ the conductivity of the 2DEG, n_2D the sheet density of electrons. We find $D = 0.6\,\mathrm{m^2\,s^{-1}} = 600\,\mathrm{\mu m^2\,ns^{-1}}$. Since a 2D diffusion obeys $L^2 = 2Dt$, where L is the typical distance from the start point after a diffusion time t, we can write $\frac{1}{2}v_\mathrm{F}l_e = D$, where l_e is the mean free path for the electron and v_F is the Fermi velocity. We then get $l_e = 2\frac{D}{v_\mathrm{F}} \simeq 4\,\mathrm{\mu m}$. In other words, there should in average be only one impurity every few microns in the 2DEG. This relatively large distance allows to define micron-sized structures that are free of these defects.

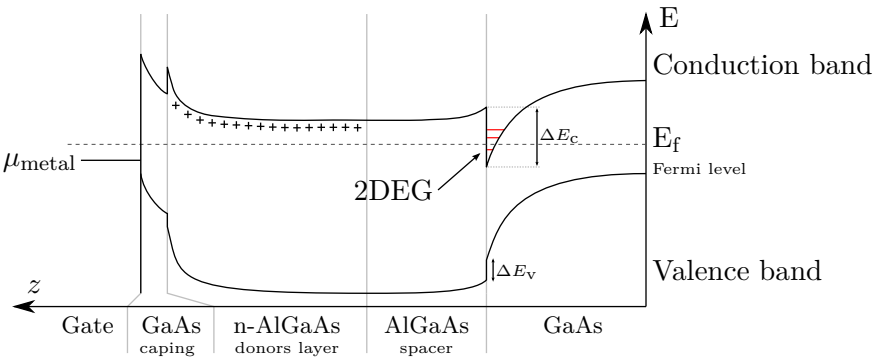

Figure 1.2: Band structure of the GaAs heterostructure. We can see discrete levels with respect to the growth direction (z direction) appear in the conduction band. Placing the Fermi level between the ground and first excited states allows to define an atomically flat 2DEG.

1.2 Quantum dots

A quantum dot can be made in a 2DEG by confining electrons within a small region isolated form electron reservoirs. In order to get the confinement, one has to raise barriers between these. This is achieved by polarising the metallic gates on top of the HEMT. Indeed, a negative voltage applied to the gates with respect to the 2DEG potential will result in a higher electrostatic potential energy for the electrons. Raising this potential higher than the Fermi energy, the electrons underneath the gates get pushed aside and the 2DEG will split into two parts. The typical voltages to be applied

to the gates to get this effect is around $-250\,\mathrm{mV}$ for the wafer used here.[1] The resulting electric field in the structure is on the order of $2 \times 10^6\,\mathrm{V\,m^{-1}}$. It is important to realise that once the 2DEG is split, electrons will still have the possibility to tunnel through the barrier. We remind that the transmission rate for a beam of particles with enery $\frac{\hbar}{2m}\epsilon$ (the zero energy reference corresponds to the potential far from the barrier), modeled by a plane wave of the form $e^{i(kx-\omega t)}$ through a square barrier of height $\frac{\hbar}{2m}U_0$, $U_0 > \epsilon$, and width L is [17]:

$$T = \frac{4\epsilon\,(U_0 - \epsilon)}{4\epsilon\,(U_0 - \epsilon) + U_0^2 \sinh^2 \chi L}, \tag{1.1}$$

$$\chi = \sqrt{U_0 - \epsilon}, \tag{1.2}$$

where $\hbar$ is Planck's constant and m the mass of the particles. For a thick barrier, that is for $\chi L \gg 1$ or $L \gg 10^{-16}\,\mathrm{m}$ for $\frac{\hbar^2}{2m}\,(U_0 - \epsilon) = 1\,\mathrm{meV}$, equation (1.1) can be approximated by an exponential behaviour:

$$T = \frac{8\epsilon\,(U_0 - \epsilon)}{U_0^2} e^{-\chi L}. \tag{1.3}$$

The thick barrier condition should be easily fulfilled since the resolution for the gate design is of the order of 10 nm. As a consequence, we can expect to be able to change the barrier "thickness" on orders of magnitude, as will be discussed further. By having two such barriers around an island of electrons smaller than a micrometer in size, a quantum dot is defined as shown on figure 1.3. The different parameters of the system will be addressed thanks to electrical connections to its different parts. The properties of the quantum dot will be measured in two ways. The first consists in transport measurements through the quantum dot. The second will be conductance measurements of a nearby electrometer.

On the agenda of this work, we will need to determine the charge state of quantum dots. The charge detection method allows to do so in a non destructive way: one can probe the number of charges in the dot, without ejecting them from the dot, which will be needed.

1.2.1 Model and characterisation

A quantum dot can be modelled as electrons trapped in a two dimensional parabolic potential, linked to two reservoirs by tunnel barriers. The characteristics of these barriers as well as the electro-chemical potential of the quantum dot can be tuned by varying the voltages applied on the gates, as we discuss in the following.

1. If one wants to estimate the voltage to be applied from electrostatics considerations, one has to keep in mind that the 2DEG will screen the electric field.

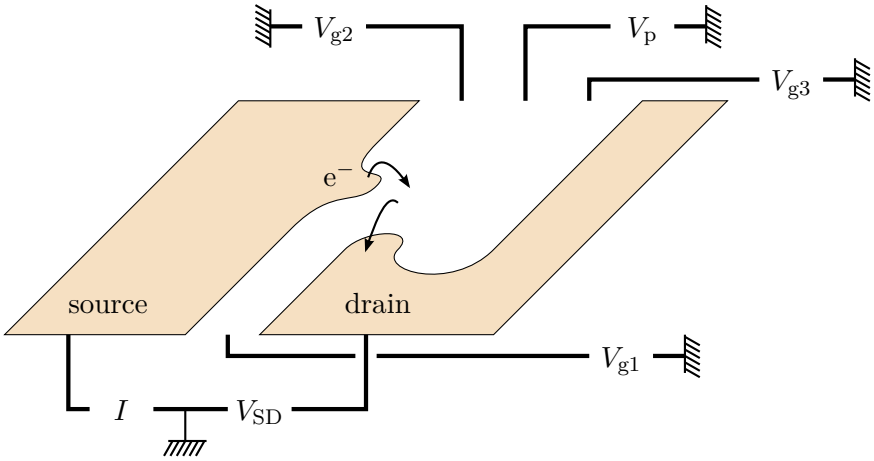

Figure 1.3: Formation of a quantum dot and measurement principle. The 2DEG is split into three parts by the negative voltages applied to the different gates: two reservoirs (source and drain) and the quantum dot in between. The latter is the small island of electrons in the centre and is connected to the reservoirs through tunnel barriers characterised by independent tunnel rates Γ_l and Γ_r. The gates are represented in the plane of the 2DEG for clarity.

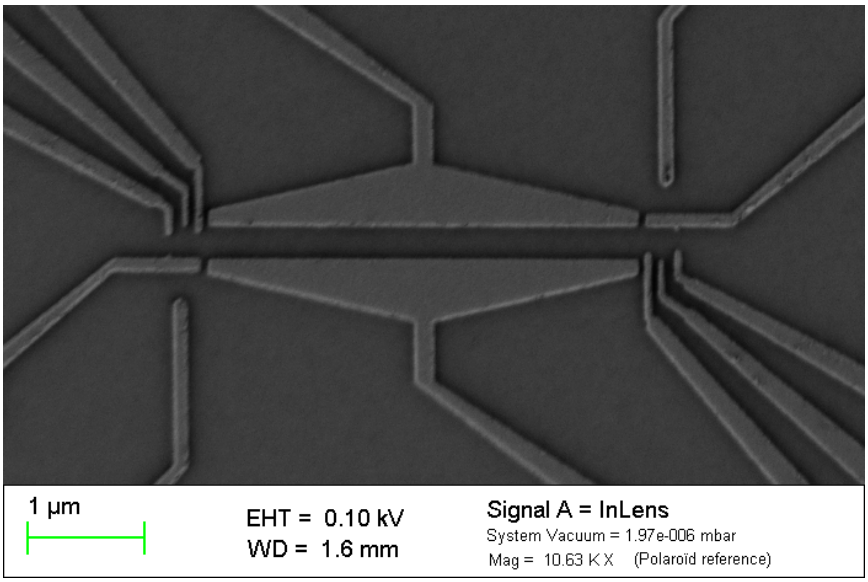

Figure 1.4: SEM image of the sample used during this Ph.D. We can see two quantum dots on the left and right sides linked by a one-dimensional channel. A quantum point contact is attached to each dot.

Constant interaction model

The CI model, commonly used to describe quantum dots, relies on two major hypotheses. First, the Coulomb interaction between the electrons in the dot on one side and the electrons in the reservoirs and the gates on the other side are modelled by a single constant capacitance C. This capacitance is thus the sum $C = C_\mathrm{g} + C_\mathrm{s} + C_\mathrm{d}$, where $C_\mathrm{g} = \sum_i C_\mathrm{gate}^{(i)}$ is the sum of the electrostatic capacitances between the dot and each gate (i), $C_\mathrm{s}(C_\mathrm{d})$ is the capacitance between the dot and the source (drain) reservoir.

Second, the single particle spectrum is independent of the number of electrons present in the dot. Following these assumptions, one can write the energy of the dot filled with N electrons:

$$E(N) = \frac{(-eN + C_\mathrm{g}V_\mathrm{g} + C_s V_\mathrm{s} + C_\mathrm{d}V_\mathrm{d})^2}{2C} + \sum_n E_n(B) \tag{1.4}$$

where a single gate with voltage V_g has been taken into account, V_s and V_d are respectively the source and drain voltage, and $E_n(B)$ are the single particle orbital energies of the trap, the sum running over the N occupied energy levels.

A first estimate of the capacitance C can be gained from a disc of diameter d, for which $C = 4\epsilon_0\epsilon_r d$, where ϵ_0 is the vacuum electrical permittivity, $\epsilon_r \simeq 12.5$ is the relative permittivity of AlGaAs. Assuming a quantum dot that is 20 nm in diameter, we get a capacitance $C \approx 14\,\mathrm{aF}$, which leads to characteristic charging energy for the capacitance $E_\mathrm{C} = \frac{e^2}{C} \approx 25\,\mathrm{meV}$. The same diameter allows to estimate a single particle splitting: the characteristic length in a harmonic oscillator is $\bar{x} = \sqrt{\frac{\hbar}{m^*\omega_0}}$, where $\omega_0 = \frac{E_0(B=0)}{\hbar}$ is the trapping (angular) frequency. We hence get, for a diameter of 20 nm, or $\bar{x} = 10\,\mathrm{nm}$, a trapping energy of $\hbar\omega_0 \simeq 2\,\mathrm{meV}$. The values typically observed experimentally will range from $E_n(B) \approx 10\,\mu\mathrm{eV}$ for very wide dots—more than 1 µm in diameter—to a few meV for small dots on the order of a few tens of nanometres, that is for a lithographic size typically around 200 nm. We remind that a temperature of 100 mK corresponds to a thermal energy $k_\mathrm{B} \times 100\,\mathrm{mK} \simeq 10\,\mu\mathrm{eV}$. Note that the dependences $E_\mathrm{C} \propto \frac{1}{d}$ and $\omega_0 \propto \frac{1}{d^2}$ are (one of) the reasons leading research in molecular or single-atom electronics: the dimensions for the trapping will drop to the nanometre or the Angstöm scale and both the trapping and charging energies can reach the eV range. Remembering that $1\,\mathrm{eV} \Leftrightarrow 10^4\,\mathrm{K}$, equivalent physics should be addressable at much higher temperatures—eventually at room temperature—in these systems compared to lateral dots.

Since the dot is in contact with source and drain reservoirs through tunnel barriers, a better suited physical quantity is the electro-chemical

potential of the dot, which reads:

$$\begin{aligned}\mu(N) &= E(N) - E(N-1) \\ &= E_{\mathrm{C}}\left(N - \frac{1}{2}\right) - \frac{E_{\mathrm{C}}}{e}\left(C_{\mathrm{g}}V_{\mathrm{g}} + C_{\mathrm{s}}V_{\mathrm{s}}\right) + E_N,\end{aligned} \tag{1.5}$$

where $E_{\mathrm{C}} = e^2/C$ is the charging energy of the dot and E_N the energy of the highest occupied single particle level. E_{C} will typically be on the order of a few meV for the dots used here. The drain voltage is kept to ground for simplicity and to reflect the experimental conditions. It immediately follows that by increasing the voltage applied to one of the gates, the chemical potential of the dot is lowered and the occupancy of the dot increased each time the chemical potential gets below the Fermi energy of the reservoirs.

Tunnel barriers

Now that the main properties of a quantum dot have been explained, they have to be measured. This is achieved by applying a voltage bias V_{sd} between source and drain. The bias voltage ranges from $V_{\mathrm{SD}} \simeq 10\,\mu\mathrm{V}$ to $100\,\mu\mathrm{V}$. The induced current is measured, directly giving a measure of the conductance of the device. This current starts from 100 nA when no gates are polarised, which corresponds to a resistance through the sample on the order of $1\,\mathrm{k}\Omega$. This resistance is due to the finite conductivity of the electron sheet and to the resistance of the ohmic contacts. The latter are usually around a few hundreds of ohms at low temperature. Since the resistance of a quantum dot will usually be much higher than $10\,\mathrm{k}\Omega$, the resistance of the ohmic contacts will be neglected in the measurement setup presented in figure 1.3. When polarising the gates that define the quantum dot in the structure, the current drops below 10 nA and oscillations as a function of the gate voltages arises. This phenomenon, known as Coulomb blockade will be detailed further. In such a situation, electrons flow through the dot at a rate of $10^{10}\,\mathrm{s}^{-1}$. Let us consider the dot in the situation pictured in the middle panel of figure 1.5, with a single state within the bias window, this one being occupied by one electron. By considering the tunnel coupling to the reservoir as a perturbation to the dot, we can apply Fermi's golden rule:

$$T_{i\to f} = \frac{2\pi}{\hbar}|\langle f|H'|i\rangle|^2\rho, \tag{1.6}$$

where $T_{i\to f}$ is the transition rate from the state $|i\rangle$ to the state $|f\rangle$, H' is the tunnel coupling term of the Hamiltonian and ρ is the density of final states (here the 2D density $\frac{m}{\pi\hbar^2}$). The electron-flow rate of $10^{10}\,\mathrm{s}^{-1}$ leads to a tunnel coupling of $10^{-12}\,\mathrm{eV}$.[2] By pushing the gates more negative, the current

2. Note that this coupling is from the local state in the quantum dot to an extended state in the lead.

will drop below our detection limit—around 10 fA—that is to say less than $10^5\,\mathrm{e}^-/\mathrm{s}$ or tunnel couplings of $10^{-17}\,\mathrm{eV}$. During our experiments, transition rates down to the second time scale could be measured and transition rates as low as $10^{-2}\,\mathrm{s}^{-1}$ were reported [18]. Such low transition rates bring the tunnel coupling to $10^{-24}\,\mathrm{eV}$. In other words, lateral quantum dots are structures whose coupling to the reservoirs can be continuously tuned in a range of more than 10 orders of magnitude! However, the price to pay is that not all of the dot's parameters will be independent. In other words, getting a dot strongly linked to the reservoirs is easy under the condition of having a large number of electrons in it, but having a single-electron dot with large coupling to the reservoirs is much more challenging.

Spectroscopy

Under the bias conditions cited above, electrons can flow through the dot only if its chemical potential lies in the bias window, as shown in figure 1.5. If now the chemical potential is out of this range, no electron can tunnel into the dot since this would require more energy than available to the system. In addition, no electron can leave the dot since reaching available states in the leads requires more energy than available. The system is then blocked in the N electron state and no current can flow. This phenomenon is known as Coulomb blockade. In order to probe this phenomenon, the temperature of the leads has to be well below the addition energy:

$$E_{\mathrm{add}} = \mu(N+1) - \mu(N) = E_{\mathrm{C}} + \delta_N \tag{1.7}$$

where $\delta_N = E_{N+1} - E_N$ is the energy difference between the highest occupied single particle orbital and the first unoccupied one. Since it is typically on the order of a few milli-electron volts, Coulomb blockade will be reachable by working at temperatures below 1 K. Under this condition and for a bias voltage smaller than the addition energy, peaks in the current through the dot *versus* the gate voltage are expected as can be seen in figure 1.6. Experimentally, the bias voltage will vary from around 100 µV to 10 µV. A smaller bias allows a finer spectroscopy since a larger bias results in a larger measured peak.

In order to measure the energy difference between two peaks, it is necessary to calibrate the lever arm of the gate-to-dot capacitance relatively to the overall capacitance: $\alpha = C_{\mathrm{gate}}/C$. This is achieved by increasing the bias voltage: as can be seen on the rightmost panel of figure 1.5, when the bias window gets wider than the addition energy, a new conduction channel opens and the conductance increases. It follows that $E_{\mathrm{add}} = |E_{\mathrm{F,l}} - E_{\mathrm{F,r}}| = e \times |V_{\mathrm{bias}}|$ and the addition energy is then determined. Moreover, it is possible to resolve excited states of the quantum dot in the same manner: if the bias window is larger than the single particle splitting δ_N, then an electron can flow either through the orbital involved in the ground state

Sylvain Hermelin, Ph.D. Thesis

of the dot or through the next higher energy orbital, again leading to an increase of conductance. All this information can be retrieved from a two-dimensional plot of the differential conductance in the (V_{sd})–$(-V_{\mathrm{gate}})$ plane, called the Coulomb diamond. The expected diagram is shown in figure 1.7 and an experimental diamond in figure 1.8, on which the spectroscopic characteristics of the dot can be determined. Focusing on the diamond around $V_{\mathrm{plunger}} \approx -0.1\,\mathrm{V}$, we find $E_{\mathrm{addition}} \approx 1.5\,\mathrm{meV}$, $\delta \approx 500\,\mu\mathrm{eV}$ and $\alpha \approx 1/25$. As can be seen in figure 1.8, the charging energy of the dot seems to increase quite quickly from diamond to diamond (going from right to left, that is while emptying the dot). This behaviour mostly comes from the design of the quantum dot, whose size changes quickly when it gets emptied. We will then consider these values as lower bounds for E_{addition} and δ. Moreover, the tunnel barriers suffer from the same limitation: their thickness varies very fast with the gate voltage, which makes it very difficult to extract regular Coulomb diamonds.

A major characteristic of the dot that is still to be determined is the absolute number of electrons it contains. We can get a rough idea of what should be this number. Indeed, the electron density can be easily determined from a Hall voltage measurement. This value was determined at 4 K to be $1.35 \times 10^{15}\,\mathrm{m}^{-2}$. If we consider a disc of 150 nm in diameter, corresponding to the lithographic size of the dots, the number of electrons present in the disc is on the order of 150. However, this figure does not hold as a determination of the actual number of electrons in the dot. Moreover, Coulomb peaks only allow to follow the change of charge number: looking at figure 1.5, we can see that the transport spectroscopy is only sensitive to the levels within the bias window. This totally disregard the number of (filled) levels below it (in figure 1.5, N could be 2 or 1000 without any change in the reasoning). The only way to determine the number of charges in the dot is then to push the last electron out of the dot and renumber from there.

1.2.2 Charge detection

Going towards the last electron requires to push the gates more and more negative. As a consequence, the tunnel barriers to the reservoirs get thicker and thicker. When the typical dwell time through the dot will be on the order of 10 µs, then the current through the dot will drop below 10 fA, which is the detection limit of our setup at 1 Hz-bandwidth. It is then impossible to measure the Coulomb peaks down to the last electron,[3] and a workaround has to be implemented.

The commonly used technique relies on the high sensitivity of QPCs (for Quantum Point Contacts) with regard to their electrostatic environment.

3. This affirmation is to be strongly soften since Ciorga and co-authors realised a lateral dot transport spectroscopy in 2000 [19]; nevertheless a special geometry has to be used, which could not fit our spatial requirements.

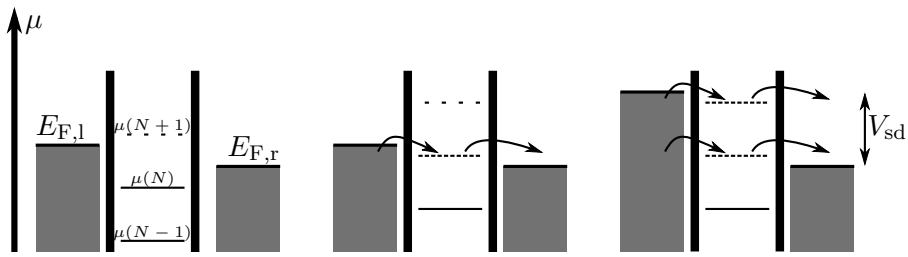

Figure 1.5: Principle of the transport spectroscopy of a quantum dot. Every level that stays below the Fermi level of the reservoirs is filled with one electron. Left: the quantum dot is in the Coulomb blockade regime while no electron of any reservoir has enough energy to enter the dot due to Coulomb interaction and no electron from the dot has enough energy to reach free states of the leads. Center: the chemical potential of the dot is in the bias window, *i.e.* electrons can flow through it. Right: two levels of chemical potential enter the bias window, hence the addition energy can be measured.

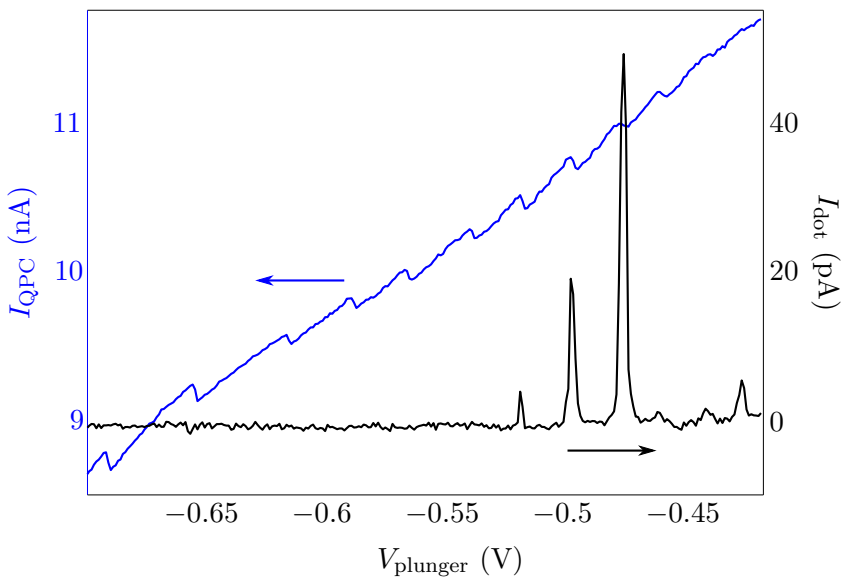

Figure 1.6: Simultaneous measure of Coulomb blockade through the quantum dot (black curve, right axis) and charge detection thanks to the QPC (blue curve, left axis) *versus* the plunger gate voltage. When the latter is too negative, the barriers coupling the dot to the reservoirs get too thick and the current through the dot too low. The charge detection technique allows one to monitor the unloading of the dot in this regime of low dot-conductance.

Sylvain Hermelin, Ph.D. Thesis

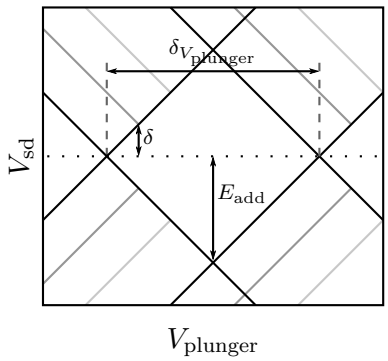

Figure 1.7: Schematic of the differential conductance of a dot *versus* source-drain bias voltage and plunger gate voltage, called the Coulomb diamond. The addition energy E_{add}, single particle splitting δ and lever arm $\alpha = C_{\text{gate}}/C = E_{\text{add}}/\delta V_{\text{plunger}}$ can be determined.

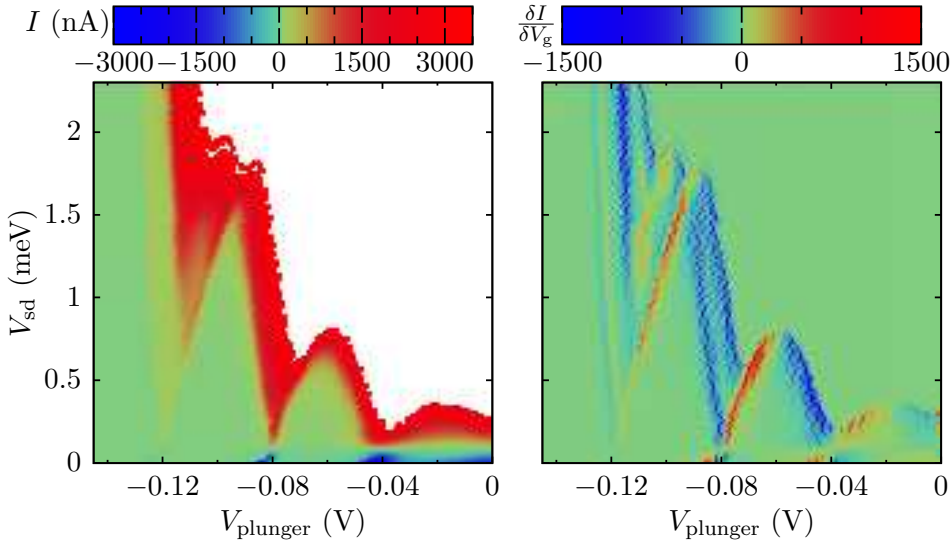

Figure 1.8: Upper half of the Coulomb diamond on the left dot of the sample. Measured current on the left, derivative of the current with respect to the gate voltage on the right. The addition energy $\simeq 1.5$ meV and single particle splitting of around 500 μeV can be measured. It is to be noted that the addition energy increases fast with decreasing number of electrons (that is when V_{plunger} gets more negative). The lever arm $\alpha \simeq 1/25$ is calibrated. An offset of around 100 µV can be seen in the data (left panel, red to blue transition). This offset mostly comes from the current-to-voltage converter that imposes this voltage on its input. The top right region, in white, is constant because of the saturation of the current-to-voltage converter.

For reminders, a QPC is a short one-dimensional channel for the electrons. When the width of such a channel gets comparable to the Fermi wavelength of the electrons, the latter have to flow through the laterally quantised modes of the QPC potential. In such a condition, the QPC shows plateaux of conductance at integer multiple of $\frac{2e^2}{h}$ when varying the depth of the potential; these plateaux correspond to integer numbers of open conducting quantum channels through the QPC [20, 21]. Since the QPC resistance varies fast with respect to the gate voltage between these plateaux, the device is highly sensitive to its electrostatic environment and can be used to monitor a charge variation of a single electron charge in a nearby quantum dot [22].

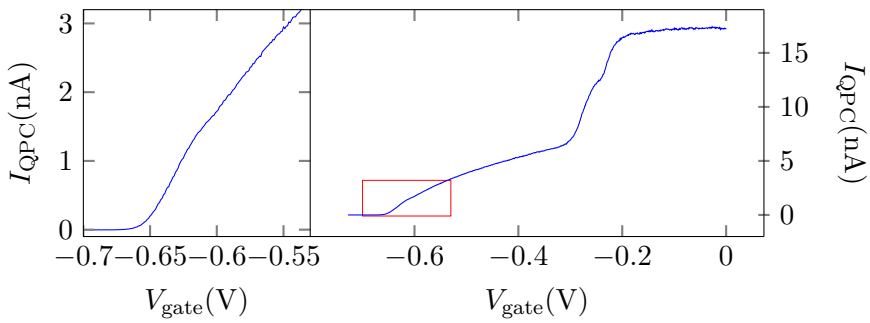

Figure 1.9: QPC scan at 4 K. The two gates defining the QPC are swept simultaneously. The bias voltage was around 30 µV. None of the other gates defining the quantum dot was polarised. The Left panel is a close-up on the red rectangle.

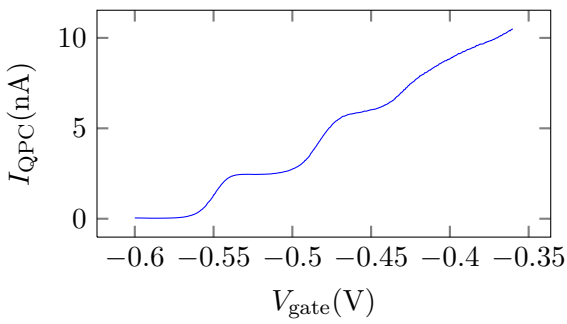

Figure 1.10: QPC conductance plateaux at 100 mK. The bias is around 30 µeV. Data taken at a different cool down, with the dot partially polarised.

The figure 1.9 shows a current-gate voltage characteristic for one of the QPCs. One can see the depletion under the larger parts of the gates around $V_{\mathrm{gate}} = -0.25\,\mathrm{V}$. The constriction gets pinched off around $V_{\mathrm{gate}} = -0.65\,\mathrm{V}$. We can see that at this point, the slope gets more important and the

QPC conductance will get more sensitive to its local electrostatic environment.[4] Note that the steepest part arises around a resistance of $25\,\mathrm{k\Omega} \simeq \frac{h}{e^2}$, which corresponds to a single conducting channel open. The slope around $V_{\mathrm{gate}} = -0.63\,\mathrm{V}$ is of $40\,\mathrm{nA\,V^{-1}}$, for a current of $0.8\,\mathrm{nA}$, that is $5\,\%\,\mathrm{mV^{-1}}$. The characteristic around pinch-off for the same QPC (at a different cool down) is shown in figure 1.10. The dot is now partially polarised. The step from the first plateau to pinch-off has a slope of $120\,\mathrm{nA\,V^{-1}}$ for a current of $1.4\,\mathrm{nA}$, that is $8.5\,\%\,\mathrm{mV^{-1}}$. Note that in the regime between the first plateau, which corresponds to a single conducting channel open and the pinch off, the electrons are tunnelling through the potential barrier. We can see that the sensitivity of the device increases slightly thanks to the lower temperature. We will now estimate the current change induced by an extra electron added to a nearby dot. Consider a QPC formed by the gates depicted figure 1.11. Given a symmetric voltage on both gates V_{gate}, one can

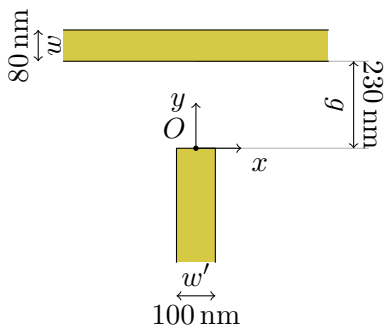

Figure 1.11: Model for the QPC. The top gate will be considered infinitely long and the bottom gate infinite on the lower side. This shape mimics the geometrical shape of our QPCs. The gates are taken infinite to simplify the analytical expressions.

4. Even though the slope is much more important around $V_{\mathrm{gate}} = -0.25\,\mathrm{V}$, it results from a potential change all along the gate: it will not be able to sense an additional charge in the dot, since it applies a local potential shift at the very end of the gate.

compute the potential generated in the 2DEG plane[5] [23]:

$$\begin{aligned}\phi(\vec{r},d) =& \frac{V_{\text{gate}}}{\pi\epsilon_r}\Big[G(x,y-g)+G(-x,y-g)\\ &-G(x,y-g-w)-G(-x,y-g-w) \qquad (1.8a)\\ &+G\left(-y,x+\frac{w'}{2}\right)-G\left(-y,x-\frac{w'}{2}\right)\Big]\\ G(x,y) =& \arctan\left(\frac{d}{R(x,y)-x-y}\right) \qquad (1.8b)\\ R(x,y) =& \sqrt{d^2+x^2+y^2} \qquad (1.8c)\end{aligned}$$

where d is the depth at which lies the 2DEG, G is the response function for an infinite rectangle square gate. The resulting potential is shown in figure 1.12. The potential of the constriction is usually described by a saddle point potential; the symmetry of the problem sets the saddle point at $x_{\text{sp}} = 0$. A numerical study of this potential allows to get $y_{\text{sp}} \simeq 90\,\text{nm}$ and a y-confining harmonic trap of equation:

$$V(y) = \frac{1}{\pi\epsilon}V_{\text{gate}} \times \left(1.6\times10^{-5}y^2+0.37\right), \qquad (1.9)$$

where y is expressed in nm and V in eV, that is a trapping pulsation $\omega_y = 1.2\times10^{12}\,\text{s}^{-1}$, *i.e.* 700 µeV or 7 K for a gates voltage near pinch-off. This explains why the conductance plateaux of figure 1.9 are not yet nicely defined since the data were taken at 4 K.

5. the substrate surface is supposed pinned to 0 V, which makes it much easier to determine the Greens functions for the electrostatic problem and the screening due to the 2DEG is neglected.

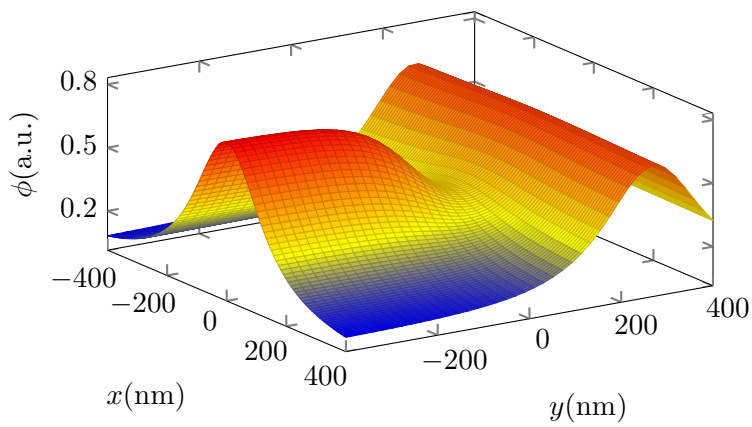

Figure 1.12: Potential landscape giving birth to the QPC. The geometry of the gates is shown in figure 1.11.

We can now estimate the electrostatic sensitivity of the device. Consider the addition of one electron charge in a quantum dot, at a distance $r = 400\,\mathrm{nm}$ from the QPC saddle point. An upper bound to the induced potential shift at the saddle point is:

$$\delta\phi_{e^-} = \frac{-e}{4\pi\epsilon_0\epsilon_r r} = 360\,\mu\mathrm{V}. \tag{1.10}$$

To get the same effect on the QPC, one has to move the gate voltage by up to 10 mV. We can measure from figure 1.9 that the slope of the I-V curve of the QPC around $V_{\mathrm{gate}} = -0.63\,\mathrm{V}$ is $38\,\mathrm{nA\,V^{-1}}$. This means that the current should shift by 380 pA, *i.e.* 38 % when an electron comes in or out of the dot. Since all the previous derivations did not take the screening due to the presence of the gates nor the one due to the 2DEG, we can expect the result to be reduced significantly. This is confirmed experimentally since the conductance changes observed will typically be around 1 %.

The main reason why this technique works lies in the decoupling of the energy scales: the lateral quantisation of the QPC will typically be on the order of a meV and its resistance set around 25 kΩ. In other words, it is possible to bias it up to 1 mV—we typically used 300 µV during our experiment—which allows to measure a current on the order of 10 nA, when the current through the dot is zero. A trace of the current through a QPC while the plunger gate is swept is shown in figure 1.6, on page 36. The QPC conductance jumps each time the system goes through a Coulomb peak, *i.e.* each time a single electron is removed from the dot if the gate is made more negative. It is important to notice that even when the Coulomb peaks cannot be resolved any more, the charge detection is still efficient. This comes from the fact that we measure the current through the QPC whose characteristics are (almost) independent of the parameters of the dot. Note as well that we always start to measure the dot *via* transport through the dot not only because it allows to determine the characteristics of the dot, but also because the charge detection technique does not work for a dot that is too strongly open: the broadening of the levels—or in other words the fluctuations of the charge inside the dot—smear out the jump on the QPC trace, making it impossible to resolve. Another important figure for this scheme to work can be seen from figure 1.6: the change in conductance of the quantum dot is typically 1 %, which means that in order to be clearly measured, the noise level of the system should be much below than a percent. Common current-to-voltage converters allow such a figure, however the noise level we commonly observe with the full setup and the sample usually reaches 0.1 % noise at low frequency. The resulting signal-to-noise ratio is on the order of 10, which should allow to increase the bandwidth of the circuit. Nevertheless, the bandwidth we can reach will be limited due to the current setup of the fridge: the lines connecting the sample to the room temperature present a relatively high capacitance

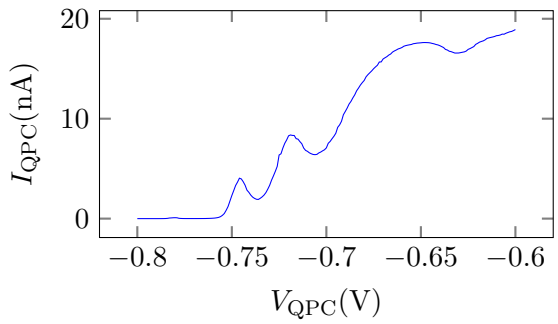

Figure 1.13: QPC response when the dot and channel are polarised. We can see that Coulomb blockade peak appear, most likely due to a minimum in potential between the QPC and the channel-defining gate. V_{QPC} corresponds to the voltage applied on the lower gate of figure 1.11. $T < 100\,\mathrm{mK}$.

of about 2 nF. Hence, the circuit formed by the QPC and the line is a low-pass filter of characteristic time $\tau = R_{\mathrm{QPC}} C_{\mathrm{line}} \simeq 4 \times 10^{-5}\,\mathrm{s}^{-1}$. The current bandwidth limit on the setup actually comes from the current-to-voltage converter that has a bandwidth of 1.4 kHz.

It is to be noted at this point that the design of the sample (see figure 1.4 page 31) made Coulomb blockade features appear in the QPCs once the dots and the channel were formed. A characteristic trace of one QPC under these conditions is presented in figure 1.13. As can be seen on this graph, the sensitivity of the QPC will strongly vary upon the chosen polarisation point. The good news about it is the possibility to achieve higher sensitivities: around $V_{\mathrm{QPC}} = -0.75\,\mathrm{V}$ it can reach $0.55\,\mathrm{nA\,V^{-1}}$, for a current of 2 nA, that is to say a 27 %/mV signal. However, the window on which it can be used is limited to only 2 mV to 3 mV. As a consequence, large gate movements like the ones needed to get the stability diagrams (see next section) will move the QPC out of the right polarisation. We can then polarise it around $V_{\mathrm{QPC}} = -0.69\,\mathrm{V}$, where the sensitivity stays roughly constant over 20 mV (and then falls by one half on the next 10 mV); in compensation, the sensitivity falls to $0.36\,\mathrm{nA\,mV^{-1}}$ for a current of 11 nA, *i.e.* a 3.3 %/mV signal.

1.2.3 Stability diagram

The ability to monitor the change of charge in the quantum dot allows to measure the charge, relative to a reference, in the quantum dot for any point in the configuration space. By plotting the derivative of the QPC conductance *versus* the voltages applied on two gates of the dot, we get lines separating stable charge regions of the dot, as shown in figure 1.14. Hence, each crossing of a line means a change of charge ±e in the dot,

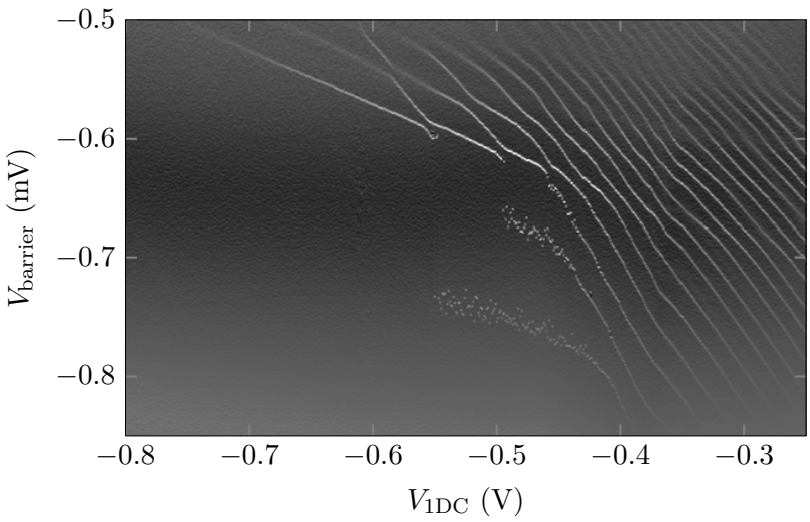

Figure 1.14: Stability diagram of the left dot. The lower left region corresponds to $n = 0$ electron. V_{barrier} is swept towards more negative values at a rate of 3 ms per point. Colour code is the derivative of the QPC current with respect to V_{barrier} (arbitrary units).

emptying it while going to the more negative gate voltages. The stability diagram of figure 1.14 exhibits two main characteristics: a regular set of lines in the top right hand side and the absence of lines in the bottom left hand side. The top right region corresponds to electrons regularly leaving the dot when the gates are pushed more negative, as expected from the model previously stated. In the lower left region however, the QPC still has the same sensitivity and hence a charge tunnelling out of the dot would be witnessed. Therefore, we can say that the last electron has been pushed out of the dot. The absolute number of electrons in the dot is hence zero and can be re-labelled from there. As an immediate consequence, the *stable* charge state of the dot can be measured for any gate voltages values [6].

A parasitic feature of the stability diagram presented in figure 1.14 is the existence of two different slopes for the charge regions. This arises from the shape of the dot's potential: two local minima of the potential exist and therefore the system behaves as a double dot. Nevertheless, the tunnel coupling from one position to the other is strong enough for no sign of separated operation to be to be ed during our experiments. We will therefore consider the system as a single dot.

A very important feature of the stability diagram is the presence of

6. This statement holds only for configurations for which a quantum dot can be defined: if the barriers are too open, the lines will smear-out. It is then possible to switch to transport measurement, but again, at some point, coulomb peaks will get wider than the addition energy.

broken lines around $(-0.5\text{V}, -0.7\text{V})$. The lines appear for a lower V_{barrier} than one would expect. These discontinuities arise from the fact that during the sweep of V_{barrier}, the electron(s) trapped in the dot do not have the time to tunnel out of it for a sweep interval of several tens of millivolts, which corresponds to a few hundreds of milliseconds sweep time. The noise on the line comes from the stochastic nature of the tunnel effect for single particles. In other words, we directly see a region where a metastable charge state can be prepared and live for several tens of milliseconds, which will prove useful later.

1.3 Qubit implementation

In this section, we will discuss some qubit implementations in lateral quantum dots. The first qubit that can be thought of is a charge qubit. The information is for example coded in the charge state of a quantum dot.[7] The major limitation arising in such systems is the short coherence time of the qubit: $\text{T}_2^* = 250\,\text{ps}$ and $\text{T}_2 = 7\,\text{ns}$ times have been measured [24, 25]. The low values of these coherence times is mostly due to charge noise in the system. To implement efficient qubits, a system more immune to charge noise has to be sought. The electron spin in lateral quantum dots has been proposed as being such a system, in addition to the principle for implementing a complete set of quantum gates [9].

1.3.1 Single-electron spin qubit

In such an implementation, the information will be coded onto the spin orientation of a single electron with regard to an external magnetic field. We will follow the common notation $|\uparrow\rangle$ for the ground state of this spin and $|\downarrow\rangle$ for its excited state. The first step towards playing with a spin qubit consists in being able to measure a single electron spin. After that, we need to be able to manipulate it. Last but not least, the coherence time of the spin has to be long enough to earn its rank of qubit.

Readout

Single-shot destructive measurement of a single electron spin in lateral quantum dots has been realised by Elzerman and co-workers in 2004 [26]. The read-out principle is as follows: the quantum dot is polarised in a way such that the electron energy is higher than the Fermi energy of the reservoir E_{F} if its spin is down and less than E_{F} if its spin is up, as depicted in figure 1.15. Considering a reservoir temperature small compared to the Zeeman splitting, *i.e.* $k_{\text{B}}T_{\text{reservoir}} \ll g\mu_{\text{B}}B$, where k_{B} is the Boltzmann constant,

7. one can think of alternate encodings, e.g. coding the information on which excited state the charge lives in.

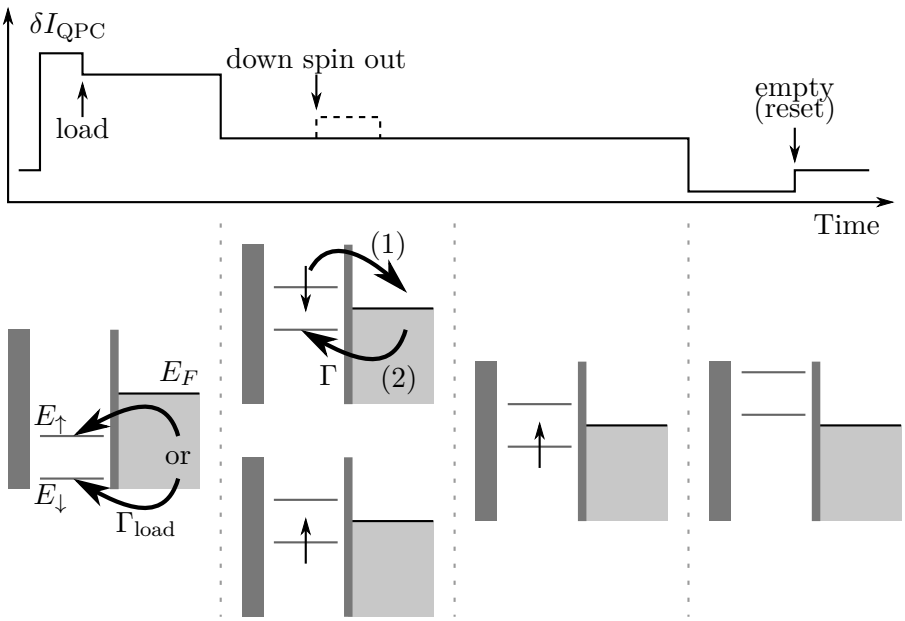

Figure 1.15: Single electron spin readout. The dot is randomly loaded by an up or down spin, then pushed around E_{F} so that only the down spin can tunnel out of the dot. The up spin is blocked in the dot since no states are available in the lead. If loaded with a down spin, the dot empties and loads back with an up spin. The QPC trace picks up the empty charge state of the dot during this process.

$g = -0.44$ the Landé factor for the electron in GaAs and B the external magnetic field applied, which means for a 10 T field as used in [26] an electron temperature below 200 mK is needed. The rules of thumb for these systems are: 25 µeV $\Leftrightarrow$ 1 T and 10 µeV $\Leftrightarrow$ 100 mK. Under this condition and for an up spin, there is no available state in the reservoir and the electron stays in the dot. In contrast, if the spin is down, there are available states and the electron will tunnel out of the dot with the characteristic rate Γ. Once the electron is out, another electron tunnels in with the same rate Γ, with spin up and the dot is blocked. The change in the charge of the dot can be monitored by a nearby QPC and interpreted as the fact that the dot *was* hosting a down-spin electron. To sum up the readout process, we need the two spin states that are to be discriminated to have different energies such that one can be placed above the Fermi level. This results in a spin-to-charge conversion and the change in charge is measured. Of course, the whole readout process has to be performed before the spin has had the time to relax to the ground state and in a time long enough for the measuring setup to pick up the unloading event. In total, we need the ordering $\Gamma_{\text{load}} \gtrsim \Gamma \gg \text{BW} \gg T_1^{-1}$, where BW is the bandwidth of the measurement circuit for which the signal-to-noise ratio stays greater than 1. We will now discuss the main mechanism leading to the relaxation of the spin state.

Relaxation

Thanks to this measurement technique, it is possible to determine the relaxation time T_1 from $|\downarrow\rangle$ to $|\uparrow\rangle$. Indeed, the loading of the dot is random between $|\downarrow\rangle$ and $|\uparrow\rangle$. Hence, for a short enough loading time—*i.e.* $1/\Gamma_{\text{load}} \ll T_1$, where Γ_{load} is the tunnelling rate for the loading position—a down spin can be prepared with probability $\frac{1}{2}$ (and an up spin the other $\frac{1}{2}$ of the times). Then, by adding a variable wait time before measuring the spin state, the probability to find $|\downarrow\rangle$ will decay exponentially with the characteristic time T_1. The authors obtained $T_1 \simeq 0.12$ ms at 14 T, $T_1 \simeq 0.55$ ms at 10 T and $T_1 \simeq 0.85$ ms at 8 T with visibilities up to 65 %.

Similar kinds of experiments in a 1 T parallel magnetic field, allowed to measure T_1 up to 1 s [27] and confirm that the principal cause for spin relaxation in lateral quantum dots in GaAs arises from the cocktail of phonons—both piezoelectric and the deformation potential—plus spin-orbit interaction. Indeed, in the presence of spin-orbit interaction, the eigenstates of the system are perturbed and become, at first order, a superposition of the different orbitals of the trap with different spin states [27]:

$$|\text{g}\uparrow\rangle^{(1)} = |\text{g}\uparrow\rangle \quad + \quad \epsilon_{\text{g}\uparrow}^{(1,x)}|\text{e}^x\downarrow\rangle + \epsilon_{\text{g}\uparrow}^{(1,y)}|\text{e}^y\downarrow\rangle \tag{1.11a}$$

$$|\text{g}\downarrow\rangle^{(1)} = |\text{g}\downarrow\rangle \quad + \quad \epsilon_{\text{g}\downarrow}^{(1,x)}|\text{e}^x\uparrow\rangle + \epsilon_{\text{g}\downarrow}^{(1,y)}|\text{e}^y\uparrow\rangle, \tag{1.11b}$$

where $|\mathrm{g}\uparrow\rangle$ corresponds to a spin up electron in the ground state of the trapping potential and $|\mathrm{e}^x\downarrow\rangle$ to a down spin in the first excited orbital of the trapping potential (the x and y exponents refer to the principal directions of the 2D harmonic trap) and so on. The addition of the piezoelectric phonons is to shake the electrons and hence couple the $|\mathrm{e}\rangle$ and $|\mathrm{g}\rangle$ orbitals, thus coupling the second term of (1.11a) to the first term of (1.11b), and *vice et versa*.

As a consequence, the longitudinal coherence time T_1 will decrease as B^{-5} at low magnetic field [27, 28] and B^{-7} at fields higher than 10 T: the electron has to give the energy $g\mu_\mathrm{B}B$ to the phonon bath and the Fermi golden rule states:

$$\Gamma_{|g\downarrow\rangle^{(1)}\to|g\uparrow\rangle^{(1)}} = \frac{2\pi}{\hbar}\left|\langle g\uparrow|^{(1)}U_\mathrm{ph}|g\downarrow\rangle^{(1)}\right|^2 \times \rho_\mathrm{ph} \tag{1.12a}$$

$$U_\mathrm{ph} \sim \sum_{\vec{q}} \frac{e^{iq_\parallel\vec{r}}}{\sqrt{\omega_{\vec{q}}}}\left(e\beta_{\vec{q}} - iq\Xi_{\vec{q}}\right)\left(b^\dagger_{-\vec{q}} + b_{\vec{q}}\right) \tag{1.12b}$$

where U_ph gives the main dependences of the electron–phonon coupling on the wave vector q and angular frequency $\omega_{\vec{q}}$ of the phonon, $\vec{q}_\parallel$ is the component of $\vec{q}$ parallel to the 2DEG plane, $\beta_{\vec{q}}$ is the piezoelectric potential and $\Xi_{\vec{q}}$ the deformation potential, $\rho_\mathrm{ph} \propto q^2$ the phonon density of states and $b^\dagger_{\vec{q}}$ is the creation operator for a phonon of wave vector $\vec{q}$. We can hence see that the overall behaviour of the decay will be, for the piezoelectric and deformation components respectively:

$$\Gamma_\mathrm{piezo} \propto (\overbrace{q^{-\frac{1}{2}}}^{\text{(a)}} \cdot \overbrace{q}^{\text{(b)}} \cdot E_\mathrm{z})^2 \cdot \overbrace{q^2}^{\text{(c)}} \tag{1.13a}$$

$$\Gamma_\mathrm{deformation} \propto (\underbrace{q^{-\frac{1}{2}}}_{\text{(a)}} \cdot \underbrace{q}_{\text{(b)}} \cdot \underbrace{q}_{\text{(d)}} \cdot E_\mathrm{z})^2 \cdot \underbrace{q^2}_{\text{(c)}} \tag{1.13b}$$

where the factor (a) comes from the square root of ω in U_ph, (b) is a q–dot size matching factor that comes from the $e^{i\vec{q}\cdot\vec{r}}$ term of U_ph, E_z is the Zeeman energy that enters into the coefficients $\epsilon^{(1)}_{g\updownarrow}$ and (c) comes from the density of states of phonons. The factor (d) is the "extra" q in front of Ξ in U_ph. In the end, we find $\Gamma \propto B^5$ for fields less than 10 T and $\Gamma \propto B^7$ for higher fields.

The theoretical prediction from Golovach, Khaetskii and Loss in 2004 [28] goes further and states that the coherence time T_2—time during which a superposition of states survives—of such qubits should not suffer further limitations than the absolute limit $T_2 < 2T_1$. Following this lead, several research groups focused on the realisation of qubit gates and read-out schemes with such a system.

Spin manipulation: theoretical approach

As stated in DiVincenzo's criteria, a universal set of quantum gates has to be applicable to the qubits. The basics to get such a set are the control of a single qubit and the ability to get two qubits to interact fully coherently. These abilities correspond to being able to apply any arbitrary rotation (in the Bloch sphere) to a single qubit and to be able to entangle two qubits.

For reminders, a qubit is a two-level system, commonly denoted $|\uparrow\rangle$ and $|\downarrow\rangle$. The qubit $|\mathrm{qb}\rangle$ can live in a superposition of the two states:

$$\begin{aligned} |\mathrm{qb}\rangle = \alpha\,|\uparrow\rangle + \beta\,|\downarrow\rangle \qquad & (\alpha,\beta) \in \mathbb{C}^2 \\ & |\alpha|^2 + |\beta|^2 = 1. \end{aligned} \tag{1.14}$$

Note that such states are called "pure states", by opposition to statistical mixtures in which the system is in *one of* the states $|\uparrow\rangle$ or $|\downarrow\rangle$ with their respective probability. The condition $|\alpha|^2+|\beta|^2 = 1$ allows to have a bijective transformation to a simpler space: a sphere. Hence, the state of $|\mathrm{qb}\rangle$ is commonly represented as a point on the Bloch sphere or, equivalently, as the vector going from the origin to this point. The poles of the sphere correspond to the states $|\uparrow\rangle$ and $|\downarrow\rangle$, their axis being usually taken as the z-axis. The rotations around the x-, y- and z-axes are generated by the Pauli matrices σ_x, σ_y and σ_z:

$$\sigma_x = \begin{pmatrix} 0 & 1 \\ 1 & 0 \end{pmatrix}, \qquad \sigma_y = \begin{pmatrix} 0 & -i \\ i & 0 \end{pmatrix}, \qquad \sigma_z = \begin{pmatrix} 1 & 0 \\ 0 & -1 \end{pmatrix}, \tag{1.15}$$

in the basis ($|\uparrow\rangle$,$|\downarrow\rangle$). In order to realise an arbitrary rotation in the Bloch sphere, which is necessary to implement a quantum computer, it is necessary to be able to apply controlled rotations in at least two non-collinear directions—accessing all points on a surface requires only two independent parameters.

For a single electron spin, the rotation around the z-axis is generated by the Zeeman term $E_\mathrm{z} = g\mu_\mathrm{B}B$, which corresponds to a rotation rate of $40 \times 10^9\,\mathrm{rad\,s^{-1}\,T^{-1}}$. This allows for $B = 100\,\mathrm{mT}$ to get a π-rotation in $800\,\mathrm{ps}$. The rotation around the x-axis is more tricky to achieve, but its principle is known: one has to use electron spin resonance (ESR), that is by shining a rotating magnetic field in the (x, y)-plane, at Larmor's frequency $f_\mathrm{L} = \omega_\mathrm{L}/2\pi = g\mu_\mathrm{B}B_\mathrm{z}/h$. The resulting Hamiltonian reads:

$$H = \frac{1}{2}g\mu_\mathrm{B}\,(B_z\sigma_z) + \frac{1}{2}g\mu_\mathrm{B}\vec{B}_\perp \cdot (\sigma_x\vec{e}_x + \sigma_y\vec{e}_y) \tag{1.16a}$$

$$\vec{B}_\perp = B_\perp \times (\cos(\omega_\mathrm{L}t)\vec{e}_x + \sin(\omega_\mathrm{L}t)\vec{e}_y)\,, \tag{1.16b}$$

where we only treat the spin part of the system. Assuming $|B_\perp| \ll |B_z|$, we can get the hint that the system is "mostly" rotating around z. Thus, by

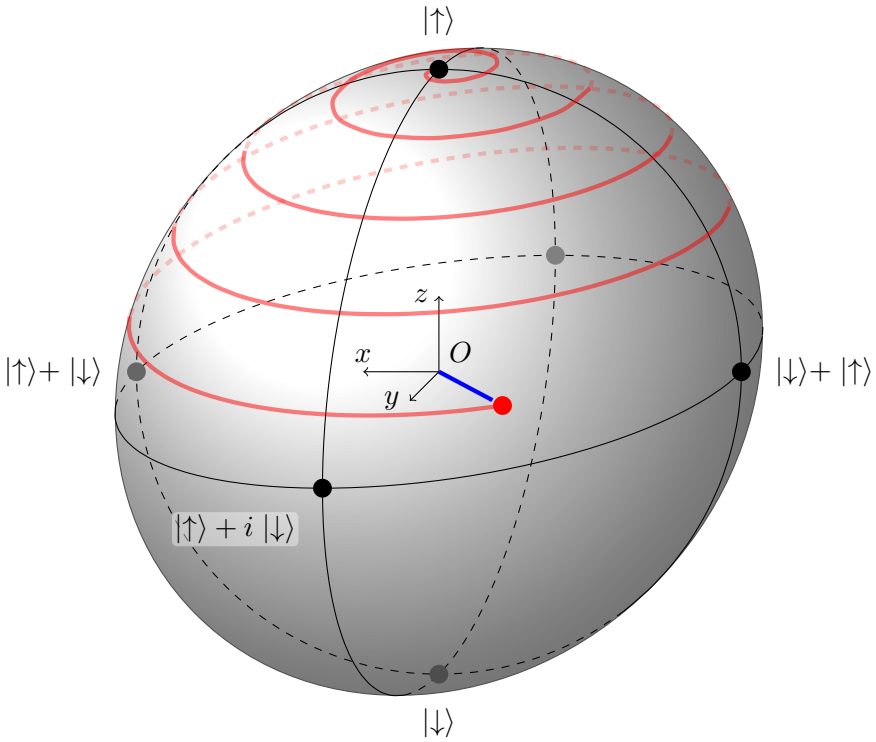

Figure 1.16: Bloch sphere of a single spin and ESR trajectory of the spin, starting from $|\uparrow\rangle$, with $B_z = 20B_\perp$. We can see that the electron-spin (red line) goes "slowly" but surely towards the $|\downarrow\rangle$ state.

going into the rotating frame:

$$\vec{e}_{x'} = \cos(\omega_\mathrm{L} t)\vec{e}_x + \sin(\omega_\mathrm{L} t)\vec{e}_y, \qquad \vec{e}_{y'} = \vec{e}_z \times \vec{e}_{x'}, \qquad \vec{e}_{z'} = \vec{e}_z, \tag{1.17}$$

we get the Hamiltonian:

$$H' = \frac{1}{2} g\mu_\mathrm{B}\sigma_x B_\perp. \tag{1.18}$$

from which we see that the state slowly rotates at the frequency $f = \frac{g\mu_\mathrm{B}B_\perp}{h}$ around the x'-axis (but keep in mind that the x'-axis is rotating around $\vec{e}_z$!). It is to be noted that the treatment holds for $B_\perp$ not small compared to B_z. A sample trajectory in the Bloch sphere is shown in figure 1.16. Considering an initial state $|\mathrm{qb}\rangle = |\uparrow\rangle$, the probability to end up in the $|\downarrow\rangle$ state is:

$$P_{|\uparrow\rangle\to|\downarrow\rangle} = \sin^2\left(\frac{g\mu_\mathrm{B}B_\perp t}{\hbar}\right). \tag{1.19}$$

In other words, the probability to *measure* the state $|\downarrow\rangle$ after a time t oscillates in time, with the frequency:

$$f_\mathrm{Rabi} = 2\frac{g\mu_\mathrm{B}B_\perp}{h}. \tag{1.20}$$

These oscillations are known as "Rabi oscillations" and are a signature of coherent evolution. Note that their frequency scales linearly with the oscillating field amplitude and that the resonance condition $f_{B_\perp} = f_{\mathrm{L}}$ for the rotating magnetic field scales linearly with the field B_z. We can remark that by turning off the oscillating field after time $\tau_\pi = \frac{1}{f_{\mathrm{Rabi}}}$, we can invert the spin state, *i.e.* $|\uparrow\rangle \mapsto |\downarrow\rangle$ and $|\downarrow\rangle \mapsto |\uparrow\rangle$. By turning it off at $\tau_{\pi/2} = \frac{1}{2f_{\mathrm{Rabi}}}$, we can prepare a superposition of states with a definite phase:

$$|\uparrow\rangle \mapsto |\uparrow\rangle + i\,|\downarrow\rangle \tag{1.21a}$$

$$|\uparrow\rangle \mapsto |\uparrow\rangle + \;\;|\downarrow\rangle \tag{1.21b}$$

for a $\frac{\pi}{2}$-rotation around the x-axis and the y-axis, respectively.

Regarding the two-qubit gates, the two gates people usually try to implement are the "C-NOT" gate and "$\sqrt{\mathrm{SWAP}}$" gates. Let us first consider the C-NOT gate. It aims at getting the negation of a target qubit if the control qubit is, say, $|\uparrow\rangle$, and the identity of the target qubit if the control is $|\downarrow\rangle$. This requirement only describes a classical C-NOT gate so far. For the gate to be efficient for a quantum computer, this must hold for qubits as inputs, that is for superpositions of the states $|\uparrow\rangle$ and $|\downarrow\rangle$ for the two qubits. That is to say, if we have the control and target qubits $|\mathrm{qb}\rangle_{\mathrm{C}} = \alpha|\uparrow\rangle + \beta|\downarrow\rangle$ and $|\mathrm{qb}\rangle_{\mathrm{T}} = \gamma|\uparrow\rangle + \delta|\downarrow\rangle$, the gate result should be:

$$\begin{aligned}(\alpha|\uparrow\rangle + \beta|\downarrow\rangle) \otimes (\gamma|\uparrow\rangle + \delta|\downarrow\rangle) \quad \mapsto \quad & \alpha|\uparrow\rangle \otimes (\gamma|\downarrow\rangle + \delta|\uparrow\rangle) \\ & +\beta|\downarrow\rangle \otimes (\gamma|\uparrow\rangle + \delta|\downarrow\rangle)\,,\end{aligned} \tag{1.22}$$

where the system composed of an $|\uparrow\rangle$ control and $|\downarrow\rangle$ target is noted $|\uparrow\rangle \otimes |\downarrow\rangle$.

The other gate, $\sqrt{\mathrm{SWAP}}$, consists in stopping midway through a SWAP gate, which is the exchange of the two qubits. To image this, let us consider a Bloch sphere with z-axis pointing towards the singlet state $S = |\uparrow\downarrow\rangle - |\downarrow\uparrow\rangle$, x-axis pointing towards $|\uparrow\downarrow\rangle$ and then y-axis towards $S + iT_0$, where $T_0 = |\uparrow\downarrow\rangle + |\downarrow\uparrow\rangle$, as can be seen in figure 1.17. The $T_+ = |\uparrow\uparrow\rangle$ and $T_- = |\downarrow\downarrow\rangle$ states can be easily detuned away from the S, T_0 system by applying an external magnetic field. By applying a π-rotation around the z-axis—which can be controlled by the exchange interaction between the two electrons—we can see that:

$$|\uparrow\downarrow\rangle \mapsto |\downarrow\uparrow\rangle \tag{1.23a}$$

$$|\downarrow\uparrow\rangle \mapsto |\uparrow\downarrow\rangle \tag{1.23b}$$

which correspond to the mappings of a SWAP gate. It is then possible by stopping halfway through the gate to obtain the $\sqrt{\mathrm{SWAP}}$ mapping:

$$|\uparrow\rangle \otimes |\downarrow\rangle \mapsto \frac{1}{2}\Big((1+i)|\uparrow\rangle \otimes |\downarrow\rangle + (i-1)|\downarrow\rangle \otimes |\uparrow\rangle\Big)\,, \tag{1.24}$$

and *vice versa*. In the end, the goal of the two-qubit gates is to *entangle* different qubits of the computer.

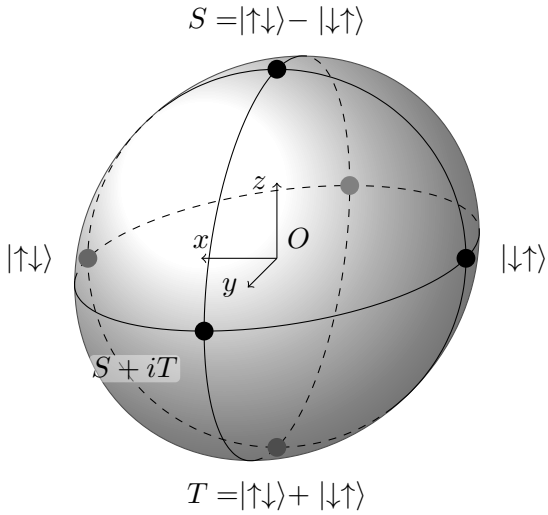

Figure 1.17: Bloch sphere for the two level system composed of the two-spins states $|\uparrow\downarrow\rangle - |\downarrow\uparrow\rangle$ and $|\uparrow\downarrow\rangle + |\downarrow\uparrow\rangle$ of two spins.

Decoherence

The aforementioned descriptions for manipulating the electron spin are supposed in an ideal world where the system couples only (or almost only) to the signals sent by the physicist. However, the electron spin does live in an environment which may affect its ability to stay in a superposed state. The principal enemy to date lies in the nuclear spins of the host wafer [29, 30, 31, 32, 33]. An electron in a GaAs-based quantum dot is typically in contact with $N \sim 10^6$ nuclei (Ga or As) of the substrate. The electron therefore experiences an effective magnetic field B_{nuc}, and we can write an effective Hamiltonian for the spin of the electron:

$$H_{\text{eff}} = \frac{1}{2} g \mu_{\text{B}} \left(\vec{B}_{\text{ext}} + \vec{B}_{\text{nuc}} \right) \cdot \vec{\sigma}, \tag{1.25}$$

where $\vec{\sigma} = \sigma_x \vec{e}_x + \sigma_y \vec{e}_y + \sigma_z \vec{e}_z$ is the Pauli vector. The total amplitude of this magnetic field, *i.e.* if all the nuclear spins are aligned, is of the order of 5 T. However, the temperature of the wafer induces random orientations of the nuclear spins. The total nuclear field is then the sum of the independent contributions of each nucleus and can be modelled by a Gaussian distribution of width $B_{\text{nuc}} \sim \frac{B_{\text{nuc,max}}}{\sqrt{N}} \sim 5\,\text{mT}$. The nuclear magnetic field experienced by the electron spin in the dot is then a random field with Gaussian probability:

$$P(\vec{B}) = \frac{1}{(2\pi B_{\text{nuc}}^2)^{\frac{3}{2}}} \exp\left(-\frac{\vec{B}^2}{2B_{\text{nuc}}^2} \right). \tag{1.26}$$

In other words, the nuclear field is constant during the characteristic time of evolution of the electron-spin state. However, when realising a manipulation

of quantum states, the experiment has to be repeated a large number of times in order to reconstruct the underlying quantum state. From one repetition to the other, the nuclear field evolves and we hence have to take into account a new random value for each repetition. In other words, the observables are averaged over all the possible nuclear field values, weighted by their probability. As a consequence, the free evolution of a single electron spin with zero applied external field reads [30]:

$$\langle \vec{S}(t) \rangle_{\text{nuc}} = \frac{\vec{S}(0)}{3} \left(1 + 2 \left[1 - \left(\frac{g\mu_{\text{B}}}{\hbar} B_{\text{nuc}} t \right)^2 \right] e^{-\left(\frac{g\mu_{\text{B}}}{\hbar} t\right)^2} \right), \tag{1.27}$$

where $\vec{S}$ is the spin of the electron. We can see that after a time $T_2^* = g\mu_{\text{B}} B_{\text{nuc}}/\hbar$ most of the information about the initial state is lost. The same phenomenon will arise for the transverse components of the spin under a magnetic field large compared with the characteristic nuclear field:

$$\langle \left| \vec{S}_\perp(t) \right| \rangle_{\text{nuc}} = \frac{\left| \vec{S}_\perp(0) \right|}{2} \left(1 + e^{-\frac{1}{2}\left(\frac{g\mu_{\text{B}}}{\hbar} t\right)^2} \right), \tag{1.28}$$

where $\vec{S}_\perp = \vec{S} - \vec{S}_z$, if the external field is along z. The decay arises with the same characteristic time T_2^*, which is on the order of 10 ns.

The value of T_2^* compared to the spin manipulation durations does not seem to qualify the spin qubit under the low decoherence criterion of DiVincenzo. However, if some manipulations can be realised faster than T_2^*, the situation can be improved. Some techniques well known from the ESR and NMR communities allow to diminish significantly the accumulated error due to the uncertainty in the magnetic field experienced by the electrons. The first and most commonly known is the spin-echo sequence. Let us consider a spin in the $|\uparrow\rangle$ state, in an external field along z and some unknown offset-field. A first $\frac{\pi}{2}$-pulse around y sends it in the vicinity of x. After half the time needed for the spin to go to the $-x$ direction—time computed from the external applied field—a π-pulse around y is sent. The result is that if the spin had time to rotate by $\frac{\pi}{2} + \epsilon$, the π-rotation will get it back at $\frac{\pi}{2} - \epsilon$. After the second half of its journey, the spin gets again the same advance ϵ and ends up at an angle π! Nicely aligned with $-x$. The same evolution without the π-pulse would have left the spin at an angle of $\pi + 2\epsilon$ instead of π. Using similar techniques, the coherence time T_2 of spin qubits has been measured to be longer than 200 µs [34].

Another important improvement that can arise comes from a phenomenon called motional narrowing. Consider an electron spin in a dot. Imagine that the nuclear field in the dot fluctuates much faster than it normally does, say much faster than the typical time needed for the nuclear field to induce a $\pi/2$ rotation. Each nuclear field configuration $B_{\text{n}}^{(i)}$ rotates the spin by an angle θ_i around a random axis $\vec{u}_i$. All the rotation angles θ_i are much

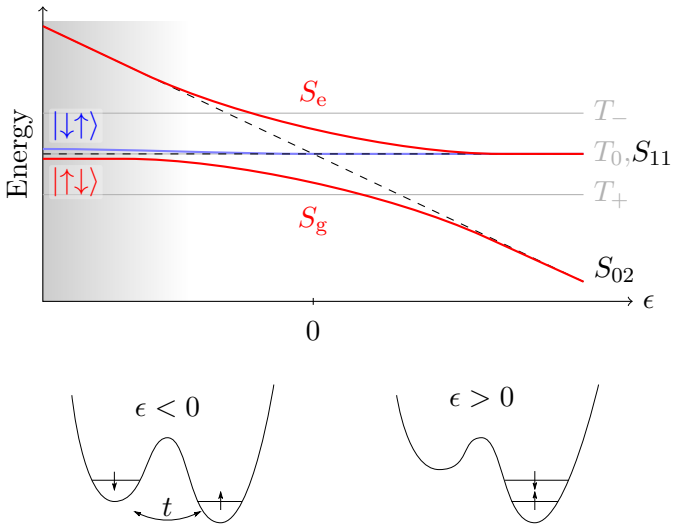

Figure 1.18: Energy diagram of two electron-spins in a double dot with tunnel coupling t, as a function of the detuning ϵ from the degeneracy between the states with one electron in each dot $(1,1)$ or two electrons in the same dot $(0,2)$. The dashed lines correspond to the singlet $(1,1)$ and $(0,2)$ states. The red lines correspond to the admixture of these two states once the tunnel coupling is made finite. The states T_+, T_-, T_0 are of the $(1,1)$ kind. The exchange interaction strength in the system is the vertical distance from S_g to T_0. It can be seen to vary as a function of ϵ. The shaded region corresponds to a Zeeman shift due to the nuclear field of the substrate larger than the exchange energy. In this region, the T_0 and S_g—which his mostly S_{11} in this region—degeneracy is hence lifted.

smaller than 2π and the total rotation will stay close to zero: the decoherence is slowed down. Another way to see this phenomenon is to consider that at each instant the nuclear field seen by the electron spin has the time to explore all its possible values, which average to a zero field. This null field does not induce decoherence [15]. We expect the rapid transport of an electron spin that we realised to exhibit this behaviour.

Spin manipulation: experiments

A short time after the spin measurement was achieved, a two-qubit gate was demonstrated by Petta and co-workers in 2005 [31]. Each qubit is borne by a single electron spin, and the two electrons are trapped in a double quantum dot. The authors used the electrically controlled asymmetry of the two dots in order to tune the exchange interaction between the two electrons (see figure 1.18). A fine control of the exchange strength through the double-dot detuning ϵ and the interaction time (down to 100 ps) allowed

them to perform coherent rotations of the two-electron spin state. Indeed, the exchange interaction lifts the degeneracy between the singlet state $S_{1,1}$ and the triplet state $T_0 = |\uparrow\downarrow\rangle + |\downarrow\uparrow\rangle$, both with one electron in each dot. The $\sqrt{\text{SWAP}}$ operation was realised as fast as 180 ps, which is much faster than the coherence time they determine: $T_2^* = 9\,\text{ns} \pm 2\,\text{ns}$. In addition, the rotation allowed the authors to apply echo sequences to the qubit. The echo sequence raised the coherence time to 2 µs, which then holds as a lower bound to T_2. For reminders, the absolute limit for a qubit is $2T_1 > T_2$. However, the coherence is usually much more sensitive to perturbations and the measured value for T_2 drops; this effective value for the coherence time is usually denoted T_2^*.

Finally, coherent single spin rotations were achieved in 2006 by Koppens *et al.*[35]. In this work, a double quantum dot is used in order to probe the spin state of an electron. This one can either go through the double dot or stay blocked in it as a function of its spin state. It was shown thanks to current measurements through the dot that applying an oscillating magnetic field on the dot allows to rotate the spin of an electron. The expected linear dependence of the resonant frequency upon the external magnetic field, characteristic of Rabi oscillations, was verified. A second experiment in which the oscillating magnetic field is not applied continuously but in bursts allowed to measure the Rabi oscillations as a function of the burst time as well as the linear dependence of the Rabi frequency upon the amplitude of the driving field.

A significant improvement to this technique was demonstrated in 2007 by Nowack and co-workers [36]: they used spin-orbit coupling inside the sample to generate the RF magnetic field. Indeed, by shaking the electron using only electric fields [8], the electron feels an effective magnetic field proportional to its momentum, due to spin-orbit coupling, since it reads [28]:

$$H_{\text{SO}} = \alpha\left(p_x\sigma_y - p_y\sigma_x\right) + \beta\left(-p_x\sigma_x + p_y\sigma_y\right), \tag{1.29}$$

where α is the Rashba spin-orbit coupling due to the asymmetry of the structure (especially the trapping potential in the z direction) and β is the Dresselhaus term due to the asymmetry of the crystalline structure, or bulk inversion asymmetry, and $\vec{p}$ is the momentum of the electron. In both cases, while the $\sqrt{\text{SWAP}}$ based on exchange is realised in the sub nanosecond time-scale, the single spin rotation typically needs around 100 ns with these schemes. It is to be noted that Rabi oscillations could be measured on times longer than T_2^* thanks to a non exponential decay. This is attributed to a non-Markovian evolution of the nuclear spin bath [37].

Another series of improvements came from the group of Pr. Tarucha: using a micro magnet fabricated on top of a double quantum dot, arbitrary

8. The use of only electric fields makes the technique more scalable and avoids extra steps of lithography to realise the antenna for the oscillating magnetic field.

rotations—electrically driven—of electron spins was demonstrated [38]. The advantage of the methods are the selectivity, scalability and the fact that it should be applicable to other materials. The design of the magnet induces a different field on each dot, hence the electrons can be addressed individually by choosing the driving frequency. The scalability and the independence of the host material come from the fact that the oscillating magnetic field (coming from a field gradient due to the micro-magnet design) is engineered instead of arising from the host material properties (spin-orbit). Hence this method should be readily transposable to other systems, like silicon-based heterostructures for example. The same system allowed the authors to sequentially select two electrons (one in each dot), apply a single-spin rotation to one of them and then entangle the two spins thanks to the exchange interaction.

Finally, despite their very long relaxation time, the usability of a single electron spin as a qubit could be questionable due to its short coherence time $T_2^* \approx 5\,\text{ns}$ to $20\,\text{ns}$ [39, 31, 40, 41, 42]. This limitation has been strongly pushed aside in a recent work from the Yacoby group [34]. A 16-π-pulses Carr-Purcell-Meiboom-Gill (CPMG) sequence was implemented that allowed to exceed $200\,\mu\text{s}$ of coherence time. This result is extremely promising for the spin qubits hosted in lateral quantum dots.

1.3.2 Other implementations

Singlet-triplet qubit

Another implementation that can be built will rely not on one, but two electrons. The information is then coded in whether the two electrons are in a singlet state or in a triplet state [9]. Usually, the $|\uparrow\uparrow\rangle$ and $|\downarrow\downarrow\rangle$ states are shifted away from the problem by applying an external magnetic field and the qubit basis is (S, T_0).

The previous discussion on exchange-controlled SWAP operation of two single spins [31] can be readily interpreted as a controlled single-qubit rotation of a (S, T_0)-qubit (see the Bloch sphere in figure 1.17). The first significant advantage of the exchange-controlled rotation is purely experimental: there is no need to send oscillating voltages at several GHz down to the sample. This fact makes the life of experimentalists much simpler, even if fast pulses will still have to be fed to the gates. The other major advantage of this implementation is the speed of the rotation: being sub-nanosecond and the coherence time of a few tens of nanoseconds, it is possible to implement echo sequences to the qubit in order to augment its

9. For reminders, a singlet state will have a form: $|\text{gg}\rangle \otimes (|\uparrow\downarrow\rangle - |\downarrow\uparrow\rangle)$ and the T_0 triplet state $(|\text{ge}\rangle - |\text{eg}\rangle) \otimes (|\uparrow\downarrow\rangle + |\downarrow\uparrow\rangle)$, where g,e are the ground and first orbital states of the trap and $|\uparrow\rangle$, $|\downarrow\rangle$ are spins respectively anti-aligned and aligned on the external magnetic field (the Landé factor g is negative).

Figure 1.19: SEM picture of the sample used to implement controlled rotation of a (S, T_0)-qubit. The two double dots couple electrostatically. Image from [43].

coherence time. However, the two-qubit gates for singlet-triplet qubits prove much more challenging than for the single-electron-spin qubit.

The first demonstration of a two-qubit gate—the C-phase gate—for (S, T_0)-qubits was realised by van Weperen and co-workers in 2011 [43]. In this experiment, two double dots are electrostatically coupled as shown in figure 1.19. The idea is that the charge configuration of the control double-dot acts as an extra-gate for the target double-dot system. In other words, having one or two electrons in the right dot of the control system will change the detuning between the two dots of the target system. This results in a modification of the energy difference between a singlet and a triplet (T_0) state. This very control knob was the one used to realise the single (S, T_0)-qubit rotations around the z axis described earlier [31], where the detuning was influenced only by "normal" top gates. The difference of induced phase for a control dot in the (0,2) or (1,1) charge configuration could reach π in 20 ns to 30 ns. However, even if being an important step, this work shows an important limit: the control bit is classical. The operation of the control system as a qubit will usually require to work at smaller detuning than used in this work, a consequence of which being that only a small fraction of charge will move from one dot to the other when changing from singlet to triplet, hence strongly reducing the controlled evolution speed—a 3 µs time for a π phase lag is foreseen—while staying under the longer coherence time achievable with echo sequences, as seen previously.

Another work, from the Yacoby group in Harvard, unpublished at the time of this writing, showed the entanglement of two singlet-triplet qubits in a similar system [44]. The two main differences are that their sample uses a linear configuration for the four dots. This achievement necessitated efficient techniques to prepare and lock the nuclear spin polarisation in the dots [45] as well as a fine control of the electrical pulses [46].

Finally, it is to be noted that the singlet-triplet qubit in double-dots

allows for an *in situ* spin-to-charge conversion: a triplet state will fall in the (1,1) charge configuration while a singlet state will go into the (0,2) charge configuration. This allows to measure the qubit without losing the charges that constitute it. Hence, this should allow more freedom in the sample design, since the tunnel coupling to the reservoirs should not be a relevant parameter any more.

1.3.3 Three electron spins

In 2000, DiVincenzo and co-authors proposed an exchange-only spin qubit. The idea behind this is to rely solely on the exchange interaction between electrons. This avoids the need for RF magnetic fields (as seen for the single-spin qubit) or for magnetic field gradients, as we have seen for a single- and two-electron spin qubit. The price to pay is an increase of complexity: the scheme proposed encodes the qubit in a three-electron spin state in a triple quantum dot. In 2010, coherent spin manipulation was demonstrated by Laird *et al.* [33]. Later on, in 2011, Gaudreau *et al.* [47] advanced a bit further and coherently manipulated spin states of the triple quantum dot that involve all three spins. The group of Marcus demonstrated as well a 132-π rotation in 20 ns in such a system [48]. Nevertheless, the lack of arbitrary waveform generators with short enough rise times added to the limited bandwidth of the RF lines nowadays prevents from achieving the corresponding π-rotation in 150 ps. In addition, none of these works could yet prove arbitrary rotations of the qubit. Moreover, the two-qubit gate still has to be investigated and should prove quite challenging, at least due to the high number of gates that will have to fit within a reduced space.

Chapter 2

Surface acoustic waves

Résumé

Les ondes acoustiques de surface (*SAWs* pour *surface acoustic waves* en anglais) ont été étudiées dans le cadre des semi-conducteurs comme un moyen de réaliser des transferts de charges rapides, synchrones et faiblement demandeurs en énergie pour des dispositifs couplés en charges ou CCDs. L'utilisation de ces ondes permet en outre de notablement diminuer le nombre de grilles fines lithographiées tout en permettant des vitesses de transport élevées, de l'ordre de $3000\,\mathrm{m\,s^{-1}}$.

Dans une première partie, les ondes de surface utilisées sont décrites, ainsi que leur mode de génération à l'aide de transducteurs inter-digités (ou IDTs). Un tel transducteur est constitué de deux peignes d'électrodes qui s'interpénètrent, comme on peut le voir figure 2.2. Une polarisation électrique de ces peignes permet de générer un champ électrique entre eux. Le substrat d'arséniure de gallium étant piézoélectrique, une déformation du matériau s'en suit. En faisant osciller la tension de polarisation dans le temps, la déformation mécanique évolue de manière oscillante : c'est la définition d'une source acoustique. Ainsi, le dispositif génère une onde acoustique dans le substrat. Le transducteur génère principalement une onde de surface (mode de Rayleigh, figure 2.1). De plus, le dessin du transducteur suppose un mode de fonctionnement résonant : la répétition périodique des sources impose de travailler à une fréquence donnée pour que les ondes générées par les différentes paires de doigts interfèrent de manière constructive (figures 2.6 et 2.7). La longueur d'onde des transducteurs utilisés est de $1\,\mu\mathrm{m}$, ce qui fixe la fréquence de résonance autour de $2.7\,\mathrm{GHz}$.

Une fois l'onde générée, elle se propage à la surface du substrat. Le raisonnement précédent peut alors s'appliquer mais dans l'autre sens : le matériau est piézoélectrique, donc la déformation due à l'onde acoustique

génère un champ électrique. C'est ce champ électrique qui est utilisé pour déplacer les charges. Nous décrivons alors dans ses grandes lignes l'évolution de la technique depuis sa prédiction par Parmenter en 1953 [49], dans lequel l'effet est prédit jusqu'aux expériences plus récentes, principalement par le groupe de Cambridge, visant à la réalisation de pompes à électrons. Ces expériences reposent sur une onde de surface qui entraîne des électrons le long d'un canal quasi uni dimensionnel. Le résultat de cette interaction est une quantification du courant entraîné par l'onde : un nombre bien défini d'électrons est *pompé* à chaque période de l'onde dans des boîtes quantiques dynamiques.

Nous discutons également la calibration de l'amplitude de l'onde générée grâce à son effet sur une boîte quantique : lorsque cette dernière est irradiée par l'onde acoustique, ses niveaux se retrouvent élargis de l'amplitude de l'onde (figure 2.9). Une spectroscopie de la boîte dans de telles conditions permet donc la calibration de l'onde (figure 2.10).

Enfin, en dernière partie de ce chapitre, nous examinons les expériences déjà existantes qui caractérisent des boîtes quantiques dynamiques (figure 2.12) ou qui étudient le spin d'ensembles d'électrons entraînés par de telles boîtes (figure 2.13). Ces expériences montrent que des ensembles de spins électroniques peuvent être déplacés de manière cohérente sur une distance de plus de 100 µm.

Sylvain Hermelin, Ph.D. Thesis

Introduction

Surface acoustic waves (SAWs) have been investigated in semiconductors to succeed top-gated structures as a mean to achieve fast synchronous charge transfer in charge coupled devices (CCDs) for example [50]. Indeed faster charge displacements, higher operating frequency, lower amount of thin lithographic lines and lower running energy cost were expected. While the first implementations needed the stacking of a piezoelectric material to generate the waves and a semiconductor to host the electrical charges [50], the principle got ported to GaAs heterostructures. There, the same material could take on both roles, since being both piezoelectric and semiconducting [12]. High speed ($\approx 2900\,\mathrm{m\,s^{-1}}$) and high frequency (370 MHz) synchronous transport has been achieved [12].

Further on, the possibility to generate quantised currents through a SAW irradiated one-dimensional channel was investigated both experimentally in the pioneering work of the Cambridge group [51, 52] and theoretically [53, 54]. The existence of quantised current plateaux at integer multiples of ef, where f is the wave frequency, reflects the existence of dynamical quantum dots in the irradiated channel. The properties of the dynamical dots could be more directly addressed in a work from Astley and co-workers [55]. In this work, the authors could probe the energy spectrum of such dynamical quantum dots and show that their properties are similar to the properties of lateral quantum dots (see 2.4.1). Lastly, coherent transport of electron spin ensembles was realised in SAW generated dynamical dots [13]. This last point will be detailed in section 2.4.2. All these preceding works paved the way to coherent transport of a single electron spin using SAWs in GaAs.

2.1 Description and generation

Acoustic waves in bulk material present three modes: two transverse modes and a longitudinal one. However, depending on the boundary conditions, other modes can arise. In particular, at the interface between a bulk material and the vacuum, a surface mode can develop. We will consider in the following the case of a semi-infinite medium, with a flat interface. The new acoustic mode that arises constitutes the Rayleigh waves [56]. The corresponding waves are commonly called SAWs for Surface Acoustic Waves. Rayleigh waves have a complex vibration pattern: the atoms of the wafer have an elliptic motion (see figure 2.1) and the amplitude of the oscillation decreases exponentially when going away from the boundary: the SAW is located within one wavelength λ from the surface of the wafer.

In order to generate the SAWs, we use interdigitated transducers (IDT). These consist of two inter-penetrating combs of electrodes as shown on figure 2.2. The application of a voltage between the two combs will generate

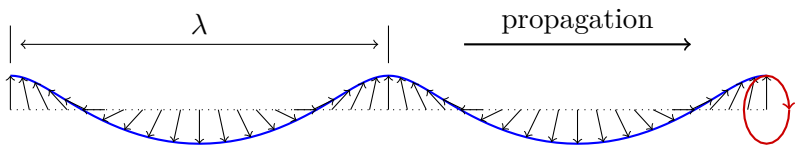

Figure 2.1: Side view of a Rayleigh wave at the surface of the propagating medium. The top part of the figure (above the blue line) is under vacuum, the bottom part corresponds to the propagating medium (here, the GaAs wafer). The wave propagates from left to right. Each arrow represents the displacement of a given atom from the substrate. The blue line is the distorted wafer surface. The red ellipse shows the movement of a given atom. The amplitude of the oscillations decreases exponentially with the distance from the surface [56].

an electric field between every pair of fingers. The penetration of the electric field in the GaAs wafer will apply a mechanical strain on the wafer due to its piezoelectric properties. A periodic change in the voltage sign will force an oscillating strain, thus generating an acoustic wave. By arranging the acoustic sources in lines much longer than the wavelength of the generated wave, one can then generate a flat beam of SAW. [1] While the acoustic wave is propagating through the sample, the induced deformation will in turn generate an electric field in the wafer. We will use the latter for our experiments.

Let us now estimate the characteristics of the generated wave. Consider an IDT with wavelength $\lambda = 1\,\mu\text{m}$ on which a resonant polarisation (*i.e.* an RF signal) of amplitude $V = 2\,\text{V}_{\text{p-p}}$ is applied, matching the applied voltages used during the experiments. The induced strain by a pair of polarised fingers will be $S = d_{14}E$, where $d_{14} = -2.69 \times 10^{-12}\ \text{m}\,\text{V}^{-1}$ is the GaAs piezoelectric constant [58] and $E \approx 1\,\text{V}/500\,\text{nm} = 2 \times 10^6\,\text{V}\,\text{m}^{-1}$ is the applied electric field. Hence, each pair of fingers will deform the material by about 3 pm. Moreover, the full piezoelectric equation for a material reads:

$$\vec{S} = \bar{s}\,\vec{T} + \bar{d}\vec{E}, \tag{2.1}$$

where $\vec{S}$ is the strain tensor [2], $\bar{s}$ is the compliance tensor of the material, $\vec{T}$ is the stress tensor, $\bar{d}$ the piezoelectric tensor and $\vec{E}$ the electric field. Therefore, the total strain in the material will be the sum of contributions coming from an incident acoustic wave and a generated strain from the piezoelectric effect. As a consequence, the strain generated by the total transducer

1. In fact the anisotropy of the wafer leads to a diverging or auto-focusing beam, depending of the IDTs' orientation with respect to the crystallographic axes of the wafer, as well as the width of the IDT [57].

2. A usual convention that we follow here is to write the 3×3 tensor $S_{\text{i,j}}$ (resp. $T_{\text{i,j}}$) as a 6-coordinate vector $\vec{S}$ (resp. $\vec{T}$) because of its symmetry. We hence have: 11 → 1; 22 → 2; 33 → 3; 23 → 4; 13 → 5 and 12 → 6.

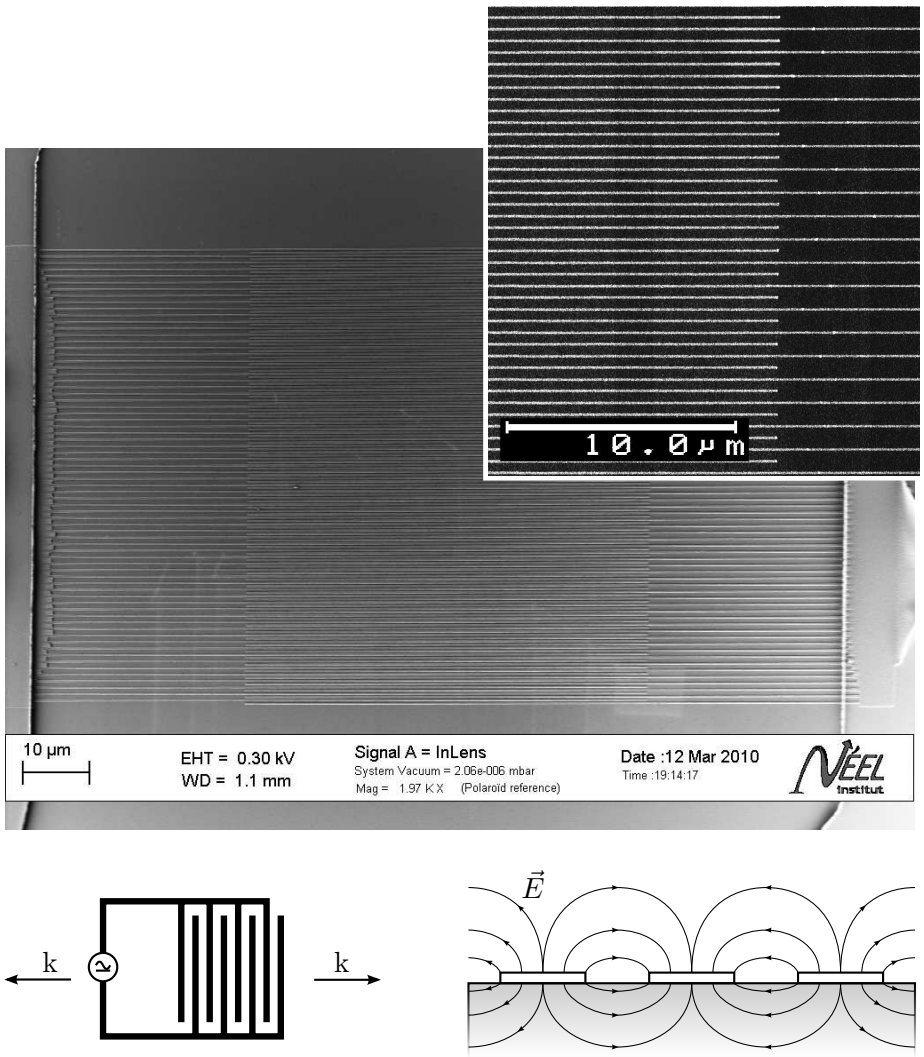

Figure 2.2: Principle of the IDT for generating the SAWs. Top: SEM image of an IDT. The RF feeds can be seen on each side. The inset is a close up on the region where the fingers from each side start to overlap. Bottom left: design principle of the IDT. Bottom right: cut view of the fingers of the IDT. Grey part is the wafer. The electric field lines imposed by the fingers are schematically depicted.

will be the aforementioned deformation due to one pair multiplied by the number of half-wavelengths of the transducer, that is a total deformation of $3 \times 2 \times 70$ pm. However, the strain field due to one pair of fingers is expected to decrease as $1/r^3$, where r is the distance from the fingers while the SAW mode is exponentially decreasing when going away from the surface. The acoustic wave generated hence cannot perfectly match the SAW mode and the generation efficiency will be reduced. We will here consider an estimate of 10 % for the matching, hence reducing the wave amplitude by an order of magnitude. In the end, the total displacement generated by our system will be on the order of 40 pm, over a half-wavelength of 500 nm. This estimation seems in reasonable agreement with vertical displacements induced by SAW measured with optical interferometry techniques [59]. In the following, we will consider that the generated wave keeps the same amplitude during its propagation. From the previously determined amplitude of deformation and the stiffness of GaAs, the stress in the material can be estimated to be on the order of 5 MPa. We can now use the second equation of piezoelectricity:

$$\vec{D} = \bar{d}\vec{T} + \bar{\epsilon}\vec{E} \tag{2.2}$$

where $\vec{D}$ is the electrical displacement vector, $\bar{d}$ the reciprocal piezoelectric tensor and $\bar{\varepsilon}$ the permittivity tensor of the material. This allows to estimate the electric field that propagates with the SAW to about 170 kV m^{-1}. Hence, assuming a sinusoidal wave, its peak-peak amplitude will be on the order of 85 mV. Taking into account the fact that the electron gas is buried 125 nm below the surface and the exponential decay of the SAW mode when going deeper in the wafer, this amplitude will be reduced by a factor of two at the level of the 2DEG. Moreover, the presence of the metallic gates will screen part of the field, further reducing the overall efficiency of the device [53]. [3] In the end, the device should allow us to produce a travelling sinusoidal electrical potential of amplitude ranging from a few millivolts to above 100 mV as seen by the electron gas when the RF power supplied to the IDT ranges from −10 dBm to 10 dBm. Since the RF lines feeding the IDTs we used have 10 dB attenuation at 1 K, the corresponding source power will range from 0 dBm to 20 dBm. Note that these powers are commonly achieved with commercial sources at 3 GHz.

The relevant parameters determining the design of the transducer are actually the amplitude of the wave, which should be high enough to prevent the electrons from tunnelling to the neighbouring dots—one dynamical dot is created every λ— and the curvature of the potential at its maxima, as shown in figure 2.3. Indeed, this parameter should be high enough for the generated dots to have a single-particle level splitting on the order of a meV.

3. A further reduction will arise from the reflections of the radio frequency signal feeding the IDT on the different connectors and the sample holder. This factor will be dependent on the frequency and is quite difficult to estimate once the cryostat is cold.

Sylvain Hermelin, Ph.D. Thesis

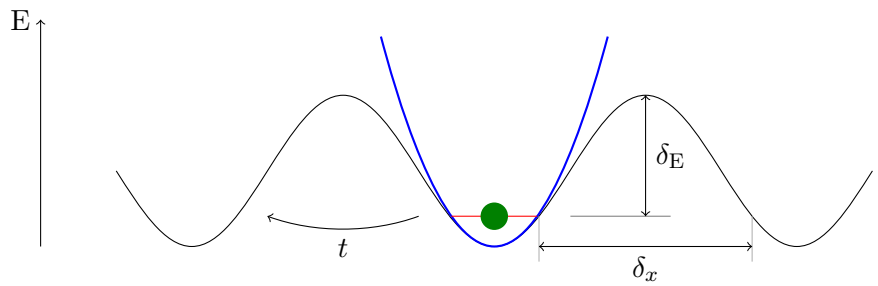

Figure 2.3: Potential wave seen by the electron. The blue curve is the parabolic approximation of the local minimum, used to estimate the single-particle level splitting of this trapping potential. δ_E and δ_x are the parameters of the tunnel barrier separating the electron from the neighbouring dot and t the corresponding tunnel coupling from one dot to the other.

Following the previous assumptions and using an amplitude of 50 meV for the potential seen by the electrons, the limited development of the electrical potential around its maximum gives:

$$V(x) = eV_{\max} \cos kx \simeq -\frac{1}{2} V_{\max} k^2 x^2 + \text{const.} \tag{2.3}$$

The potential energy of an electron in such a potential is:

$$E_{\text{elec}} = -eV(x) = eV_{\max} k^2 x^2 = \frac{1}{2} m^* \omega_0^2 x^2 \tag{2.4}$$

where $m^* = 0.067 \times m_e$ is the electron effective mass in the 2DEG, m_e the bare electron mass and ω_0 the characteristic angular frequency of the equivalent harmonic oscillator. This leads to a single-particle splitting of 1 meV, within the targeted range.

In addition, in the experiment we realised, the electrons are confined in the direction perpendicular to their motion by a one-dimensional channel (see figure 1.4 on page 31). The single-particle spacing due to the confining potential of the one-dimensional channel can be estimated following a method of Davies, Larkin and Sukhorukov [23]. The derivation assumes the surface of the wafer pinned at 0 V and neglects any screening from the 2DEG. The computation of the electrostatic potential generated in the 2DEG plane (fully depleted) by the one-dimensional channel gates shows a lateral confining potential with characteristic pulsation $\omega_y \simeq 3$ meV.

To conclude this section, the designed IDT should allow us to produce an electric potential modulation that travels at 3000 m s^{-1} and fits the requirement of mimicking the potential used to generate static quantum dots.

2.2 SAW assisted transport

The first appearance of acoustic-wave-assisted electronic transport in the literature is due to R.H. Parmenter in 1953 [49]. In this paper, Parmenter predicted that a longitudinal sound wave should generate a net electrical current in metals as well as in semiconductors [4]. His prediction relies on the fact that some of the electrons will usually have a velocity component matching the wave velocity. They will then get caught by the wave and dragged along in the sample, hence generating a current flow. [5] This discussion takes place in a regime where the fluctuations of electronic density arising from the generated field are small compared to the electronic density of majority carriers.

The first successful measurement of the acoustoelectric effect was realised in n-type germanium and was used to infer values of the inter-valley scattering time [61]. The electric field from which the electronic drag arises is the deformation potential. This potential is due to the slight band-structure modification due to the material compression or expansion coming from the acoustic wave. Later on, higher electric fields were achieved by using SAWs. The juxtaposition of a piezoelectric material and a semiconductor allowed to use the generated electric field to *synchronously* drag photo-generated electrons in depleted doped silicon [50]. The generated electrons got dragged over a distance of 3mm at a speed around 3400m/s.

In the mean time, the development of molecular-beam epitaxy growth allowed to define heterostructures of semiconductors. The resulting possibilities to engineer specific band-structures allowed to get heterostructures of GaAs that house a thin conduction channel of electrons and are a piezoelectric material at the same time. The use of such a structure allowed Hoskins, Morkoç and Hunsinger [12] to measure electrons synchronously dragged by a SAW, propagating in the heterostructure itself. The electrons were injected and collected thanks to diodes connecting the depleted channel. The electric field used during this experiment is estimated to be on the order of 77 mV with an incident microwave power on the transducer of 10 mW.

Two major extremes can be depicted out of the described works: the linear regime, where the electric field generated induces small relative changes in the carrier density, and the non-linear regime, where the electronic density is strongly perturbed by the oscillating field. The work of my Ph.D. takes place somewhere in between and investigates what happens when two reservoirs (in the linear regime) are linked by a depleted one-dimensional channel (non-linear regime) while a SAW propagates through the sample.

We now turn towards experiments in this field in which the charge in-

4. A different derivation from Gabriel Weinreich suggests that the effect should be non-negligible only for minority carriers and hence disappear for metals [60].

5. Parmenter actually uses hard boundary conditions and the electronic flow should give rise to a measurable voltage and a *classical* electronic counterflow.

jected in the SAW gets reduced. In a work of 1996, Shilton *et al.* showed that the SAW-generated acoustoelectric current gets quantised in multiple of ef when it travels through a depleted one-dimensional channel of length comparable to the SAW wavelength [51]. The device principle, presented in figure 2.4, is as follows: IDTs are placed 2 mm away from a split gate on top of a GaAs-hosted 2DEG. The wavelength of the IDTs is set to 1 µm. The gap in the split-gate is 0.7 µm wide and 0.7 µm in length. [6] The data are interpreted as the formation of moving quantum dots along the one-dimensional channel. The strong Coulomb interaction in the small areas around the moving electrostatic potential minima opens a gap in the energy spectrum of the system and these dots get loaded in a reproducible manner with n electrons, n being a positive integer. Since the current shows plateaux with respect to different parameters (split-gate voltage, source-drain bias voltage, SAW amplitude and temperatures from 300 mK up to 7 K), this work opened a new direction in the research of electron pumps for metrology standards. As a consequence the question of the quality of the quantisation and of the relevant processes that lead to it are actively discussed [53, 54] but stay unclear. In particular, the exact shape of the entrance of the channel seems to strongly influence the quantisation. The direction followed during my Ph.D. was to have a special shape for the entrance and output potentials of the channel: both were designed to form few-electron quantum dots.

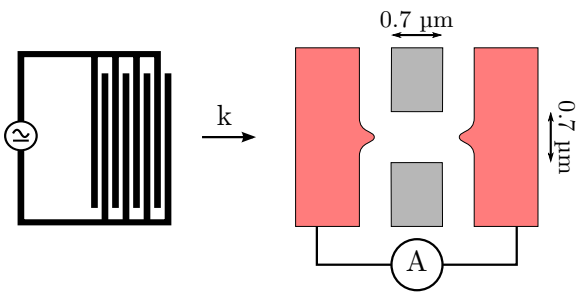

Figure 2.4: Principle of an acoustoelectric transport experiment as realised in [51]. The transducer wavelength is 1 µm, leading to a resonant frequency of 2.7 GHz.

Similar results could be reproduced in collaboration with the group of Pr. Seigo Tarucha from the university of Tokyo as shown in figure 2.5. It is to be noted that the design of the channel used for the work described in this thesis did not allow us to reproduce such results. The channel used here is indeed narrower than those usually used for quantised charge pumping and is designed to work with a quantum dot at its entrance. As a consequence, the SAW should be less efficient to pump the electrons towards the

6. The potential actually induced where the 2DEG lies will be a longer, $\gtrsim 1$ µm, and narrower channel.

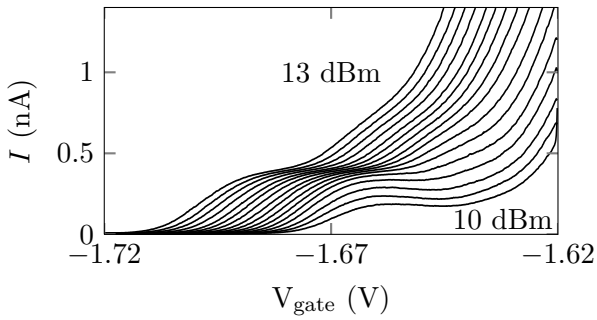

Figure 2.5: SAW-assisted transport through a quasi-one-dimensional channel. The experiment was realised with a sample close to the one in figure 2.4. Measurement taken at 4 K. The plateau appears at $ef = 411\,\mathrm{pA}$. Both the sample and the experiments were realised in collaboration with S. Takada.

one-dimensional channel and the quantised acoustoelectric current is more difficult to observe.

2.3 SAW characterisation

The characterisation of the SAW consisted in finding the resonant frequency of the transducer and a calibration of the amplitude of the generated electric field. The first measurements consisted in reflection measurements of the IDTs, by means of a vector network analyser (VNA). We expect that most of the power sent to the IDT should be reflected, except when resonant with the IDT: some of the electrical power should be translated into acoustic power, hence reducing the amount of power reflected. The figure 2.6 shows a 4K measurement of an IDT reflection. A narrow resonance can be

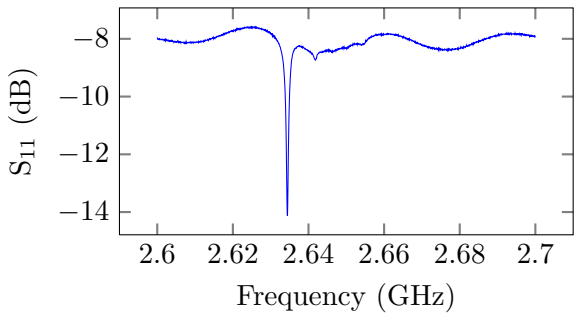

Figure 2.6: Reflection of an IDT in a $50\,\Omega$ system.

Sylvain Hermelin, Ph.D. Thesis

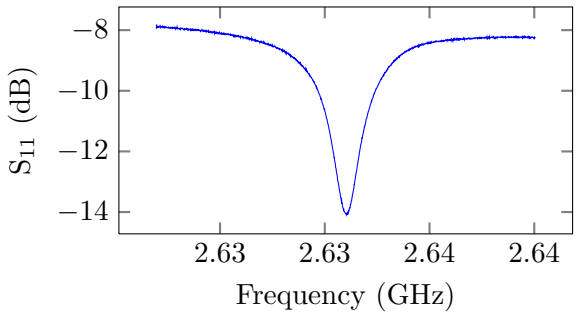

Figure 2.7: Close-up on the resonance.

seen around 2.63 GHz. A close-up on the resonance is shown in figure 2.7. Further characterisation was realised by 4 K measurements of the acoustoelectric current, similar to the one described in figure 2.4 and 2.5. The finer working point in frequency was obtained by measuring the influence of the SAW on usual transport experiments through a quantum dot at dilution fridge temperatures, following the work of the Cambridge group [62]. The conductance of the quantum dot was measured by lock-in technique while being swept across a Coulomb peak and the IDT feed frequency was stepped around the expected resonance. The measured current is shown in figure 2.8. The lock-in modulation of the bias was ±50 µV, smaller than the energy scales of the dot, as seen previously. The radio frequency sent to the IDT was stepped from 2.615 GHz to 2.655 GHz, with 9 dBm source power. This signal was modulated on the millisecond time scale with a duty cycle of 1:50 in order to limit sample heating. A clear change in the Coulomb peak amplitude can be seen around 2.633 GHz, which we associate to the presence of the SAW.

The resonance frequency of the IDT being known, the amplitude of the generated SAW has to be calibrated. This is once again realised by measuring the interaction of a SAW and a quantum dot [62]. Under a continuous-wave irradiation of SAW, we can consider the problem in an equivalent manner as a quantum dot whose plunger-gate voltage is oscillating at the SAW frequency. It follows, since the current through the dot is measured at low frequency, that the levels of the dot are effectively broadened by the amplitude of the wave, as shown in figure 2.9. It is to be noted that due to its sinusoidal shape, the SAW potential spends more time on its extrema. As a consequence, when the system is on the side of the broadened Coulomb peak (see figure 2.9, right panel), the conductance is still non-negligible. We can then extract from a 2D graph of the conductance of the dot in the plane V_{plunger}–P_{SAW} the amplitude of the SAW as a function of the source power. The amplitude, in units of plunger gate voltage, is converted to energy with the α-factor measured previously. The figure 2.10 presents such

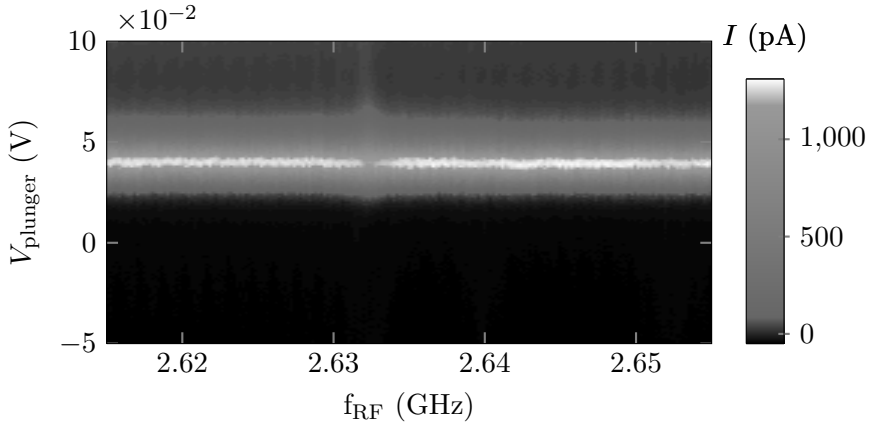

Figure 2.8: Determination of the resonance of the IDT. At $f_{\mathrm{RF}} = 2.6326$ GHz, the RF signal matches the resonance frequency of the IDT, hence generating a SAW. The latter perturbs the transport through the quantum dot

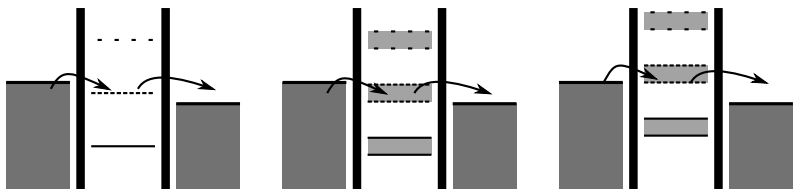

Figure 2.9: SAW broadening of the levels of the quantum dot. Left: normal Coulomb blockade, without SAW. Center: the same level is now effectively broadened due to the SAW potential. The conductance is mostly unchanged. Right: while in the normal case the dot level would be out of the bias window, the SAW potential allows it to visit the bias window. Hence, the conducting state persists longer and the peak is broadened by the amplitude of the SAW potential.

Sylvain Hermelin, Ph.D. Thesis

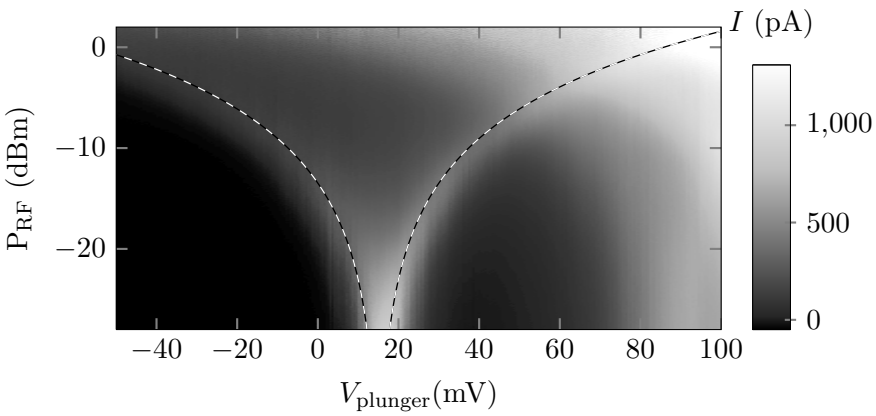

Figure 2.10: SAW amplitude calibration. The Coulomb peaks get broadened by a continuous SAW irradiation. The width of the peak allow to measure the SAW amplitude as a function of the incident power on the transducer.

a graph. The measurement was taken below 100 mK with lock-in technique under continuous-wave SAW irradiation. The bias of the quantm dot was oscillating from +50 mV to −50 mV. Since all the elements building the propagation line from the RF source to the sample should be linear,[7] the SAW electric field amplitude is related to the RF power by the relation:

$$A_{\mathrm{c-c}}[\mathrm{eV}] = \frac{2}{\alpha} \times 10^{\frac{P[\mathrm{dBm}]-P_0}{20}}, \tag{2.5}$$

where $A_{\mathrm{c-c}}$ is the peak-peak amplitude of the SAW potential, α the α-factor for the plunger gate, P the incident power on the transducer and P_0 an adjustable parameter. The latter will account for any power losses and reflections along the line: impedance mismatches along the line, attenuation of the line, mismatch between the IDT electric mode and the SAW mode, as well as the acoustic losses along the wafer and airborne RF power leaking from the sample holder. Adjusting the equation (2.5) to the data of figure 2.10, we get $P_0 = 23$ dBm. The different sources of "loss" are shown in figure 2.11.

2.4 Dynamical quantum dots

We have seen in the previous section that a SAW going through a one-dimensional channel generates moving or dynamical quantum dots. In this section, we will discuss their properties and try to bring to light that these dots should be suited for transporting a single electron spin.

7. The RF switch used to chop the signal for the previous measurement is kept in the ON state and far under the 3 dB compression point; hence it can be considered as linear.

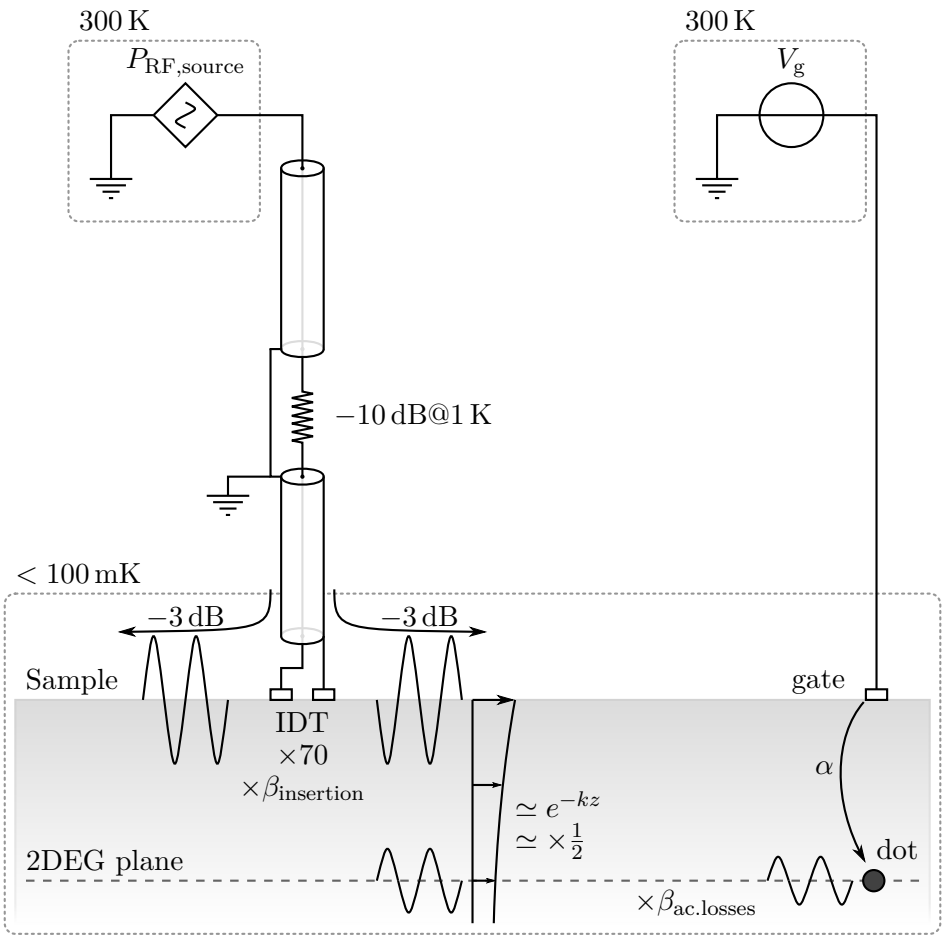

Figure 2.11: Main sources of RF signal losses along the line from the RF-source to the dot. The symmetry of the IDT implies that half the transformed power goes each direction in the wafer. Its number of pairs of finger amplifies the signal by a factor of 70. $\beta_{\mathrm{insertion}}$ represents the insertion losses, $\beta_{\mathrm{ac.losses}}$ the acoustic losses along the wafer. The localisation of the wave at the surface gives a roughly one-half factor between the surface field and the field seen by the 2DEG. α is the dot-gates lever arm defined in section 1.2.

Sylvain Hermelin, Ph.D. Thesis

2.4.1 Spectrum

Transport experiments described earlier allowed to infer the existence of a gapped spectrum due to Coulomb interaction in the dots. A work from Astley and co-workers [55], addressed the question of the energy spectrum of the dynamical dots in a more direct way. In this work, dynamical dots are created in a long one-dimensional channel (see figure 2.12). During part of their journey through the channel, the electrons present in the dot are given the possibility to tunnel out from the dot into a side reservoir. This is achieved by making one of the gates that define the one-dimensional channel much thinner in the central part (figure 2.12, inset). The large distance (around 7 µm) between the entrance of the channel and the tunnelling region allows to have an independent tuning on the tunnelling region (central part along the channel) and on the entrance of the channel, so that the number of electrons in each dynamical dot when it enters the tunnelling region can be changed independently of the barrier characteristics. In order to obtain the addition energies in the dot, the tunnelling through the side barrier is modelled and fitted to the data. This leads to $\Delta E_{1\to 2} = 2.6\,\text{meV} \pm 0.4\,\text{meV}$ and $\Delta E_{2\to 3} = 14.1\,\text{meV} \pm 1.3\,\text{meV}$. The authors question the origin for the large value of the rate between these two values. The two main explanations they offer are that the assumptions used for the tunnelling model may affect the calculation or stronger electron-electron effects since the reservoirs are further away compared to usual measurements. They note though, that the order of magnitude are comparable to that measured in static few-electron quantum dots.

This work suggests that dynamical dots can be made to have properties similar to the properties of static quantum dots, suggesting that they should be usable to transport a single electron and its spin. On the other hand, the passage from static dot to dynamical dot breaks the translational symmetry: the crystalline nature of the wafer defines a reference frame. It is therefore important to check that the properties of the electron are maintained while in the moving frame.

2.4.2 Spin of ensembles of electrons

The question of the spin of electrons in dynamical quantum dots has been partially addressed by the group of Ploog from the Paul-Drude Institute, Germany [13]. In this work, an array of dynamical dots is generated by two SAW beams propagating at 90° in a GaAs quantum-well heterostructure. The superposition of the two potentials builds up an egg-box like potential travelling at $\frac{1}{\sqrt{2}} \times c_{\text{sound}}$ (see figure 2.13). Electron-hole pairs are generated thanks to a polarised laser pulse. Electrons and holes bearing an opposite charge, they will get caught in spatially separated dynamical dots—namely electrons in the potential maxima and holes in the potential

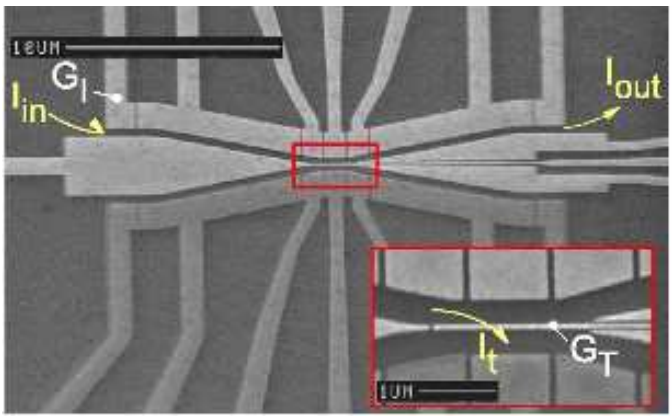

Figure 2.12: Sample used in [55] by Astley *et al.* The SAW beam arrives from the left side. The dynamical dots formed in the upper channel are brought close to a tunnel barrier in the central part (inset). There, the electrons can tunnel into the reservoir in the lower part of the sample (arrow I_t). Only the upper gates of the sample (brighter ones) were used for the described experiment. Image from [55].

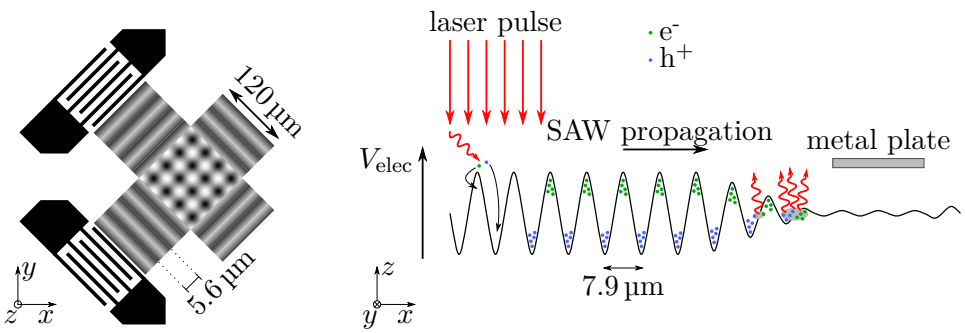

Figure 2.13: Coherent rotation of spin ensembles. Left: dynamical quantom dots are generated by two SAW beams. Right: Cut along the x-direction of left panel. Electron-hole pairs are photo-generated and separated thanks to the SAW potential. The screening due to a metal plate lifts the spatial separation and allows the e-h pairs to recombine. The emitted light is collected and its polarisation analysed.

minima. The spatial separation allows for virtually infinite lifetimes of the electron-hole pairs. Around 100 carriers' are trapped in each of the dots. Further on the carriers path, a metal plate screens the SAW potential, allowing the recombination of electrons and holes. The emitted light will carry the signature of the e-h pairs in its polarisation. The circular polarisation ratio shows oscillations as a function of both the travelled distance and the external magnetic field (aligned with the propagation direction), revealing oscillations of the projection of the spin of the ensembles of the carried electrons [8].

Assuming that all the carriers in a quantum dot have the same wave vector $\vec{k}_{\mathrm{DQD}}$, they will all see the same spin-orbit field. This one is aligned with the dots' direction of propagation (x direction on figure 2.13) for this experiment. Since the light used to generate the carriers is circularly polarised and propagates along the z-direction, the spin of the generated electrons and holes is polarised in the same z-direction. Once set into movement by the SAWs, the carriers all have the same velocity and direction of motion, $\vec{x}$, imposed by the SAW beams interference. They hence all have the same wave vector $\vec{k}_{\mathrm{DQD}}$ and experience the same spin-orbit field:

$$H_{\mathrm{SO,Dresselhaus}} = \beta\left(-p_x\sigma_x + p_y\sigma_y\right) + \alpha\left(p_x\sigma_y - p_y\sigma_x\right), \tag{2.6}$$

where β is the Dresselhaus spin-orbit coupling and α is the Rashba spin-orbit coupling. The symmetry in the z-direction of the quantum well used for this experiment brings the Rashba contribution close to zero in this sample, as was confirmed in their experiments. From equation (2.6), we can see that the spins of the electrons will precess around the direction of motion (x here). The precession rate could be readily changed by applying an external magnetic field along the same direction. The inferred values for the spin-orbit field and electron g-factor, respectively 24.7 mT and 0.493, are in reasonable agreement with theoretical predictions. The spatial period for the oscillations was 24 µm with no external field and could be changed continuously from 6 µm to 42 µm when an external magnetic field of ±20 mT was applied in the direction of the spin-orbit field.

From the previous experiments, the authors could extract a value of importance for the experiment we plan here. They showed that the spin of these ensemble of electrons evolves coherently for more than 100 µm. This rather large figure shows that carrying electrons with surface acoustic waves is expected to be applicable to the transport of electron spins in a quantum processor. The same authors discussed in a later article [14] the dependence of spin coherence length on the parameters of the heterostructure used. They show that it does not depend on the number of charges (from 15 to 140) per moving dot and confirm that the large value for the observed coherence

8. The spin decoherence of holes is supposed to be faster due to the presence of both light and heavy holes.

length comes from the confinement of the electrons. In the free case, an electron will diffuse and will be regularly scattered by the impurities of the structure. Its direction of propagation is random in between each scattering event and its spin will accumulate a rotation of a random angle around a random direction (equation (2.6) links these parameters respectively to the distance travelled between two scattering events and to the direction of propagation). This dephasing is known as the D'yakonov-Perel' mechanism [15]. In contrast, when confined, the electron motion is limited (eventually around a non-zero mean value, as in the case of dynamical quantum dots). It will hence accumulate zero random rotations in the ideal case and its spin stays coherent. In the real case, the noise coming from the environment shakes the quantum dot in a random manner. As a consequence, the spin accumulates small random rotations and its coherence time will stay finite, but much longer than in the free case. We therefore expect the spin coherence length to be on the order of 100 µm (*i.e.* 30 ns) or more when going to the single charge limit. It is this long coherence length, compared to the confinement size, that ensures the enhancement of the spin coherence time, compared to the free situation. Indeed, the confinement prevents the electron spin from accumulating significant precession angles around random directions. In addition, as discussed in chapter 1, during the transport the electron will sense a large number of different nuclear configurations. From the SAW velocity of $3000\,\mathrm{m\,s^{-1}}$ and a dot size of 30 nm we can estimate that the electron stays in contact with a given configuration for 10 ps. Since this time is 5 orders of magnitude shorter than the Larmor period associated with the nuclear field (5 mT), we expect to have motional narrowing during the transport (see section 1.3.1). For the transport from one dot to the other, we hence expect that the transfer itself will not degrade the coherence time but increase it.

Conclusion

In conclusion, SAW-generated moving quantum dots are a system that is well suited to transport a single electron. In addition, the improved spin coherence due to the confinement is a particularly promising property of such systems. The next research step is now to transport a single *chosen* electron. This will be the main part of my Ph.D. work and will be detailed in what follows. In other words, the goal was to select one electron in a quantum dot and transport this very electron towards another quantum dot, which is placed several microns away. A further step will be to measure the influence of the transport on its spin.

Chapter 3

Experimental setup

Résumé

Dans ce chapitre, nous présentons brièvement le dispositif expériemental utilisé pour la préparation de cette thèse. Cette partie représente cependant une part majeure du travail que j'ai réalisé au cours de ces trois années. En effet, lors de mon arrivée à Grenoble, en 2008, les boîtes quantiques latérales étaient inutilisées, mis à part quelques premiers développements sur des boîtes de grande taille. De plus, le réfrigérateur à dilution, nécessaire pour atteindre les températures expérimentales inférieures à 100 mK requises, avait été récemment acheté en seconde main d'un laboratoire allemand. Le trajet, effectué par camion, a ouvert un nombre de fuites conséquent qu'il a fallu réparer.

Nous présentons dans un premier temps le principe de fonctionnement du réfrigérateur à dilution (figure 3.1) : en dessous de 600 mK, la dilution d'^{3}He dans de l'^{4}He est endothermique. Le principe est alors d'assurer un flux continu d'^{3}He prérefroidi vers la boîte à mélange, où la dilution s'opère. Cette technique permet de descendre à des températures de l'ordre de quelques mK. Les puissances frigorifiques, à 100 mK vont typiquement de 50 µW à 1 mW.

Dans une deuxième partie, nous présentons brièvement les sources de tensions continues, basées sur des convertisseurs numérique-analogiques commerciaux (Linear Technology LTC2604), intégrés sur des cartes développées en interne par Christophe Guttin. Chaque carte intègre huit sources de tension ± 5 V, qui peuvent être adressée au MHz. La tension en sortie a cependant un taux de variation limité à 300 mV µs^{-1}. Ces sources sont commandées par un FPGA (intégré sur une carte National Instruments Single Board RIO 9612). L'état actuel du programme permet de changer une source parmis les 64 possibles chaque 16 µs. Nous présentons ensuite les sources

radio-fréquences utilisées : un générateur arbitraire (Tektronix 5014B), qui permet de générer une tension arbitraire toutes les 830 ps (1.2 GHz), avec un temps de montée 10 %–90 % de 950 ps. Cette source est utilisée directement pour induir des changements de polarisation rapides sur des grilles de l'échantillon, mais également pour hâcher les signaux monochromatiques (2.6 GHz) générés par une source continue (Agilent E8257D). Le schéma de hâchage est présenté figure 3.3 et les signaux qui en résultent figures 3.4 et 3.5. Les mesures sont effectuées par une conversion courant-tension (convertisseurs réalisés en interne par Daniel Lepoittevin, basés sur un amplificateur opérationnel OPA141 de Texas Intruments, gain 10^6 à $10^9\,\mathrm{V\,A^{-1}}$). Les tensions sont ensuite numérisées soit par un voltmètre Keithley K2000 soit par un oscilloscope LeCroy WaveRunner 6050A (dans ce cas, le convertisseur courant tension est suivi d'un amplificateur de tension de gain 100 basé sur un amplificateur opérationnel AD620 d'Analog Devices).

En dernière partie de ce chapitre, le programme de gestion de l'expérience est très brièvement ébauché. Celui-ci se décompose en deux parties : une embarquée dans le FPGA, l'autre sur l'ordinateur hôte. La structure du programme FPGA est décrite par la figure 3.6. Il se charge de la gestion des sources de tension (vitesse de variation des rampes lentes, séquences d'expérimentation rapides, génération de signaux oscillants) et de l'envoi de pulses de synchronisation aux différents instruments. Le programme hébergé par l'ordinateur hôte se charge de configurer les instruments (FPGA compris), de récupérer les données et de les stocker.

Sylvain Hermelin, Ph.D. Thesis

Introduction

In this chapter, we will describe the experimental setup used during my Ph.D. It represents an important part of the work realised over the past three years. Indeed, when I arrived in Grenoble in 2008, the activity on lateral quantum dots in GaAs was just at the beginning. Moreover, on the cryogenics side, a very large dilution refrigerator (Oxford 1000) was acquired from the University of Bayreuth, Germany, and a major overhaul was necessary. This included the replacement of several parts of the dilution unit (continuous heat exchanger, numerous indium seals) as well as the entire wiring of the cryostat (thermometry lines, DC lines, RF lines). The other major part was to develop a software suite to run the experiment. In this chapter, we will first examine the hardware part, glancing at the cryogenics and detailing the electronics. Second, we will describe the software developed in order to run the experimental sequences described in this manuscript.

3.1 Cryogenics

As mentioned earlier, working with lateral quantum dots requires temperatures on the order of 100 mK. This temperature range is commonly achieved using dilution refrigerators. We will now quickly present their principle and the inherent limitations relevant for this project.

Below 0.87 K, the dilution of ^{3}He in ^{4}He is an endothermic process, the cooling power of which scales with T^2. The idea behind the refrigerator is then to impose a flow of pre-cooled ^{3}He that will dilute in ^{4}He. In practice, the dilution unit is organised around different stages that are presented in figure 3.1. We will quickly describe them starting from the higher temperature. The dilution unit is surrounded by 4 K liquid helium. This bath allows to pre-cool the unit and the inlet of ^{3}He. Since the dilution should go below 4 K, it is isolated from the helium bath by vacuum. The ^{3}He flow is further cooled to 1.5 K by the 1 K-pot. This stage is a pumped reservoir of ^{4}He which is continuously refilled from the helium bath. The two following stages allow to transfer heat from the ^{3}He inlet to the cold ^{3}He outlet. First the continuous heat exchanger allows to go below 100 mK and then the step heat exchangers allow to go down to 2 to 5 mK [63, 64]. The fridge used for my Ph.D. had a base temperature around 20 mK.

The available cooling power is of the order of 1 mW at 100 mK and gets approximately an order of magnitude larger for each stage presented in figure 3.1 (cold plate, still and 1 K pot). This means that the cables going down the dilution unit have to bring as little heat as possible. This is achieved by carefully choosing the materials and thorough thermal anchoring to every stage of the fridge, as presented in figure 3.2. The thermal anchoring is crucial for the electronic temperature of the sample and of the thermometers:

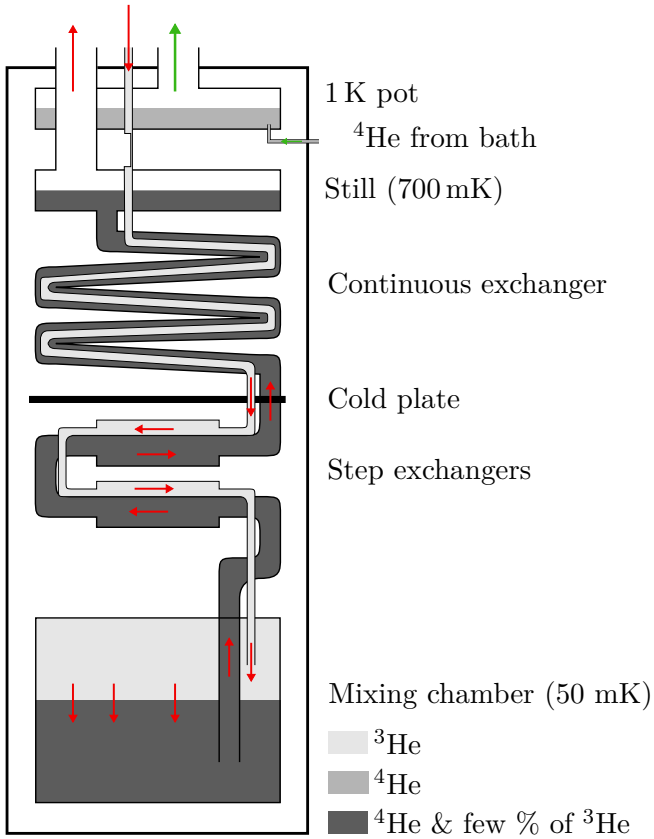

Figure 3.1: The ^{3}He flow is first cooled to 4 K by the He bath. The 1 K-pot cools it further to 1.5 K. This one pumps liquid ^{4}He from the 4 K He bath around. Further cooling is assured by the counter-flowing ^{3}He. The dilution (cooling process) happens in the mixing chamber. The outermost limit designs the inner vacuum chamber (IVC), which thermally isolates the dilution from the liquid ^{4}He, 4 K bath around.

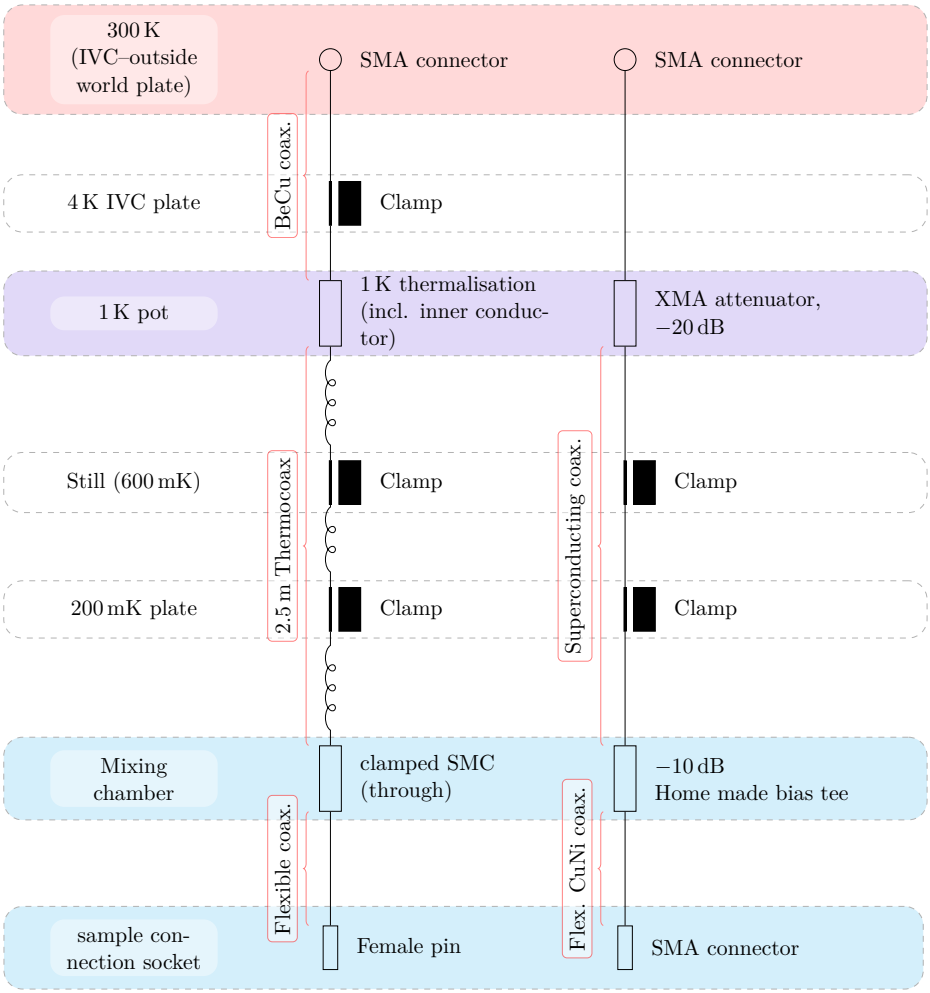

Figure 3.2: Thermal clamping of the electrical lines. The coloured parts correspond to the main thermalisation stages. The line depicted on the left part corresponds to a DC line, the one on the right to an RF line. The lines are in vacuum all the way from 300 K.

it should absorb the electromagnetic excitations transported by the lines. That is why long Thermocoax™ coaxial cables are used: the dielectric (MgO or Al_2O_3) is quite dissipative for electromagnetic signals above the GHz range. Hence, the high frequency modes that enter the line—fed at least by the black body radiation at high temperature—are efficiently converted to heat along the cable. The heat load is then absorbed by the fridge at its different stages, thanks to the thermal anchoring of both the inner- and outer-conductor of the coaxial lines. In the case where these modes do not get dissipated, they will be directly coupled to the sample and the electron temperature will rise.

The high frequency lines pose a problem: their role is to "guide" the excitations in the GHz range down to the sample. In order to keep the electron temperature low, one has to attenuate the signal along the line. Attenuators, from XMA Corp., are placed at 1 K (-20 dB) and at the mixing chamber (-10 dB) for the gate lines, which we would like to be able to move on the ns timescale. This attenuation ensures that high frequency modes and especially the noise coming from the signal generator will not perturb significantly the sample. However, since the amplitude of arbitrary waveform generators tends to be more and more limited when going higher in frequency, the pulse amplitude will be limited. For the generator we used during my Ph.D.—Tektronix 5014B—the amplitude was 4.5 V peak-peak. With a 30 dB attenuation, the pulse amplitude reachable at the sample will be around 140 mV. The IDT feed lines represent a special case: they couple less directly to the sample electrons and need a high signal amplitude. We thus chose to apply only 10 dB of attenuation at 1 K. Since the bandwidth of the IDT is only around 3 MHz and the signal does not couple directly to the electrons, but (twice) *via* the piezoelectric effect, the noise amplitude actually reaching the electrons is limited. A Fermi-distribution adjustment on the time-averaged population of the dot as a function of its energy allowed us to estimate the electronic temperature to be below $\simeq$150 mK [65], as will be discussed in chapter 4.

3.2 Electronics

The electronic setup is very important in such an experiment. Namely, the first requirement will be to get low-noise electronics, otherwise the whole point of filtering developed in the previous section gets useless. The two major sides will be "control" and "measure". The "control" is related to the voltages applied to the gates and the voltage bias applied to the reservoirs *via* the ohmic contacts. The "measure" corresponds to the amplification and digitisation of the low-level signals generated in the sample.

3.2.1 Voltage sources

The nano-structure defined for the transport experiment we describe in this thesis is defined by 12 electrostatic gates. We hence need a large number of voltage sources. In addition, this rather large number of gates implies a parameter space for the experiment that is *very* large. It is then preferable to have the possibility to move the voltages fast enough—this point tends to be contradictory to the low-noise characteristic—in order to explore the parameter space in a reasonable time. In addition, as we will see in the next chapter, having fast voltage sources will allow us to access useful metastable states in the system.

The main voltage sources used in our experiment are based on a commercial digital-to-analog converter (DAC) chip: Linear Technology LTC2604. The major interests of this chip for this experiment are its 16 bits, the 2.5 V to 5.5 V operating range, its low output noise and its "high" speed, as discussed further. This chip is then embedded on a home-made PCB board including low-voltage power-line filtering, a low-noise amplification stage of the output and the communication optical isolation and logic. Each PCB board hosts 8 sources. The outputs are coaxial, which allows to get fully shielded lines from the DAC to their entrance into the fridge, and even down to a few millimetres from the sample. The complete board then allows to have 8 parallel ±5 V sources with $25\,\mathrm{nV\,Hz^{-1/2}}$ noise, with the possibility to change one of the voltages every 16 µs. The rise time for the voltage is slew rate limited to $300\,\mathrm{mV\,\mu s^{-1}}$. A first optimisation (already in place on a similar setup) now allows to change one of the sources every microsecond. Finally, a minor rework of both the hardware and the software will allow a simultaneous change of all the voltage values every microsecond.

The DACs are controlled by a National Instruments Single Board RIO 9612. This board hosts a Xilinx FPGA [1], one hundred 44 MHz digital input/outputs, grouped in ports of 10 I/Os. In addition, an embedded microcomputer takes care of the communication between the board and a computer. Each of the first ports is used to drive a board of 8 DACs. A block diagram of the FPGA program will be presented further on.

3.2.2 High frequency generators

The high-frequency pulses used for fast gate-voltage changes are generated with a Tektronix 5014B arbitrary waveform generator. It allows to generate arbitrary 14-bit signals, with a peak–peak amplitude up to 4.5 V. The sampling rate goes up to 1.2 GHz, but its rise time—10 % to 90 %—is limited to 950 ps. This generator also gates the continuous-wave generator—

1. Field Programmable Gate Array. FPGAs are chips hosting logic gates that can be rewired during a programming stage. In other words, they allow to have fast wired logic that can be changed on demand. They are an ideal tool for digital electronics prototyping.

Agilent E8257D—used to excite the SAWs. The gating scheme is shown in figure 3.3 thanks to a mixer, Marki M8-0420LS, and an RF switch, Skyworks AS186-302LF (doubled), and the output of the SAW signal generation line

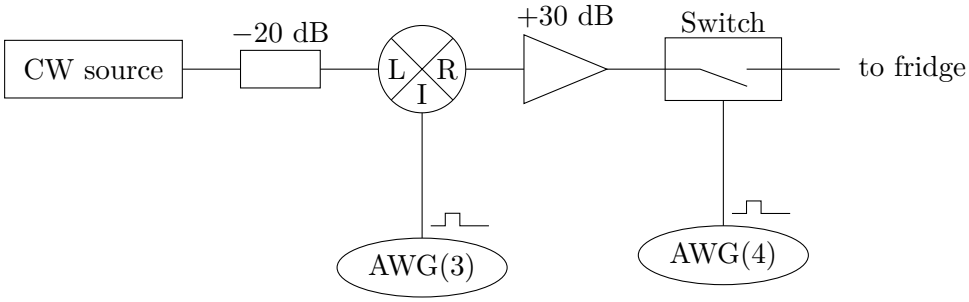

Figure 3.3: SAW excitation gating scheme. In order to get a fast gating of the SAW excitation, the output of the continuous wave generator is sent through a mixer, Marki M8-0420LS, and two cascaded RF transistors, Skyworks AS186-302LF. The signal is amplified between the two stages, since the mixer can only work at a power below 20 dBm. The switch, slower (rated 30 ns), allow more power (around 30 dBm). The command signal is generated by a Tektronix 5014B (AWG).

is presented in figure 3.4. We can see that the rise time of the gating and amplification signal is around 20 ns followed by a smaller and slower rise of the amplitude. This slow rise comes from the RF switch. This one is however needed in the amplification line for its on/off ratio of 70 dB and its high power (30 dBm). A close-up on the rising side of the burst is shown in figure 3.5a. The fall of the signal, shown in close-up in figure 3.5b, is much faster. It must be kept in mind that this signal then goes through the IDT, which means that the time signal of the actual sound wave should be the signal shown figures 3.4 and 3.5 convolved by a 27 ns gate function, due to the 70 pairs of fingers of the IDT.

3.2.3 Measure

On the measure side, currents are pre-amplified thanks to home made current-to-voltage converters, based on a Texas Instruments TLC2201 operational amplifier. The band pass of this I/V converter, including DC, varies from 0.8 kHz to 1.4 kHz, while going from $1 \times 10^6\,\mathrm{V\,A^{-1}}$ to $1 \times 10^9\,\mathrm{V\,A^{-1}}$ gain. The output voltage is then directly measured by two Keithley K2000, with an averaging time per sample down to 2 ms, for a sampling rate up to 3 ms per sample (that is the K2000 has a down time of 1 ms). For faster measurements, the I/V is set on $1 \times 10^7\,\mathrm{V\,A^{-1}}$ and an amplification stage of gain 100 is added. This amplification stage relies on an Analog Devices

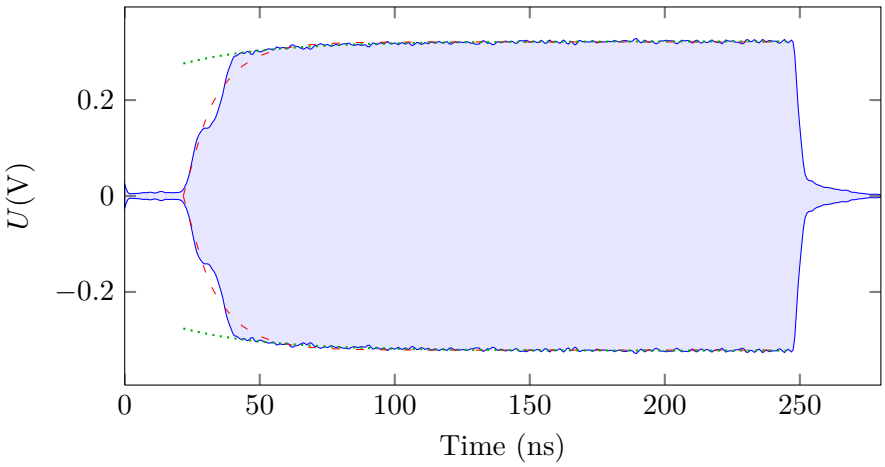

Figure 3.4: SAW signal envelope. The RF switch is turned on from 0 ns to 280 ns and the mixer is gated from 30 ns to 250 ns. The dashed red line is an exponential approximation of the overall shape with 12 ns characteristic time. The green dotted lines are an exponential fit on the smaller variation after $t = 45$ ns, with characteristic time 32 ns and represent 7 % of variation.

AD620 operational amplifier. The strong common-mode rejection ratio of this chip allows to partially decouple the grounds of the experiment and measuring oscilloscope. The signal is then RC filtered ($R = 517\,\Omega$ and $C = 100$ nF for a characteristic time $\tau \simeq 50$ µs) before being sampled by a LeCroy WaveRunner 6050A. Further software filtering (moving average) is applied on the signal. The rise time of the amplification chain is around 150 µs.

3.3 Software

A non-negligible part of the setup consists in the software I developed during my Ph.D. This software is built in two major parts: one is embedded in the FPGA chip in order to realise the microsecond control of the electronics, to take care of microsecond gate-movements and to trigger the external apparatuses—the arbitrary waveform generator and the voltmeters. The other layer of software resides in a computer, designated as the host computer in the following. This computer is linked to the FPGA *via* an ethernet network.

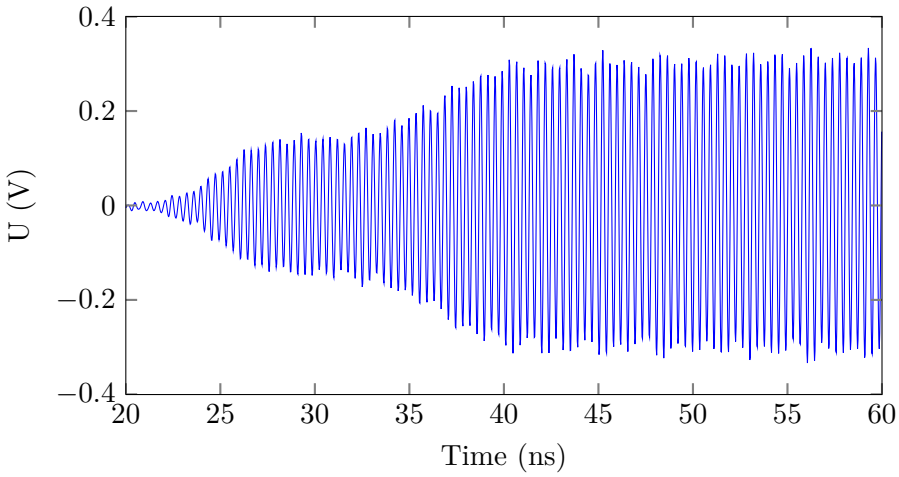

(a) Rising of the signal (close-up). The long rise-time of the signal, due to the RF switch, is a problem that should be addressed in the future in order to get shorter bursts and hence limit the increase of the electronic temperature due to the SAW irradiation.

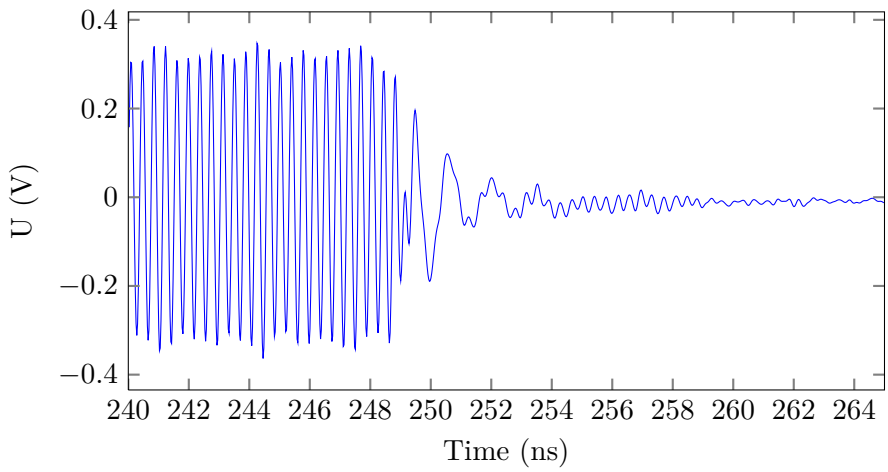

(b) Falling of the signal. Note that the signal should get off-resonance with respect to the IDT within a few nanoseconds.

Figure 3.5: Details of the rising and falling "edges" of the SAW burst presented in figure 3.4.

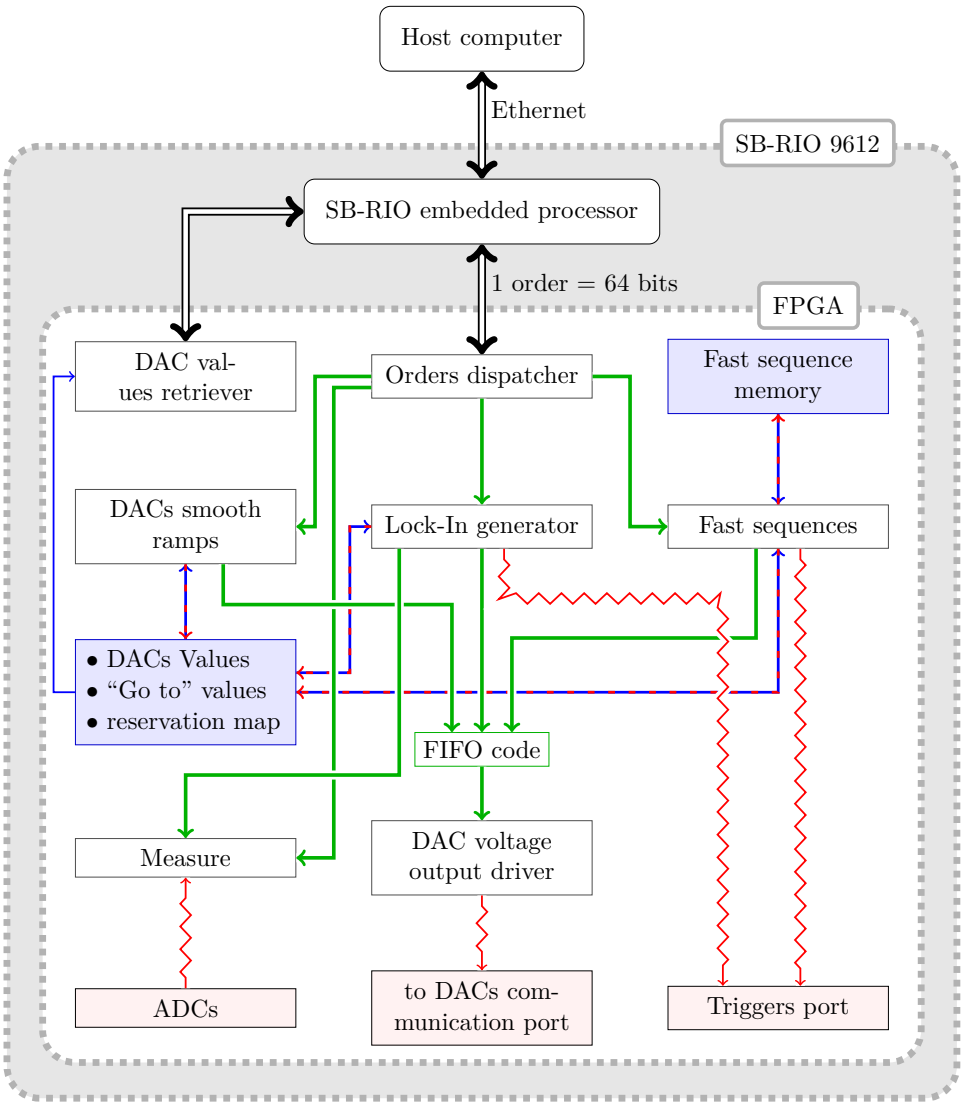

Figure 3.6: FPGA block diagram. ⟶ represents a FIFO communication line, ⟵ a memory read access (the arrows always show the data flow), ⟷ a memory read and write access, and ⇝ represents a direct access to the physical lines. ⇔ represents an acknowledged communication between two different hardwares. The red and blue boxes respectively represent physical lines and embedded memories. The "FIFO code" block corresponds to synchronisation code taken care of by LabView.

3.3.1 FPGA code organisation

The figure 3.6 presents a block diagram of the different subsystems coded in the FPGA. The most important parts are: "DACs smooth ramps" which takes cares of moving smoothly the DAC voltages: the ramps are constituted of steps of 150 µV every n ms, where n is user set, usually at 2. In practice, the user gives "goto values" for each DAC and the FPGA starts all ramps in parallel once a "go" signal is given by the user. The orders from this subsystem are then fed to the output driver through a FIFO channel[2]. The "goto values" and current values of the DACs are saved in embedded memories linked to the FPGA. Two other major subsystems are able to change the DAC values: a lock-in signal generator and the fast sequence system. The latter allows for arbitrary waveform generation. The lock-in generation will simply add a square oscillation of user set frequency, up to a few kHz, and amplitude, up to ±2.5 V, on top of the DC value of a DAC. This signal applies to only one DAC at a time, selected by the user at any time. Note, it allows to switch the lock-in excitation from a bias to gate without disconnecting anything from the sample. This point is important since for such a configuration change, the gate does not have to be depolarised, which could induce switches in the sample. It also outputs a physical synchronous trigger and a software trigger for the measuring system. The fast-sequence system is a major realisation of this setup. It allows to add arbitrary signals on top of the DC value of 16 arbitrarily chosen DACs (the list of which can be changed at any time as well). The waveforms are built as a sequence of orders, each being one of:

- a new DAC offset value for *one* of the 16 DACs (takes 16 µs per order),
- a delay, from 1 µs to 2 ms, with a 1 µs resolution, or up to 35 hours with a resolution regularly decreasing down to 35 minutes,
- a new state for the physical triggers and/or an order to stop the sequence,
- a jump to another slot of the sequence (no conditional jumps yet, but they could be straightforwardly implementable).

In addition, it offers the possibility to output a periodic trigger—at a user set frequency, gated by some sequence orders—in order to trigger the voltmeters. This piece of software actually allowed to realise complex trajectories along the stability diagrams of the dot and hence allowed to reach many more high energy metastable configurations for the dots before they lose their electron(s) (as will be discussed in the next chapter). The inner details of the blocks presented in figure 3.6 will not be presented here for simplicity.

2. First-In, First-Out: the first enqueued element will be the first dequeued on the reception side. Note that the FIFO communication is almost mandatory in order to allow the different base loop timings for the different subsystems.

3.3.2 Host-computer software

In order to be useful for the experiments, a few more layers of code are needed in the host computer. The main goal here is to be able to sweep any parameter of the experiment while stepping any other in order to build 2D colour-maps of the sample characteristics as a function of two parameters. In addition, one usually wants to be able to step an extra parameter to see how these colour-maps evolve as a function of a third parameter. We will respectively call these dimensions d_1, d_2 and d_3, or sweep, step and step2; n_j will represent the number of steps—*i.e.* $n_j + 1$ points—the user asks for dimension d_j. An extra requirement will usually be that an extra apparatus should be easily added to the setup.

This functioning is achieved by two major means: the next point in the parameter space is recursively [3] computed and sent to instrument drivers that will take care of sending the new point to the relevant apparatus if needed. In other words, each parameter of the experiment has a place on the GUI [4] on which the user will define the parameter as being static during the experiment, swept, stepped ... Only the DACs are a special case: the user has to enter which DACs are swept, stepped, *etc.*. Up to 4 DACs can be specified for each dimension [5], which comes in handy when tuning two distant dots. Any number of instruments parameters can be moved on the same time.

At the expense of losing some of the generality described above, the software and physical architecture allowed to develop a fast-measure mode. In this mode, the sweep is not controlled by the host computer but rather by the FPGA: the host computer sets the voltmeters or oscilloscope in the right triggering mode and then tells the FPGA to start the fast sequence loaded in its memory beforehand. The FPGA will then take care of moving the DACs and sending the triggers to the instruments. Once the instruments are done taking the measurements—after a given number of points [6] for the voltmeters or after a given time for the oscilloscope—the points are sent back to the computer and the data saved to a file. The program then computes the new points and starts again. This architecture allows to take a stability diagram of 300×400 points with an averaging time per point of 2 ms in about 15 minutes, and to get the 10,000 repetitions of table 4.1 within one

3. The recursive approach allows for a more readable code and ease of extent to more dimensions. However, the resulting volume of data and the ability of the human being running the experiment to cope with more than 3 dimensions usually prevents from doing so.

4. Graphical User Interface

5. Note that the code structure allows to increase this figure in a straightforward manner: the number of DAC lines in the GUI simply has to be increased.

6. The voltmeter is triggered by the FPGA for each point. This allows a better reproducibility in the duration between two points and to take measurements that are not contiguous in time.

hour. In addition, by setting the fast sequence to a ramp for one or more DACs, it is possible take stability diagrams like those presented in figure 4.6 rather fast: 3 ms per point, the whole scan in about 10 to 15 minutes.

Chapter 4

On demand single-electron transport

Résumé

Dans ce chapitre, nous discutons le principal résultat de cette thèse, c'est à dire le transport, sur demande, d'un électron unique. Plus exactement, nous montrons comment un électron unique peut être transporté d'une boîte quantique à une autre, distante de quelques microns. Le transport se fait à l'échelle de la nanoseconde et l'électron reste confiné dans une boîte quantique en mouvement durant tout le trajet. Ce dernier devrait permettre de maintenir la cohérence d'un bit quantique codé par le spin de l'électron.

Dans un premier temps, l'échantillon utilisé est décrit : deux boîtes quantiques, chacune équipée d'un point quantique (QPC) pour permettre la détection de la charge présente dans les boîtes et un canal unidimensionnel qui relie les deux boîtes (figure 4.1). À 2 mm de part et d'autre de ce dispositif sont placés des IDTS. Cependant, un seul des deux IDTs fonctionne, la lithographie du second ayant été défaillante.

Une spectroscopie en transport du canal unidimensionnel est présentée sur les figures 4.3 and 4.4 ; ces données permettent de définir le domaine de polarisation souhaité pour que le canal soit exempt d'électrons. Les diagrammes de stabilité des deux boîtes sont ensuite étudiés dans le régime où le canal est totalement dépeuplé (figure 4.6). L'étude de ces diagrammes permet de mettre en évidence la possibilité de placer les boîtes dans des états méta stables : le potentiel chimique de la boîte peut être amené significativement au dessus du niveau de Fermi pendant des temps pouvant dépasser la seconde (figures 4.8a à 4.10). Après une caractérisation de ces états (figure 4.11), nous mettons en évidence la possibilité d'en forcer la

sortie d'un électron en envoyant un train d'onde acoustique (figures 4.12 et 4.14). Enfin, les électrons ainsi éjectés sont attrapés dans la boîte de l'autre côté du canal (figures 4.15 et 4.16). Les corrélations entre les évènements d'injection et de réception sont étudiés sous différentes conditions expérimentales, ce qui permet de conclure que l'électron reçu est bien l'électron que nous avons envoyé (table 4.1). Il est à noter que le taux de réussite pour le transfert avoisine les 90 % — 96 % pour l'envoi et 92 % pour la réception. Il est ensuite démontré que le début du transfert peut être déclenché avec une précision de la nanoseconde (figure 4.20). Le temps de transfert — 1 ns — et la précision à l'envoi place ce mode de transfert en dessous des temps de cohérence généralement observés pour les bits quantiques codés par des spins électroniques, *i.e.* de 10 ns à plus de 200 µs avec de multiples séquences d'écho de spin [34]. Les taux de réussite du transfer (principalement de l'envoi) sont ensuite étudiés en fonction de différents paramètres du système : polarisation du dot (figure 4.22), temps de SAW (figure 4.25), amplitude de l'onde (figure 4.24).

Introduction

In this chapter, we will discuss a first milestone towards the single-electron-spin transport between distant quantum dots. In particular, we will show how a single electron, selected and isolated in a quantum dot, can be sent on demand towards a distant quantum dot. The scheme used relies on both the ability to prepare metastable charge states in quantum dots and the possibility to use SAWs to drag electrons in dynamical quantum dots.

After a description of the sample used, we will show that the quantum dots used can be tuned in the single-electron regime. Important properties of the system like long tunnelling times and metastability of the dot will be explored. Then the ability to extract the electron from one dot thanks to a SAW burst will be detailed. Next, we will show the complete sequence that allows to send the single electron from one dot to the other, which will consist in an initialisation stage (loading the injection dot, emptying the reception dot), a movement stage to bring the injection dot in a metastable state closer to the one-dimensional channel (both geometrically and energetically) and prepare the reception dot, followed by the transfer itself: a burst of SAW. Finally, the efficiency of the transfer as a function of different parameters will be analysed.

4.1 Sample

The sample used for the results presented in this manuscript (shown in figure 4.1) is constituted of two quantum dots placed 3 µm apart from each other. These quantum dots will have for role to isolate a single electron out of the Fermi sea. In order to infer the charge state of the dots, quantum point contacts (QPCs) have been added close by each dot. Since the ultimate goal of the sample is to transport an electron spin between these two dots, we need to be careful not to lose this information during the journey of the electron. This obviously implies that we should not lose the electron itself. In addition, the information can be lost if other electrons are in the way: if the electron we transport mixes with other electrons, then the information coded on its spin will be diluted among all the electrons at play. As a consequence, we should keep the electron isolated from the other electrons. That is why we add two long gates which will allow to define a quasi one-dimensional channel linking the two dots together. These gates do not only guide the electron: they have the crucial role of fully depleting the one-dimensional channel, thus preventing, in principle, the transported electron from mixing with other electrons and losing the information coded on its spin. To transfer the electron, we will use a SAW, which can drag electrons along a one-dimensional channel as discussed in chapter 2. The IDT that will generate the SAW is placed at a distance of 2 mm to the

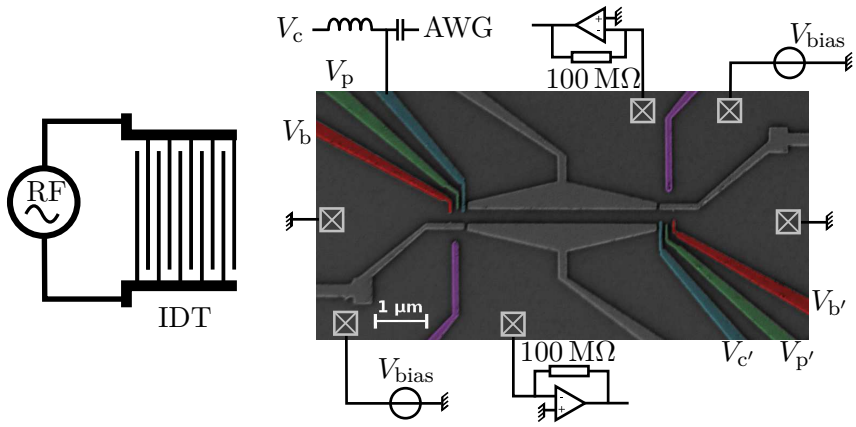

Figure 4.1: SEM image of the sample. We can see the two quantum dots on each side, their QPCs and the 1D-channel link between them. The IDT is placed 2 mm on the side. All the gates are connected to low-noise voltage sources. The ohmic contacts (crossed squares) are biased with the same voltage sources (divided by 1000 at room temperature). The currents are measured thanks to current-to-voltage converters, schematically depicted.

left side of the sample. This large distance is expected to reduce the direct electrical influence of the RF excitation on the 2DEG. A detailed view of an IDT can be viewed in figure 4.2. While this sample has been realised by our collaborators at the University of Tokyo, the technology has been transferred to Grenoble during my Ph.D.

4.2 Few electron regime and tunnelling times

In order to attain the goal cited above, the one-dimensional channel of the dot has to be fully depleted in order to prevent the mixing of the transported electron with other electrons. The first task is then to characterise the one-dimensional channel. This is done by measuring its conductance as a function of the gate voltages. The point where the conductance drops to zero is called the pinch-off. We present the pinch-off curve for the one-dimensional channel in figure 4.3. The 1D channel will be depleted when no quantum channel is fully open any more. This corresponds to a resistance $\frac{h}{2e^2}$ (the factor of 2 relates to the spin degeneracy). From these data, we can then see that the channel will be below a single open quantum channel for gate voltages below -0.36 V. However, the channel keeps a finite conductance down to gate voltages around -0.45 V. The lower panel of figure 4.3 shows the Coulomb blockade features that arise in the conductance of the 1D channel when its resistance reaches the MΩ regime. The presence

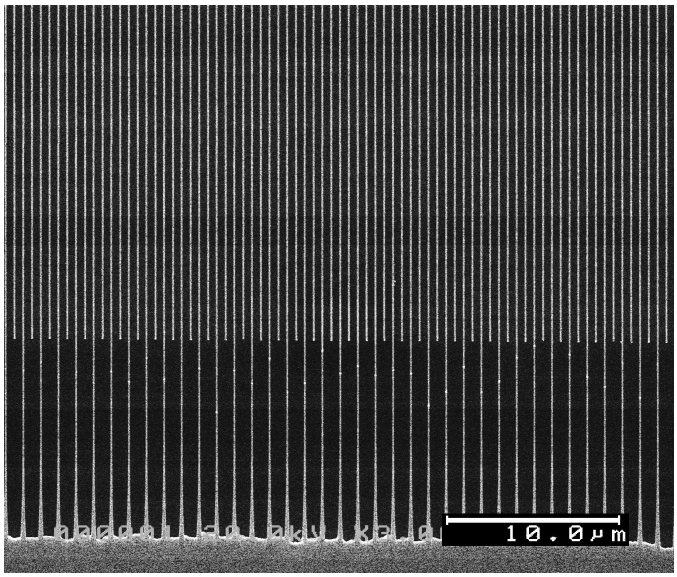

Figure 4.2: Detail of an IDT. The wavelength is 1 µm. The area of overlapping fingers is 60 µm × 70 pairs of fingers. The width of each lines is around 250 nm.

of Coulomb peaks suggests that some puddles of electrons remain in the 1D channel. When the level in one of these gets within the bias window electrons can flow through the channel, stopping off in the puddles. Moreover, a study at larger bias of these structures reveals the corresponding Coulomb diamonds, shown in figure 4.4. This allows to extract an α-factor of around 0.25 from one gate defining the channel to the localised electron states in it. In other words, a 4 mV movement of one gate raises the potential along the one-dimensional channel by 1 meV. We will then usually work for gate voltages below -0.48 V in order to have a fully depleted channel with a floor around a few meV above the Fermi level. The question of the presence of local minima along the 1D channel and the number of charges that occupy them stays open for now.

The proximity of the channel gates to the quantum dots implies first that their influence on the quantum dot will be quite important, and second that the tunnelling out of the dots should be prohibited on the side of the channel. As a consequence, the stability diagrams of the dots should be strongly different from a "standard" one, schematically shown in figure 4.5 (the reader can find a measured "standard" stability diagram in figure 1.14 on page 43). We indeed expect, when V_b is more negative, that the dot will be pushed towards the depleted channel. It is hence further away from the reservoir, the coupling decreases and as a result, the tunnelling time increases. As a consequence, the degeneracy lines on the bottom right-hand side of the stability diagram are not resolved. This is indeed observed, as

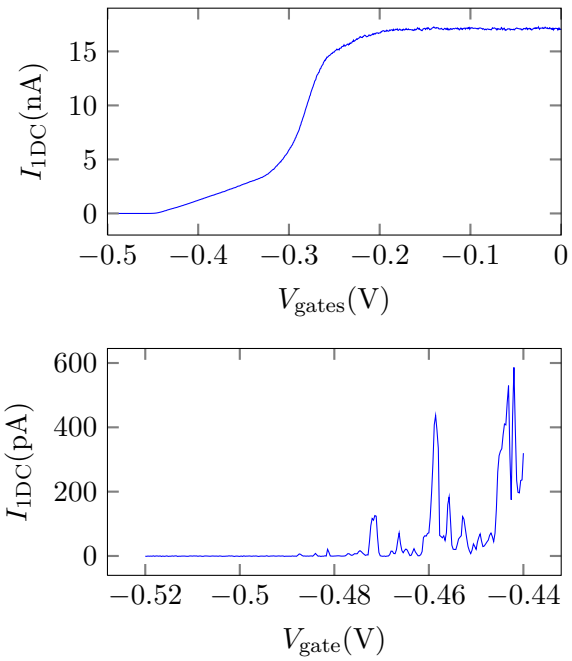

Figure 4.3: Pinch off of the one-dimensional channel. Top panel: measurement taken at 4 K, with 30 µeV bias. Both gates defining the channel are moved symmetrically. Lower panel: close-up on the pinch off below 100 mK, with 30 µeV bias (30 pA ⇔ 1 MΩ). One gate only is swept, the other one is polarised at −0.465 V.

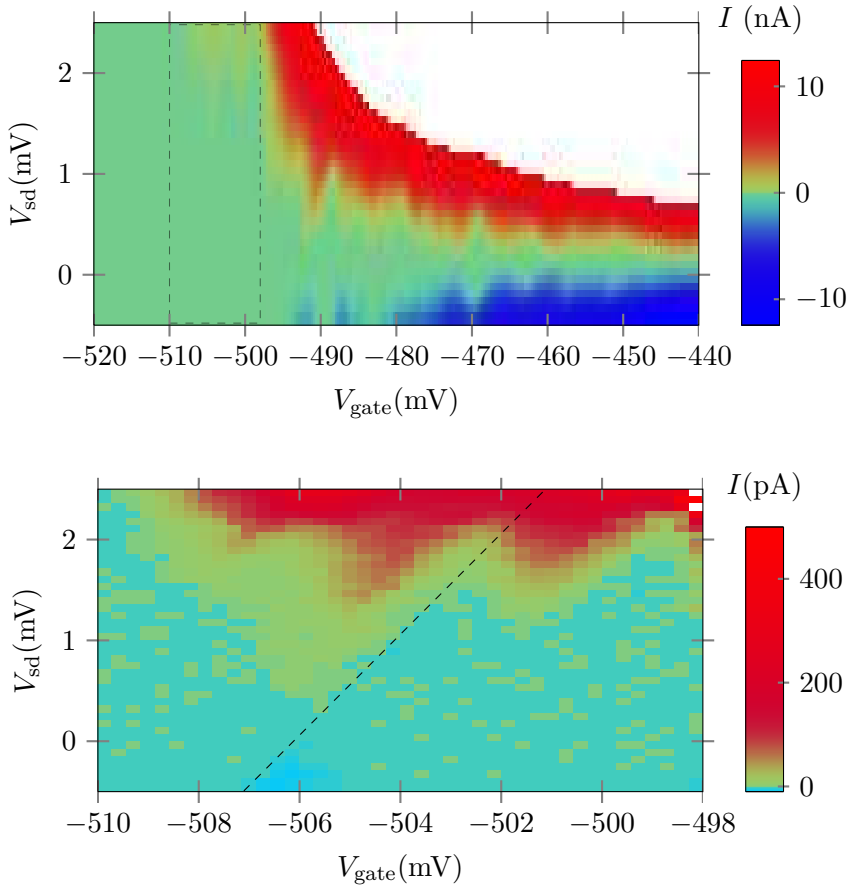

Figure 4.4: Coulomb diamond of the impurities present in the one-dimensional channel. The lower panel is a close-up on the left part of the diamond from the top panel (region delimited by the dashed rectangle). One gate is swept, the other polarised at $-0.465\,\mathrm{V}$. The dashed line on the lower panel corresponds to the slope expected for $\alpha = 0.25$.

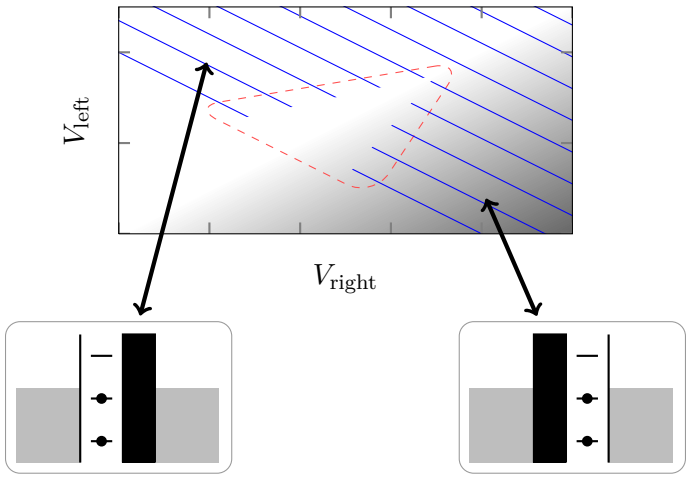

Figure 4.5: Schematic stability diagram. The lines correspond to the $n \to n+1$ electron degeneracies. The dashed red triangle highlights the part of the diagram where the tunnelling events get slower than the sweep time, hence they cannot be measured any more. The shaded region is where the dot is geometrically displaced and more coupled to the right side, as depicted in the lower right panel.

can be seen in figure 4.6. The disappearance of the lines in this part of the stability diagrams supposes that while taking the measurements of figure 4.6, electrons stay in the dot even if their chemical potential is above the Fermi level. This metastability is confirmed if we take the stability diagrams by sweeping the gate voltage V_{b} from more negative to more positive. This case is shown in figure 4.7. We can see extra lines that appear, going from bottom left to top right, in blue. This feature is understood if we follow the gate movements when the measurement is taken: between two scans, the gate "rests" at $\delta V_{\text{b}} = 0\,\text{V}$ for a few tens of milliseconds. During this time, the dot can reach its stable charge point, which is a non-zero charge when $V_{\text{c}} \geq -0.52\,\text{V}$. When starting the sweep, the gate "b" is pushed to $-0.1\,\text{V}$ in a microsecond and the sweep starts a few microseconds afterwards. Since the barrier to the reservoir is slow, the quantum dot keeps a non-zero charge that it looses electron by electron while the escape barrier gets thinner (V_{b} gets more positive). When reaching its stable state, the dot starts loading electrons one by one again and the lines change colour (the derivative of the current with respect to V_{b} changes sign). This observation allows to infer that it should be possible to freeze a charge state of the dot while moving the dot towards metastable charge states. In other words, the slow barrier should give us more freedom to use the dot in metastable charge states, as we shall explore in what follows.

Let us turn towards the injection (or source) dot. We can expect the

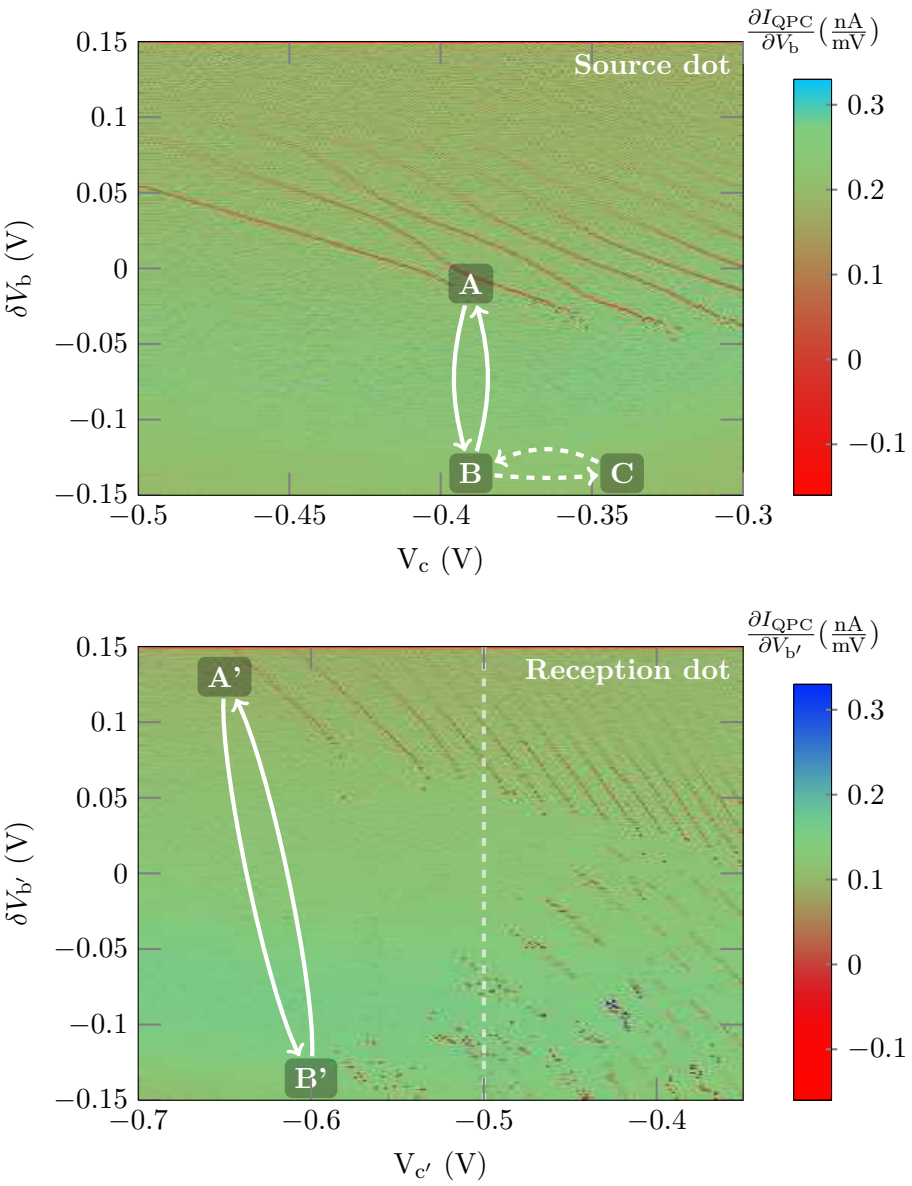

Figure 4.6: Stability diagrams of the two dots. The scans are taken by sweeping $\delta V_{b(b')}$ from positive to negative voltages. Upper panel: injection dot. Lower panel: reception dot. The non-zero background is due to the cross talk from the swept gate to the QPC.

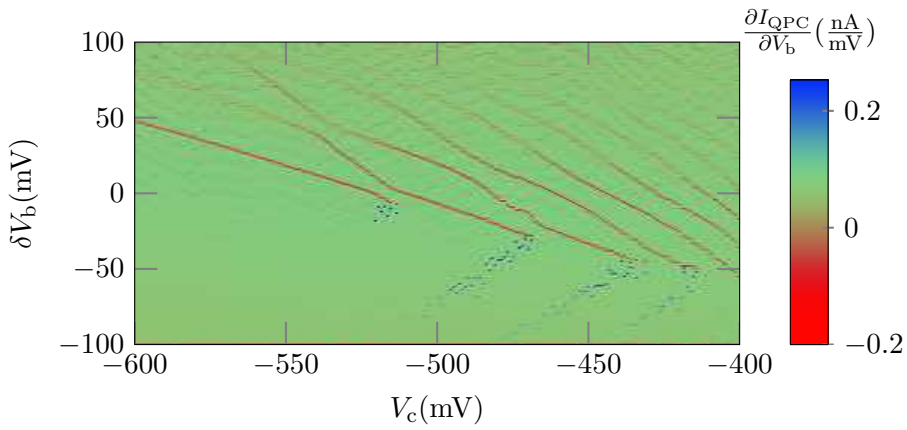

Figure 4.7: Stability diagrams taken in opposite direction. δV_{b} is swept from $-0.1\,\mathrm{V}$ to $0.1\,\mathrm{V}$. Between two sweeps, δV_{b} is put at rest at $0\,\mathrm{V}$ for a few milliseconds and then brought to $-0.1\,\mathrm{V}$ in $1\,\mu\mathrm{s}$.

shape of the potential to be as depicted in figure 4.8a. In this situation, which corresponds to point A on the stability diagram of figure 4.6, the dot can be put in contact with only its reservoir. The correct adjustment of the dot's chemical potential allows to load a single electron into it. The time scale for this loading event will typically be on the order of a hundred microseconds. The determination of this time, faster than the bandpass of our current-to-voltage converters, will be detailed further on.

Once the dot is loaded with one electron, we want to push this electron towards the channel since it will intuitively increase the coupling to it. To do so, we push the voltage V_{b} more negative. Another consequence will be the thickening of the tunnel barrier between the dot and the reservoir. At the same time, the gate will raise the chemical potential of the dot so that the equilibrium charge number should be zero, as depicted on figure 4.8b. Nevertheless, the increased tunnelling time prevents the electron from leaving the dot for a time long enough for it to be measured: we have the time to monitor the dot in a metastable charge state. The time trace we expect for the QPC current during such a sequence is depicted in figure 4.9.

Nevertheless, it is not possible to bring in any number of charges at any arbitrary point of the stability diagram. To get the information on where we can bring how many charges, we proceed to the following experiment: we push the dot in the $n = 2$ region (a bit above point A in figure 4.6) for $\delta V_{\mathrm{b}} = 143\,\mathrm{mV}$ and then push the gate "b" to a voltage $\delta V_{\mathrm{b,push}}$ varied from $143\,\mathrm{mV}$ to $-150\,\mathrm{mV}$. For each value of $\delta V_{\mathrm{b,push}}$, the charge state is measured for more than $100\,\mathrm{ms}$ and presented in figure 4.10. The different regions that appear on this graph show that if δV_{b} is not pushed negatively enough (from

(a) Loading point. The first level of the dot is brought below the Fermi level of the reservoir so as to have a single electron in. This situation corresponds to point A in figure 4.6

(b) Metastable point. The dot is pushed higher in energy, where its stable state is zero electrons. The thickness of the tunnel barrier is so that the dot can be kept up to a second in such a state.

(c) Metastable point. The dot is pushed further in energy than in (b). The tunnel barrier gets thinner.

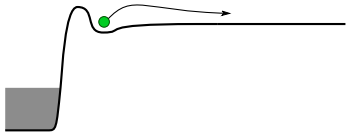

(d) Injection point. The dot is pushed higher in energy than the floor of the 1D channel. The electron is pushed into the channel.

Figure 4.8: Schematic profiles of potential through the injection dot and the one-dimensional channel.

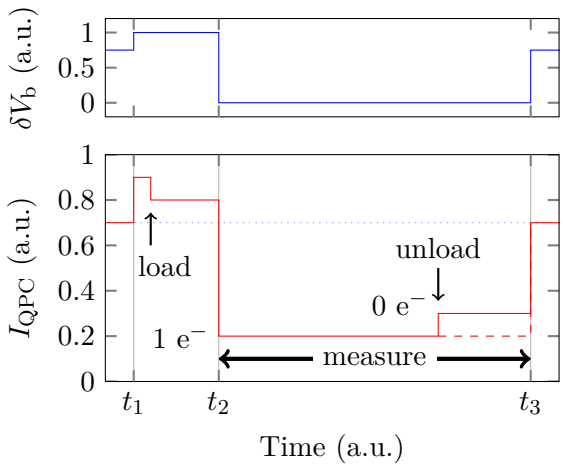

Figure 4.9: Expected time trace for the QPC during a pulse sequence. Time t_1 is the time when the gate is pushed from a rest position to the load position; t_2 is when V_b is made more negative (pushing the electron towards the channel) and at t_3 the gate goes back to its rest position. The current changes at $t_{1,2,3}$ hence correspond to cross talk from the gate movements to the QPC. The load and unload events are pointed by arrows. Note that the load event (between t_1 and t_2) is too fast to be resolved in the experiment. We commonly monitor only the part written "measure".

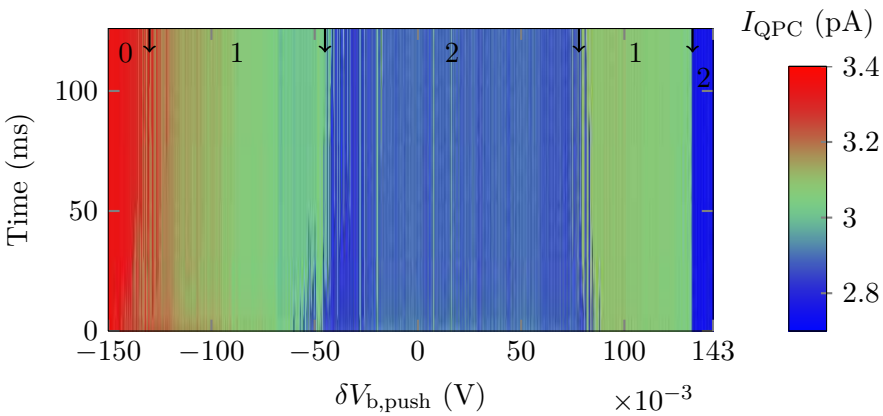

Figure 4.10: Metastability scan. For each trace, the dot is loaded with two electrons (before time = 0 ms) and then pushed higher in energy thanks to V_{b}. The load is done at $\delta V_{\mathrm{b}} = 143\,\mathrm{mV}$. The numbers indicate the number of electrons present in the dot. The transitions between the different fillings are highlighted by arrows. The leftmost regions at 2, 1 and 0 electrons are metastable states. The slight shift in the background is due to the crosstalk to the QPC that is imperfectly compensated for.

90 mV to 130 mV) the escape barrier is still fast and one electron leaves the dot faster than can be measured (3 ms). By pushing $\delta V_{\mathrm{b}} \leq 80\,\mathrm{mV}$, we can see that one more electron is kept in the dot: even though the chemical potential of the quantum dot is made higher than the Fermi level, the second electron stays trapped in the dot. It comes from the fact that the escape barrier becomes slow enough *before* the electron has the time to escape. Upon a stronger push on δV_{b}, the chemical potential of the dot gets too high and the electron starts leaving the dot again. By pushing further than −140 mV in that configuration, we can see that both electrons leave the dot within the millisecond time-scale.

We now expect to be able to take one electron from the Fermi sea and push it high in energy, close to the one-dimensional channel if we set the load point around $V_{\mathrm{b}} = 130\,\mathrm{mV}$ and $\delta V_{\mathrm{b,push}} \simeq -100\,\mathrm{mV}$. We now repeat the preceding sequence with these fixed values. Figure 4.11 shows some QPC traces (upper panel) and the average of 100 time traces (lower panel). We can see that an exponential decay, characteristic of tunnelling is recovered and a tunnelling time longer than half a second could be measured.

We hence are able to quench the charge state of the dot. This allows, for example, to plunge the dot in a region where the barrier is thin for a time much shorter than a millisecond, quench its charge state and then measure it. The outcome is an integer number of charges for each trial. Each wait time (period from t_1 to t_2 in figure 4.9) is repeated a large number of times

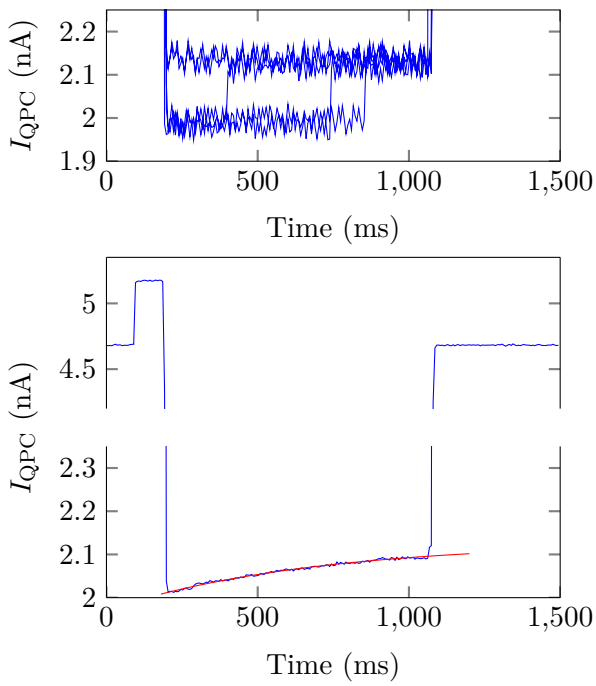

Figure 4.11: Decay characteristics of the injection dot. Top: five time traces of the dot in a metastable position. The exit events are clearly stochastic. Bottom: average of 100 such traces. The exponential decay of the quantum dot brought in the metastable position is clearly visible. The characteristic time of the red exponential fit is 670 ms. The load event is unresolved.

(typically 100 to 1000 times) and the average value is plotted versus the wait time. The resulting curve should be an exponential with the characteristic time for the loading tunnel event. It is to be noted though, that it presents some limitations, namely it is necessary to be sure that no extra charge will enter into the dot during the travelling from the probed configuration to the measuring configuration and that none of the charges trapped in the dot have time to leave it. This means that we will have the ability to explore the states shown in figures 4.8b to 4.8d.

The stability diagram for the reception dot shown figure 4.6 confirms the metastable picture: the scans are taken from top to bottom, at a rate of 3 ms per point. Following the $\delta V_{\mathrm{b}'}$ sweep for $V_{\mathrm{c}'} = -0.5\,\mathrm{V}$ (marked by a dashed line), the dot goes from 7 electrons to 3 electrons, losing one charge each time it crosses the Fermi level. Nevertheless, for the remaining 3 electrons, the barriers get quickly much slower and the dot is kept in its metastable state. When $\delta V_{\mathrm{b}'}$ reaches $-0.75\,\mathrm{V}$, the electrons start to find a way out, either back to the reservoir or into the 1D channel.

In conclusion to this section, we have the possibility to take one electron from the reservoir and push it high in energy into a position that we expect to be well coupled to the one-dimensional channel.

4.3 Electron injection

Now that we are able to push an electron high in energy and keep it there for some time, we have to send it into the channel. The naive approach of just pushing the electron in the channel being bound to leave electrons trapped along the channel, we directly try to get the electron caught in a dynamical quantum dot.

The proposed experiment is then as follows: we repeat the sequence leading to figure 4.10 but in addition we will now send a SAW burst 50 ms after getting in the metastable position. As can be seen in figure 4.12, the following charge changes are observed: $1 \to 0$, $2 \to 1$ and $2 \to 0$. These first traces allow to see that the SAW allows to stimulate the exit of one or more electrons from the quantum dot.

From figure 4.12, we can be tempted to work at different positions for $\delta V_{\mathrm{b,push}}$: around 100 mV or -110 mV, which seem to be the two values for which one electron can be extracted with high probability from the dot. However, since the exit probability of one electron between 50 mV and -90 mV does not seem so high, one can expect that we go from a situation where the electron leaves to the reservoir (positive side) to a situation where the electron is sent into the channel. In order to have the largest chance of success, we will investigate directly the more negative side of the parameter.

It is to be noted that once the metastable working point is chosen, we have the possibility to change the charge state of the dot at this point by

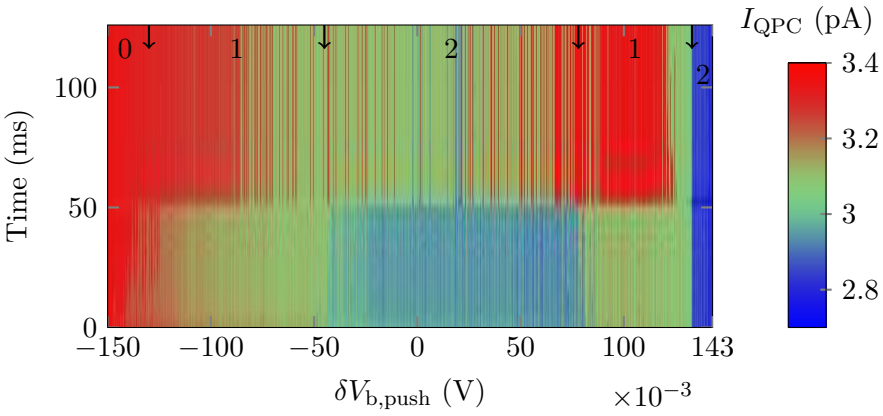

Figure 4.12: SAW-induced emptying of the injection dot. The sequence is the same as in figure 4.10 but a SAW burst of 250 ns is sent after 50 ms in the metastable position. We can see that one or two electrons are expelled with reasonable efficiency.

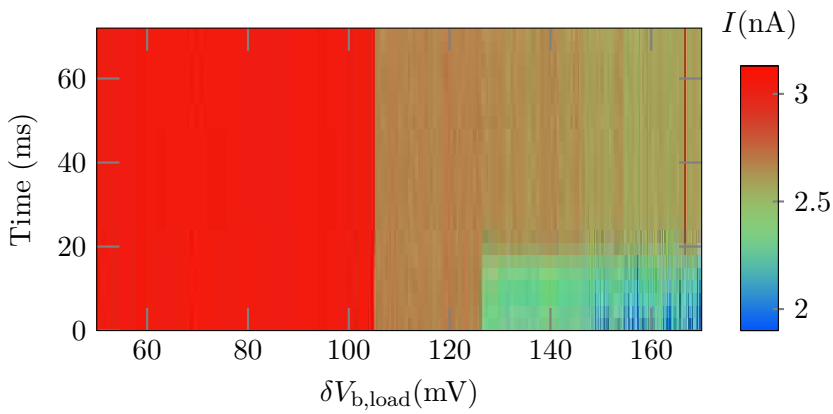

Figure 4.13: Change in the charge number of the dot in the metastable state when changing the loading point $V_{b,load}$. The dot can here be loaded with 0 ($V_{b,load} < 105$ mV), 1 ($V_{b,load} \in [105; 125]$mV) or 2 electrons ($V_{b,load} \in [125; 150]$mV). It is possible to load 3 electrons for $V_{b,load} > 150$ mV, but this charge state decays in a few milliseconds in this configuration. Data taken for $\delta V_{b,push} \simeq -50$ mV and the SAW burst is sent 20 ms after arriving in the metastable position. The charge state is measured only in the metastable position.

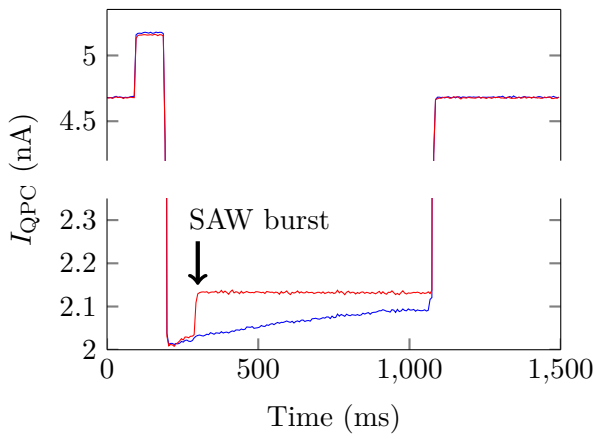

Figure 4.14: Charge state decay of the dot in two situations: one is the spontaneous decay (blue curve, same data as in figure 4.11), the other corresponds to a situation where a SAW burst of a 250 ns is emitted 50 ms after going into the metastable position. The decay becomes forced at the precise time when the SAW is generated.

moving the loading point, as shown in figure 4.13.

To get a better idea of the extraction efficiency, we realise the following experiment: we charge one electron in the injection dot, push the electron in the metastable position ($\delta V_b \simeq -110\,\mathrm{mV}$) and send a SAW burst. The dot charge state is measured before and after the SAW burst. Results of such an experiment are shown in figure 4.14. It can be seen that before the SAW burst, the dot still shows a spontaneous exponential decay. After the SAW burst, the dot is found empty with a very high probability. We can therefore infer that the SAW efficiently gets the electron out of the dot. Nevertheless, a few points still have to be addressed. First, we have to figure out whether the electron is actually sent into the channel or back to the reservoir. This will be discussed in the next section of this manuscript. Second, the microscopic picture is still undefined: does the electron get adiabatically loaded into a dynamical dot? Or is it that the periodic lowering of the barriers due to the SAW accelerates the decay, as suggested in the work of Kataoka *et al.*?[18]

4.4 On demand single-electron transport

As stated above, a major question to be answered is whether the electrons, under the influence of the SAW, exit the dot on the side we would like. To find out which way the electron leaves, we set the reception dot to catch the electron on the other side. Indeed, correlations between "one electron left the injection dot" and "one electron entered the reception dot" will strongly sustain the fact that the electron was indeed dragged along the

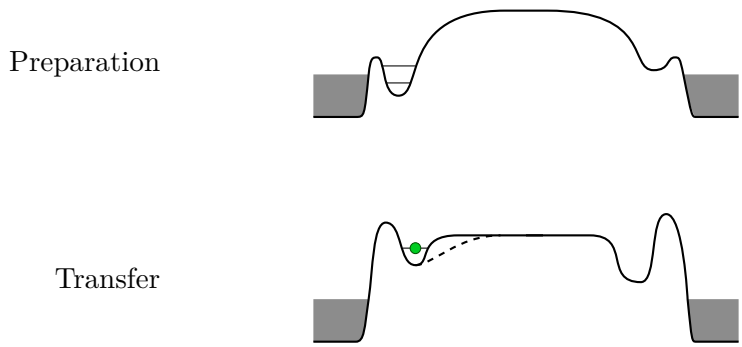

Figure 4.15: Schematic potential profiles along the 1D channel and the two dots during the sequence. During the preparation, the injection dot (left) is loaded with one electron and the reception dot (right) is emptied. For the injection and reception, the dots are brought higher in energy and strongly isolated from the reservoirs.

channel.

In order to measure such correlations, the reception dot has to be prepared and positioned adequately. Namely, it is emptied at the beginning of the sequence and then brought into a position where it is ready to host one electron. It is to be noted that the incoming electron, if caught will put the dot in a metastable state. These configurations for the reception dot are attained at points A' and B' of the stability diagram in figure 4.6. The corresponding shapes for the potential along the 1DC and the dots are shown in figure 4.15.

The complete sequence we follow is then:

1. empty reception dot (A'),
2. bring reception in reception state (B'),
3. load injection dot (A),
4. push injection dot to the metastable state (B),
5. measure the charge states of the dots,
6. send SAW burst
7. measure the charge states of the dots,
8. empty reception dot (A'),
9. send a few SAW bursts to clean the channel of charges eventually trapped. This step was only used during the tuning of the system.

We usually only record the QPC traces from step 5 to step 7, which correspond to the lower panel of the graph in figure 4.14. Indeed, the *huge* gate movements realised to go from the preparation state to the transfer state require to move the QPCs gates in order to keep them on a sensitive

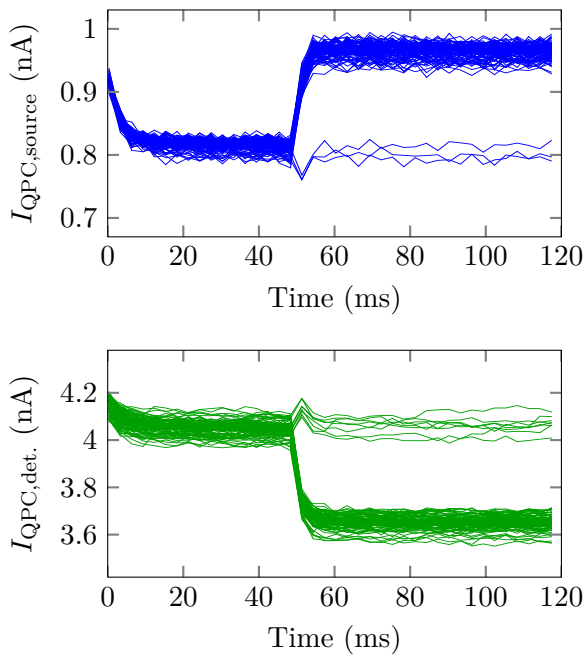

Figure 4.16: 101 superposed time traces for both source-dot QPC and reception-dot QPC. The levels for 0 or 1 electron are clearly defined for both injection and reception detectors.

polarisation point and not saturated, and gate movements take time (16 µs each). The resulting time traces (101 of them) of these events are shown in figure 4.16. We can see that no events (load or unload) happen during the time interval before or after the SAW is sent, around $t = 50$ ms. The other important point is that the two levels at 0 and 1 electron are nicely defined and their separation is much bigger than the noise level of the system. The total probability to extract the electron from the injection dot is rather high, around 97 %, and the one to catch an electron in the reception dot is around 92 %. Nevertheless, these high probabilities could be achieved *via* parasitic phenomena, e.g. the source dot decaying to the source reservoir and the reception dot getting loaded from the reservoir. The argument saying that the reception dot is high in energy compared to the Fermi level being inadmissible since we cannot actually measure this. Indeed, the only way to measure this is to check the stable charge number in the given position. Nevertheless, the point of this configuration is to have a huge barrier between the dot and the reservoir; the long tunnelling time hence prevents us from measuring the stable state of the dot at this working point. The way around this is to measure the actual correlation between injection events and reception events.

We now turn to the correlations between injection and reception events.

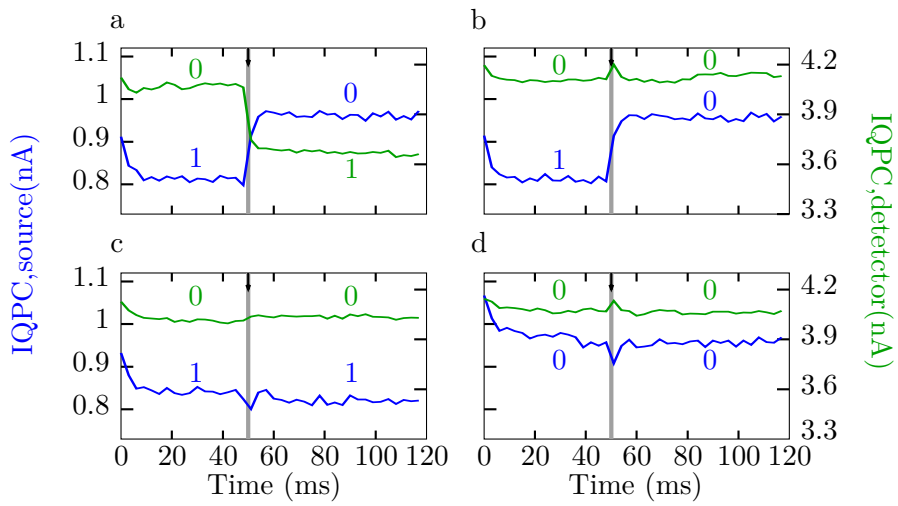

Figure 4.17: Typical time traces for the different situations of success of the transfer.

The situations we most commonly face are shown in figure 4.17. First, both the positive events happen: one electron exits the injection dot and one enters the reception dot (figure 4.17a). Second, one electron exits the injection dot, but none enters in the reception dot (figure 4.17b). Figures 4.17c and 4.17d both show a situation where no charge change is detected during the whole sequence, once with the injection dot carrying one electron (4.17c) and once without (4.17d). By counting these situations, we can pull out from the data the relevant statistical information about the success of the transfer. However, if we want to actually prove that the transfer happens, we have to get the same information in control situations. The different situations considered are the following:

(i) the injection dot is loaded and a SAW is generated,

(ii) the injection dot is loaded but the SAW is *not* generated,

(iii) the injection dot is *not* loaded but the SAW is generated,

(iv) the injection dot is randomly loaded half of the time, the SAW is generated,

(v) the injection dot is randomly loaded $\frac{1}{6}$ of the time, the SAW is generated.

Situation (i) is the "working" situation, used to quantify how efficient is the overall process. The other situations each are intended to check that a specific class of parasitic processes does not occur. (ii) checks that nothing happens without a SAW burst.[1] Situation (iii) intends to verify that the

1. By tuning adequately the experimental gate sequence, transfers without SAW could

	SAW				
Event	On	Off	On	On	On
$N_{1\text{xxx}}$	9841	10,001	16	5154	1462
$N_{10\text{xx}}$	9408 (95.6 %)	0 (0 %)	15 (94 %)	4954 (96.1 %)	1395 (95.4 %)
$N_{100\text{x}}$	9128	0	14	4807	1349
N_{1001}	8393 (91.9 %)	0 (0 %)	14 (100 %)	4417 (91.9 %)	1244 (92.2 %)
$\sum_{\beta+\delta>\alpha+\gamma} N_{\alpha\beta\gamma\delta}$	0	1	0	0	0

Table 4.1: Statistics for the different experimental situations. The statistics is out of 10,001 repetitions. The indices $N_{\alpha\beta\gamma\delta}$ are defined in the main text, page 110. The targeted load probabilities (related by $N_{1\text{xxx}}$) are 1, 0, $\frac{1}{2}$ and $\frac{1}{6}$ The percentages are all relative to the previous line results.

electron caught in the reception dot does not come from the reception-side reservoir. Indeed, by not loading the injection dot, the number of reception events is expected to stay the same if the electrons were systematically taken from the reception side, and to not vanish if it sometimes happens. Finally the situations (iv) and (v), are here to sustain that the electrons do not stay trapped in the channel before getting expelled in the next run into the reception dot. One could indeed think of a chained mechanism in which one electron gets pushed into the channel on each SAW burst and the electron already present gets ejected into the reception dot—the very same mechanism could work with any number of electrons caught in the channel. However, if the electrons are only weakly trapped in the channel, then getting a few extra SAW bursts without an injected electron should increase the number of times an electron gets caught when none is injected. To build up statistics on the experimental realisations, we compute for each time trace how many electrons were present before and after the SAW burst. This is achieved by comparing the average value of the signal before (resp. after) the burst to threshold values defined for both dots. The curves are checked visually to ensure no events (load or unload) happen outside of the SAW burst. The value $N_{\alpha\beta\gamma\delta}$ is the number of traces for which the source dots had α electrons before and β after the SAW burst, and the reception dot γ before and δ after. An 'x' index means we sum all the possibilities for this index.

Table 4.1 sums up the values of $N_{\alpha\beta\gamma\delta}$ for the different experimental situations described previously. We can extract from this table that the

be witnessed. However, their rate of success was fairly weak, not to say exceptional ... it has been observed less than 10 times over a few tens of thousands of trials.

events counted are strongly dependent on the presence on the SAW. Indeed, comparing situations (i) and (ii), one can see that no electron leaves the injection dot without the SAW. Moreover, only one electron entered the reception dot in this situation. Secondly, the fact that we never end up with more electrons in the system than we start with shows in the situation (iii) that the electrons caught in the reception dot are related to the injected electrons. If the electrons were entering directly from the reservoir into the reception dot, we would expect the number of bad events to increase significantly, while it stays at 0. Finally, if the electrons were staying trapped in the channel, we would expect the success rate to drop and/or the number of bad events to rise if we were to load the injection dot only for part of the attempts. In such a situation, the electron trapped in the channel at attempt n could be released at attempt $n + 1$, when the injection dot is not loaded, which would increase the number of bad events. The similarity in the success rate and the few bad events in situations (iv) and (v) hence strongly suggests that it is indeed the same electron that gets extracted from the injection dot and caught in the reception dot for a given attempt, with high reliability. Nevertheless, the possibility that one or a few electrons are strongly trapped in the channel and exchange with the electron that we transfer cannot yet be ruled out. This point should be addressed by further experiments in which we propose to tag the electrons by preparing their spin and measuring it on the other side. By letting a time longer than the spin relaxation time between the attempts, one should be able to conclude unquestionably this point.

4.5 Note about the spin

The setup used during my Ph.D. allows only to apply a perpendicular field to the sample. In order to read the spin of a single electron, one needs to apply a magnetic field such that the Zeeman splitting $g\mu_{\mathrm{B}}B$ is large compared to the electron temperature. For an electron temperature of 150 mK, this means applying an external field large compared to 600 mT and the single-shot measurement was actually proven with fields above 8 T. We were unable to measure a spin signature at fields up to 3 T. Let us also mention that in perpendicular magnetic field the sample enters the quantum-Hall regime around 1 T as can be seen in figure 4.18, which could perturb the spin measurement. In addition, above 3 T, the system is in the last Landau level which is supposed to be spin-polarised. It thus gets much more complicated to prepare a $|\downarrow\rangle$ state. In order to be able to investigate the spin of a single electron without entering in the quantum Hall regime, a sample holder that allows to apply a parallel magnetic field has been designed and should soon allow to investigate the consequences of the transfer on a single electron spin.

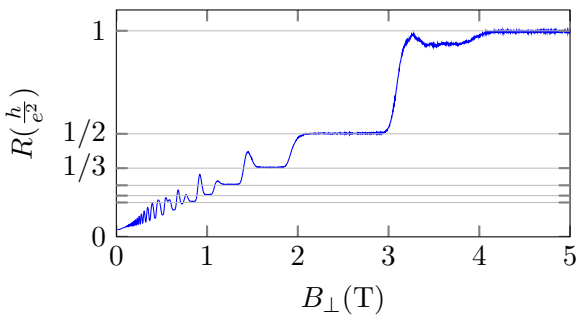

Figure 4.18: Two-terminal resistance $R = R_{xy} + R_{xx}$ of the sample *vs.* the externally applied magnetic field. The horizontal lines correspond to integer fractions of the resistance quantum $R_\mathrm{K} = \frac{h}{e^2} = 25.8128\,\mathrm{k\Omega}$. Measurements realised with a bias of 200 µeV.

The long-term goal of the experiment is to transport spin. It will be necessary to be able to measure an electron spin when the sample is under the conditions required for the transfer: large gate movements and SAW generation. We can estimate the electronic temperature of the sample during the transfer process. From table 4.1, we can see that the number of times the dot is indeed loaded with one electron (N_1xxx) goes from 100 % to 98 % when the SAW is actually sent. Since the loading point is around midway from the 0–1 and 1–2 electrons degeneracies, we can estimate that the system is around 1 meV away from the degeneracy. We can then estimate the electron temperature T_el by assuming that these 2 % errors come solely from the spread of the Fermi level:

$$0.02 = \frac{1}{1 + \exp\frac{1\,\mathrm{meV}}{kT_\mathrm{el}}}, \tag{4.1}$$

where k is the Boltzmann constant. This gives $kT_\mathrm{el} \simeq 250\,\mu\mathrm{eV}$, that is $T_\mathrm{el} \simeq 2.5\,\mathrm{K}$. It is then important to remark that in order to have a Zeeman splitting larger than the thermal energy in the reservoir, a magnetic field larger than 10 T has to be applied. The preceding estimation has, however to be considered with caution: a measure of the charge state of the dot thanks to the QPC while scanning a degeneracy-line seems to indicate a lower electron temperature, around 200 mK, as show in figure 4.19 [65]. The magnetic field needed to Zeeman-split the levels at energies where the Fermi distribution is below 5 % and above 95 %, that is a 10 % error induced in the readout, is of order 5 T. The question of the electronic temperature in the reservoirs when one electron is transferred stays unclear and will have to be investigated in more details.

Nevertheless, since one of the ultimate goals of the experiment is to generate distant entangled pairs of electrons, the idea of working with two

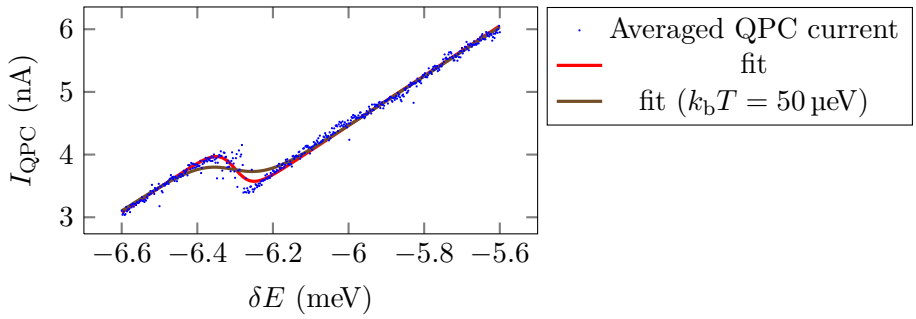

Figure 4.19: The QPC current is averaged over a few tens of ms for each point. The shift in energy is estimated from the α-factor determined previously. The first fit leads to an electronic temperature of 200 mK. The second fit was forced with an electronic temperature around 500 mK which clearly corresponds to an upper bound. The significant noise on the data comes from an averaging time not long enough compared with the tunnelling time to the reservoir.

electrons in a singlet (or triplet) state gained ground: the singlet and triplet states are separated in energy by an amount equal to the single-particle splitting of the dot with no magnetic field. The basic scheme would be as follows: prepare a pair of electrons in either triplet or singlet state, send the pair of electrons and measure whether it is a singlet or a triplet. This scheme would have to be repeated with the addition of different dead times in order to probe relaxation times. The protocol, which will be more detailed further on will most likely need two extra ingredients. First, we will need to work with two electrons. Second, we may need to trigger the transfer on a time-scale faster than T_2^*. Since the latter is on the order of a few tens of nanoseconds in static quantum dots, we will use it as a reference and try to trigger the experiment on the nanosecond time-scale.

4.6 Nanosecond triggering

The results shown so far lack an accurate triggering in which the transferred electron gets extracted from the injection dot anywhere within the 140 ns of the SAW burst—the probability being higher at the end of the burst though, as will be discussed further. As stated in the previous section, we want to be able to trigger the transfer on the nanosecond time scale. The first direction to follow is to reduce the SAW duration. The SAW burst could be shortened to 65 ns, below which an efficient transfer could not be realised. This value comes from the limited bandwidth of the IDT, as will be discussed further. Another possibility is to modify the potential of the dot. The idea is to protect the electron from leaving the dot during most of

the SAW burst and "expose" it to the SAW only during the shortest possible amount of time. To do so, the injection sequence is slightly modified. First, the barrier between the dot and the channel has to be made thicker. This is achieved by making V_C more negative during the wait state before sending the electron. This corresponds to moving point B further left in figure 4.6. Then, a fast pulse on gate C allows to bring the injection dot to point C, where the electron should be closer and more coupled to the channel, and back again. This "kick" will get the electron out of its protected state for the duration of the gate pulse. The electron should then be able to leave the dot only during this short gate pulse and the transfer resolution should be independent of the SAW duration. Figure 4.20 shows the influence of

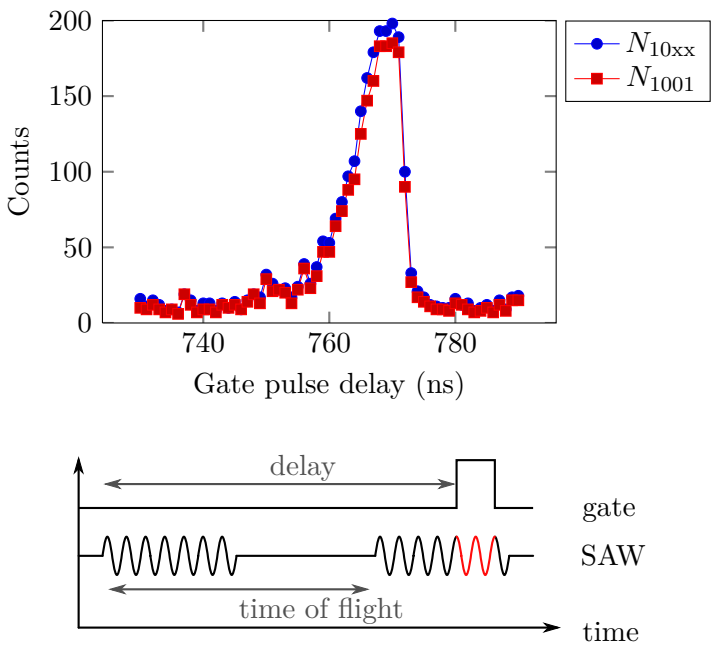

Figure 4.20: Evolution of the transfer success number N_{1001} as a function of the delay between the SAW generation and the 1-ns pulse on V_C, out of 200 repetitions. The SAW duration is 65 ns. Lower panel: timing schematic of the experiment. The time of flight is the time needed for the SAW to travel from the IDT to the centre of the sample – around 2 mm.

the delay between the time when the SAW is generated and when a 1 ns positive-voltage pulse is applied on gate C. An overall offset of 700 ns comes from the time lag of the SAW: it needs to travel the 2 mm from the IDT to the dot at $\simeq 3000\,\mathrm{m\,s^{-1}}$, as shown schematically in the lower panel of this figure. We can see from these data that the injection success rate ($\frac{N_{10xx}}{N_{tot}}$) is close to one if the nanosecond pulse is adequately placed, close to zero oth-

erwise. This shows that, in this configuration, the trigger pulse is needed in order to achieve high injection rates. In other words, the electron is injected with a high probability only during the nanosecond pulse. We hence have the possibility to trigger the transfer of the electron within a given nanosecond, which corresponds to 3 minima of the SAW. It is to be noted that the nanosecond limit seems purely technological: a faster arbitrary waveform generator synchronised with the RF source should allow to always place the electron within the same minimum of the SAW, whereas we now place it within two to three minima.

The shape of the curve in figure 4.20 can be qualitatively understood with the following model. We assume that the RF burst has a finite rise time τ_{RF} due to the gating circuitry. The IDT response is modelled with finite response time τ. The resulting SAW envelope will have a rising "edge' which results from the combination of τ and τ_{RF}. The fall time will be assumed to be only limited by the IDT rise time τ. Note that the asymmetry between the rising and falling edges is the key ingredient to reproduce the asymmetry in the success-rate curve of figure 4.20. We hence have a SAW envelope $A(t)$:

$$\begin{aligned} A(t) &= \theta(t) \times \theta(t_0 - t) \times \mathrm{rise}(t) \\ &\quad + \theta(t - t_0) \times \mathrm{rise}(t_0) \times \mathrm{fall}(t - t_0), \end{aligned} \tag{4.2a}$$

$$\mathrm{rise}(t) = 1 - e^{-\frac{t}{\tau}} + \left(\frac{\tau}{\tau_{\mathrm{RF}}} - 1\right) \times e^{-\frac{t}{\tau_{\mathrm{RF}}}}, \tag{4.2b}$$

$$\mathrm{fall}(t) = e^{-\frac{t}{\tau}}, \tag{4.2c}$$

where $\theta(t)$ is the Heaviside step function, t_0 is the duration of the burst, τ_{RF} is the rise time of the RF gating circuit (see section 3.2.2) and we normalise the amplitude of the SAW to 1. We assume that the probability $p(A)$ for the electron to be extracted from the dot within 1 ns when irradiated with a SAW of amplitude A is a smooth step function modelled by a Fermi function:

$$p(A) = \frac{1}{1 + \exp(-\frac{A - A_0}{\delta A})}, \tag{4.3}$$

where A is the SAW amplitude, A_0 is the threshold for an efficient extraction and δA is the width of the threshold. Using this model, the data from figure 4.20 can be roughly fitted as shown in figure 4.21, with the function:

$$\mathrm{N}_{10\mathrm{xx}}(t) = p\left(A(t - t_{\mathrm{flight}})\right), \tag{4.4}$$

where t_{flight} relates the SAW propagation delay from the IDT to the center of the sample. The duration of the pulse is fixed at $t_0 = 65$ ns. The parameters extracted from the fit are:

- the threshold amplitude (relative to the steady-state amplitude for a long RF burst) $A_0 = 0.81$,

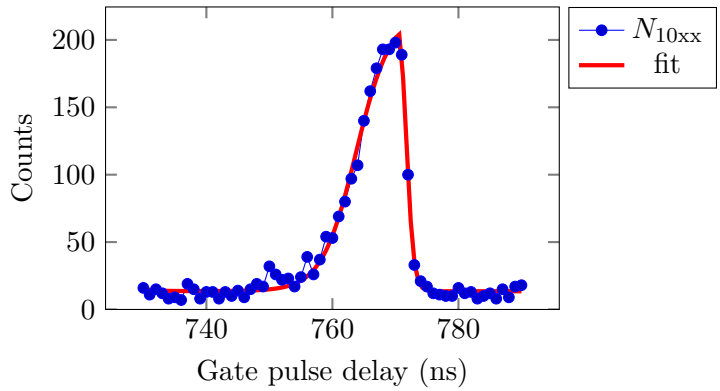

Figure 4.21: Fit on the send events N_{10xx}.

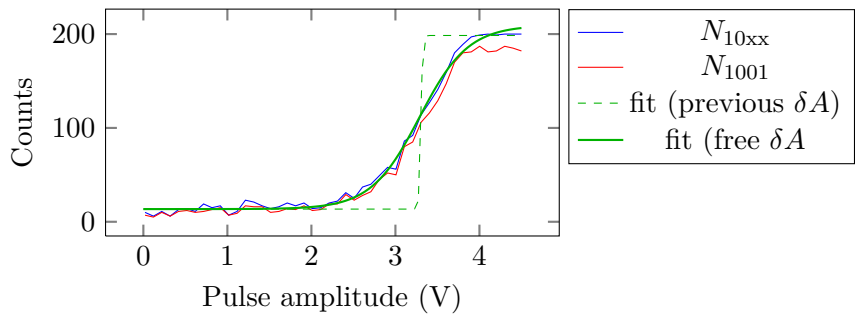

Figure 4.22: Injection and transfer rates as a function of the nanosecond-pulse amplitude for a gate pulse delay of 765 ns. A clear on/off behaviour can be seen. The amplitude is the room temperature amplitude of the pulse; its amplitude is divided by 15 along the RF line for thermalisation and filtering purposes.

- the width of the threshold $\delta A = 0.012$, *i.e.* 1.5 % of A_0,
- the rise time of the IDT $\tau = 37$ ns,
- the delay time $t_{\text{flight}} = 705$ ns.

A background has been added to take into account the low amount of transfer that occurs without the nanosecond pulse. The agreement between this simple model and the data tends to confirm the existence of a threshold in $p(A)$, which is in accordance with the fact that the SAW has to overcome the potential gradient generated by the fixed gates. This interpretation is consistent with results from the Cambridge group [66, 67].

We can now investigate the influence of the nanosecond-gate-pulse amplitude. We set the delay of the pulse so that the transfer rate is maximum on figure 4.20 and take transfer-rate statistics as a function of the amplitude of the pulse. We can see that the transfer rate depends critically on

the pulse amplitude. We expect that the voltage V_c affects the potential gradient the electron has to climb to exit the dot, as depicted in figure 4.23. In other words, at a given set of parameters, the SAW can only drag the

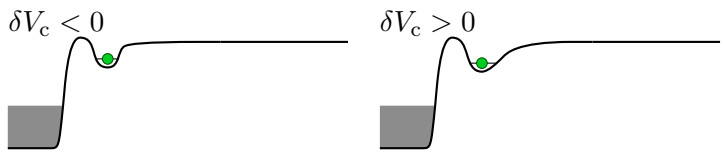

Figure 4.23: Potential shapes for the injection dot for V_c more (left) or less negative (right). The dotted line emphasizes the potential gradient for the case where V_c is more negative.

electron along a limited potential slope. Getting V_c more positive makes the gradient smaller. The simplest possible model is a linear dependence between the gate voltage and the potential gradient. When the pulse amplitude reaches 3 V, the potential gradient becomes small enough for the electron to be dragged by the SAW and the transfer is restored. The fit in figure 4.22 corresponds to the step function of equation (4.3) with a linear mapping between the threshold amplitude and the pulse amplitude with the slope of the linear dependence as the only free parameter:

$$A_0(V_{\text{pulse}}) = a \times V_{\text{pulse}} + b \qquad b = 0.81 - 4a, \tag{4.5}$$

where b is determined such that the threshold amplitude for a 4 V pulse corresponds to the one determined from the fit of the data in figure 4.21. The dashed green line corresponds to the fit with a as free parameter. We can see a clear discrepancy between the model and the data presented in figure 4.22. By letting the width δA be a free parameter for the fit, the fit gives the green solid line with $\delta A = 0.33$ and $a = 1.13$ which is in much better agreement with the data. The most likely explanation for this discrepancy in the values of δA for the previous two experiments is the fact that the offset on the gate voltage is important—4.5 V at room temperature correspond to around 300 mV on the gate—which implies a non linear dependence of the gradient with respect to the gate voltage. In the end, the model developed here allows to capture part of the physics behind the injection process. Nevertheless, a more precise model of the interaction of the SAW and the dot has to be built in order to have a predicted shape for the step function and to actually analyse the values of a, A_0 and δA. The latter is of particular interest in the determination of the relevant physics behind the width of the step function: does the electron thermally jump above the SAW or is it mostly tunnel effect through the SAW potential?

4.7 Influence of the SAW parameters

We now turn to the parameters of the SAW itself and show how they influence the transfer success rate. Note that the next two experiments were realised without a nanosecond pulse. A natural parameter to examine is the SAW amplitude. Indeed, at zero amplitude, we do not expect much to happen. The figure 4.24 shows the increase in the injection rate when

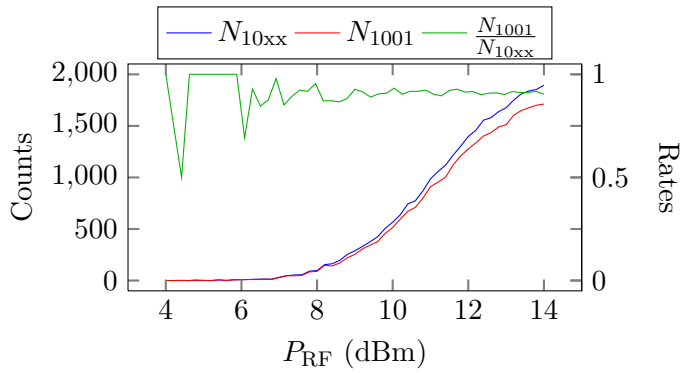

Figure 4.24: Influence of the RF power on the transfer rates. The power indicated is the power received by the IDT. SAW duration was 140 ns. Note that the noise on the rate $\frac{N_{1001}}{N_{10xx}}$ for the lower powers comes from the fact that N_{10xx} drops to zero.

the SAW amplitude is increased. Note that if corrected to be plotted as a function of the amplitude of the SAW instead of its power the curve keeps an equivalent shape. This curve supports the preceding interpretation: the higher the RF power, the higher the electric field generated by the SAW and the higher the probability to extract the electron from the quantum dot. We find again a behaviour with a threshold: below a given amplitude the electron cannot get extracted from the dot, while the electric field overcomes the potential gradient for higher SAW amplitudes.

We can now use the maximum RF power we just studied and make the burst length shorter. The general trend is that a shorter SAW burst makes the injection less efficient as can be seen in figure 4.25. Again, the slowly rising SAW envelope—see figure 3.4—can be the source of the shape seen in figure 4.25: by making the burst shorter, the amplitude reached by the SAW is smaller and the electron has less chances to get extracted from the dot. It is to be noted that from figure 4.24, the switching from no transfer to a high-efficiency transfer requires a change of around 6 dB in the RF power, that is a factor of 2 of the SAW amplitude. From figure 4.25, the SAW burst has to be lengthened from 100 ns to 140 ns to get the same switching. If we take the previous estimate of $\tau \simeq 40$ ns for the rise time of the IDT then the SAW amplitude grows by 5 % in the range 100 ns to 140 ns.

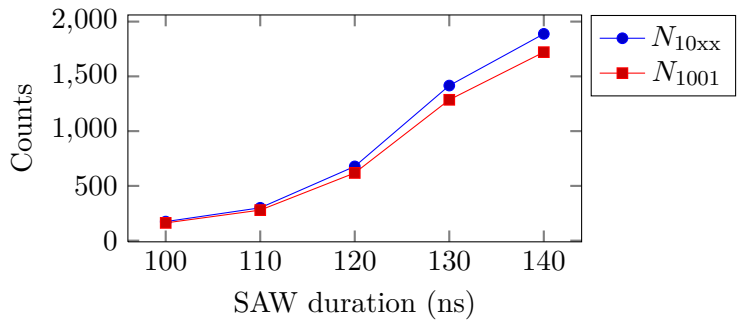

Figure 4.25: Injection and transfer counts as a function of the SAW burst duration. Note that this is the gate duration of the RF circuit and that the SAW signal envelope is slowly rising in time—see figure 3.4, section 3.2.2.

This amplitude change necessary for switching the transfer efficiency is in reasonable agreement with the one determined from figure 4.21. However, this seems in strong disagreement with the factor 2 coming from figure 4.24. A major ingredient to take into account is the fact that the injection rate of figures 4.24 and 4.25 does not represent the injection probability during a short amount of time (p in the previous section) but the integrated success rate SR:

$$\mathrm{SR}(t) = \int_0^t p\left(A(t')\right)\left(1 - \mathrm{SR}(t')\right)\,\mathrm{d}t', \tag{4.6}$$

where the SAW duration t_0 is encoded in the function $A(t)$. $\mathrm{SR}(t)$ represents the total probability for a successful injection after a SAW irradiation time t. The success-rate plots without nanosecond pulse actually correspond to $\mathrm{SR}(t \gg t_0)$. This model will surely allow to reproduce the data presented in figures 4.24 and 4.25.

We now turn to time-resolved measures of the injection process. We use the nanosecond triggering developed in the previous section in order to increase the injection efficiency during a nanosecond. This allows us to scan the response of the system to the SAW at different points of the SAW burst, in the exact same way as what was presented in figure 4.20. Figure 4.26 presents these transfer-efficiency scans for different SAW parameters. From the graphs (a) and (b), where the RF power has been changed, we can see that for a SAW amplitude divided by two (-6 dB in power), the transfer rate drops by 80 %, which confirms the data of figure 4.24. Of particular interest are graphs (b) and (c): the 10 ns increase of the burst duration is directly reflected in the time at which the process falls. It is to be noted that the model described in the previous section does not allow to consistently fit the three curves of figure 4.26. This fact suggests that more ingredients are needed to model the response of the system. One possible origin would

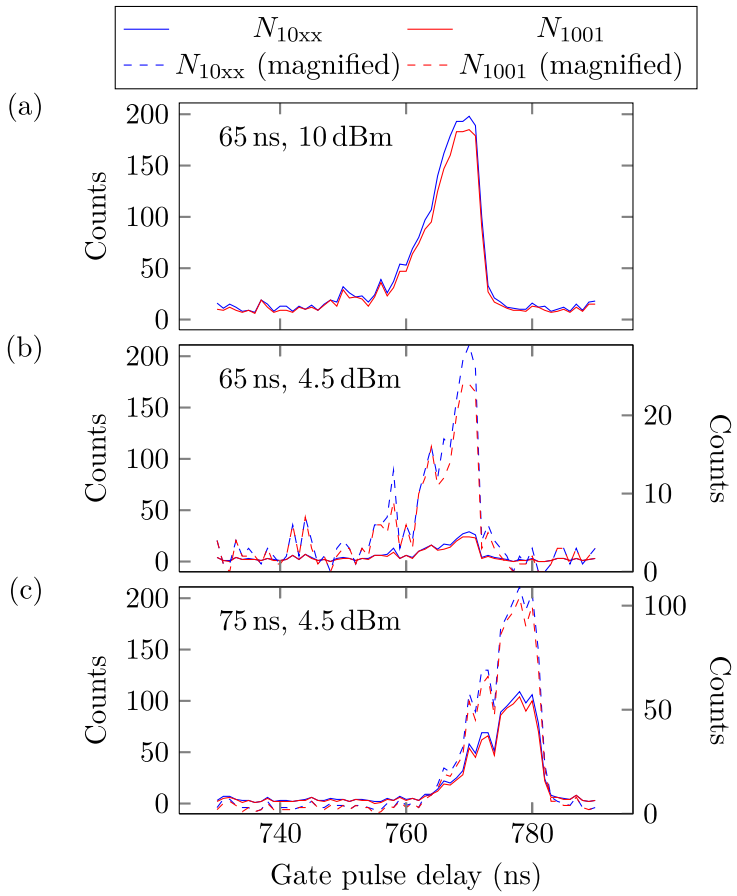

Figure 4.26: Direct comparison for different SAW amplitudes and SAW burst length. All data represent 201 repetitions. The solid lines refer to the left axis, all on the same scale. The dashed lines refer to the right axis, scaled for better details.

be the fact that the SAW could raise the electron to higher-energy orbitals. This could result in a lower amplitude needed when the SAW is generated for a longer time.

In the end, some more systematic studies and modelling will be needed in order to fully characterise the loading mechanism from the static dot to the dynamical one. Nevertheless, we hope that these first data will allow future physicists working on the subject to get a grasp of the phenomenon.

Conclusion

In this chapter, we have demonstrated a new tool for the manipulation of a single electron. Namely, the on-demand transport of a previously selected electron thanks to a surface acoustic wave. This transport is shown to be triggered at the nanosecond and previous studies of the transport mechanism show that the electron travels at a speed around $3000\,\mathrm{m\,s^{-1}}$, which sets the overall process under the usually measured coherence times. Finally, I would like to mention an article by McNeil and co-authors [67], published at the same time, in which a similar system is studied. In this paper, the authors were able to send a single electron back and forth through a one-dimensional channel, up to 60 times, which represents a "macroscopic" distance of 0.25 mm. These figures confirm the fact that the transfer can be made with high efficiency, with a low probability of losing the electron.

An empirical model is developed and allows to capture part of the physics. However, it could not consistently explain all the data and some more modelling is needed. An important point that can be extracted from both the data and this model is that the limited bandwidth of the IDT is an issue for future developments. It will have to be improved. This can be achieved in different ways. First, fabricating IDT with split fingers is known to significantly augment the bandpass, as in [67]. Using aluminium instead of gold should have the same effect since the mass difference will limit the acoustic reflections on the fingers of the IDT. Burying the fingers should have the same effect, since the extra mass due to the finger is compensated by the mass of material that is taken away from the wafer. Another but more complicated option is to reduce the number of fingers and bend them so the SAW beam is made to converge [59]. This development has been started during my Ph.D. but not yet tested in an acoustoelectric transport experiment.

Chapter 5

Two-electron transport

Résumé

Ce chapitre rend compte d'une étude du transport lorsque la boîte d'injection est chargée avec deux électrons. Nous étudions alors les états singulet et triplets de la boîte quantique. Dans cette optique, deux principes de mesure de l'état de spin (singulet ou triplet) de deux électrons sont présentés : la première est basée sur une différence de temps charactéristique pour la sortie par effet tunnel d'un électron (le potentiel électrochimique de la boîte étant défini supérieur au niveau de Fermi, voir figure 5.3 pour le principe et figure 5.4 pour les traces attendues), la seconde met à profit l'écart énergétique entre singulet et triplet pour placer seulement ce dernier au dessus du niveau de Fermi (la boîte passera alors par un état à un seul électron si elle est dans un état triplet, voir figure 5.6 pour le principe, 5.8 pour les traces attendues et 5.9 pour des traces expérimentales). Dans les deux cas, l'état de spin dans lequel se *trouvait* la boîte est déterminé par une conversion spin-charge couplée à une mesure de la charge de la boîte. La première méthode présente l'intérêt de pouvoir fonctionner à toute température électronique, point sur lequel la seconde présente une limitation ; cependant, cette dernière permet généralement d'atteindre des efficacités de détection plus élevées. Cette dernière méthode a été implémentée et le temps de relaxation des états triplets vers l'état singulet mesuré autour de $T_1 = 4\,\mathrm{ms}$ pour une boîte fixe (figure 5.11). Ce même temps de relaxation a également été mesuré en intercalant des séquences de transfert de deux électrons entre les répétitions de la mesure de T_1. Un temps similaire, $T_1 = 5\,\mathrm{ms}$ a été mesuré (figure 5.12). La séquence de mouvements de grilles et les SAWs imposées à l'échantillon pour réaliser le transfert n'est donc pas complètement délétère pour le temps de relaxation des états triplets. Il n'a cependant pas été possible de mesurer l'état de spin de deux électrons après les avoir transférés :

le déplacement des charges transférées dans la boîte vers la configuration de mesure du spin s'avère délicate et il ne nous a pas été possible de le réaliser à ce jour sans perdre d'électron en chemin.

Un autre intérêt à l'étude du cas à deux électrons réside en la possibilité de séparer les deux électrons (figure 5.1, courbe N_{2101}) avec un taux de réussite de l'ordre de 95 % sur une large gamme de paramètres. La faculté de séparer les deux électrons repose fortement sur l'énergie de charge de la boîte quantique d'injection : une fois un électron retiré de celle-ci, l'énergie du système chute de plusieurs meV et le second en est plus difficile à extraire. La séparation de deux électrons devrait permettre de tester les inégalités de Bell.

Dans une dernière partie, nous décrivons une expérience visant à étudier la relaxation d'un spin électronique unique lors de son transfert, tout en utilisant la mesure du spin d'un système à deux électrons. L'idée est de préparer deux électrons en singulet ou triplet, de transférer un des deux électrons, d'attendre que la paire séparée décohère ($T_2^* \approx 10\,\mathrm{ns}$) et de transférer le second. La variation de probabilité d'obtenir un singulet ou un triplet en fonction de l'état de départ devraient permettre d'induire si le spin de l'électron transféré relaxe ou non pendant le transfert. Il est noté que la même expérience avec un temps d'attente entre les deux transferts plus court que T_2^* devrait permettre de démontrer le fait que le transfert conserve la cohérence du système. Cependant, il ne nous a pas été possible à ce jour de synchroniser l'envoi des deux électrons à cette vitesse.

Introduction

In this chapter, we will discuss the current achievement regarding the transport of two electrons. Building on what has been shown till now, a very tempting goal is to work with two electrons loaded in the injection dot. Studying the spin state of two electrons, singlet or triplet, should allow to lift some technical limitations we have for measuring a single electron spin, as discussed in chapter 1. A second major interest lies in the ability to send only one of the electrons, which should allow the generation of entangled pairs of particles. We will see that a major step towards this goal has been demonstrated during my Ph.D.

First, we will describe the separation of two electrons. We will then discuss the measurement of the relaxation of triplet states. In a third part, we propose an experiment that should allow to measure either the decay of a single electron spin when transferred or the decoherence of the two-spin state when the electrons are transferred one after the other.

5.1 Electrons separation ...

In order to prepare a pair of distant entangled electrons, we have to load the injection dot with two electrons, wait some time for the system to decay into a singlet state ($|\uparrow, \text{inj}; \downarrow, \text{inj}\rangle - |\downarrow, \text{inj}; \uparrow, \text{inj}\rangle$), where "inj" indicates the fact that the electron is in the injection dot, and then send one of the electrons to the other side of the sample. Assuming that the passage from the situation where the two electrons are in the same dot to a situation where they are separated is non-adiabatic, the output is expected to be: $|\uparrow, \text{inj}; \downarrow, \text{rec}\rangle - |\downarrow, \text{inj}; \uparrow, \text{rec}\rangle$, where we arbitrarily chose the electron that travelled. This state is fully entangled. The adiabaticity condition compares the time it takes for the electrons to become separated to the time it takes to mix a singlet and a triplet state. This mixing is induced by the hyperfine field. If the separation is too slow, then the electrons will adiabatically follow the ground state and end up in a product state where each electron is in the ground state of the local magnetic field—determined by the external field and the local nuclear field [31]. The relevant time-scale for the separation is expected to be a fraction of the SAW period, $T_{\text{SAW}} \simeq 380\,\text{ps}$. The hyperfine field is typically up to 5 mT, that is 25 MHz or 40 ns. These two time-scales ensure that the separation should always conserve the spin state of the electronic system.

A first step towards the preparation of this entangled state is to be able to send on demand only one of the two electrons loaded in the injection dot. The idea behind the separation relies on the observation made earlier about the nanosecond triggering: a change in the polarisation point V_c during the SAW burst allows to more or less strongly prevent an electron from leaving

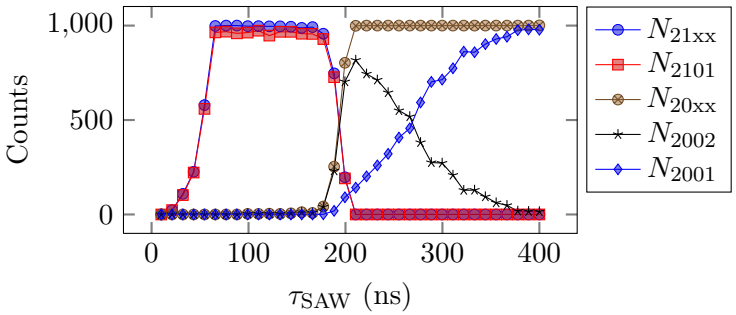

Figure 5.1: Transfer counts for a two-electron dot *vs.* the SAW burst duration for 1001 repetitions. $N_{\alpha\beta\gamma\delta}$ is the number of times the injection (reception) dot was prepared with α (γ) electrons and ended up with β (δ) electrons.

the dot. In addition, the chemical potential of the system changes by more than 2 meV when an electron is added or taken off. In other words, when extracting one electron from a two-electron dot, the system gets much lower in energy and the remaining electron should be more difficult to extract. Figure 5.1 shows the number of transfers of one electron (N_{2101}) and two electrons (N_{2002}) when loading the injection dot with two electrons. The number of times the two electrons are separated corresponds to N_{2101}. The time of SAW irradiation τ_{SAW} is varied from almost 0 ns to 400 ns. We can see that for "short" SAW irradiation, only one electron out of the two is extracted from the dot and transferred with high efficiency—case N_{2101}, around 95 %—on a wide interval of time τ_{SAW}. For $\tau_{\mathrm{SAW}} = 210$ ns, we get a transfer rate for the two electrons of 80 %. When the SAW irradiation exceeds 180 ns, the number of times both electrons get extracted from the dot ($N_{20\mathrm{xx}}$) rises. At the same time, the number of transfers of two electrons (N_{2002}) goes up as well. However, for more than 210 ns SAW irradiation, N_{2002} starts decreasing while N_{2001} keeps increasing and $N_{20\mathrm{xx}}$ stays constant. This indicates that for longer τ_{SAW} the two electrons get caught in the reception dot (after 210 ns of irradiation) and one of them is subsequently expelled from the reception dot. The fact that $N_{21\mathrm{xx}}$ and $N_{20\mathrm{xx}}$ have a finite rise time (a few tens of nanoseconds) as a function of τ_{SAW} can originate either from a slow rise of the SAW amplitude, from the fact that electrons get excited on higher orbitals (from which they would be easier to extract), or from phonon-assisted tunnelling due to the presence of the SAW [18]. The dependence of the transfer counts as a function of the RF power, shown in figure 5.2, shows the same behaviour.

It is now clear that an electron can be more or less protected from the SAW influence. Using this information, we can now understand the change in operating point for the separation of two electrons or the transport of

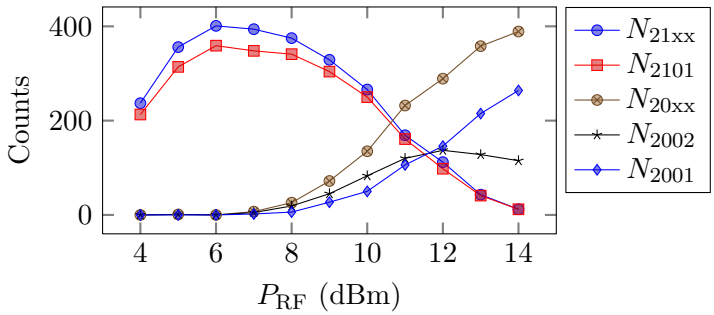

Figure 5.2: Transfer counts for a two-electron dot *vs.* the SAW power, for 401 repetitions. $N_{\alpha\beta\gamma\delta}$ is defined in caption of figure 5.1.

two electrons. In both cases, the metastable point for the injection dot will usually necessitate less-negative gate voltages to avoid one of the electrons spontaneously falling back into the reservoir. On the reception side, catching one electron is equivalent to the description of the preceding chapter. However, in order to catch two electrons, the reception dot needs to be polarised with gates p' and c' more positive while the gate b' has to be made more negative; the goal is to prevent one electron from being re-expelled from the reception dot. The limit is that the chemical potential of the dot may move below the Fermi level. As a consequence the probability that an electron will spontaneously enter the reception dot is increased. In the end, we know in which directions to change the different gate voltages in order to obtain a given behaviour (injection of 1 or 2 electrons).

5.2 Singlet-triplet relaxation

As discussed in chapter 1, a single electron spin could not yet be measured in our setup. The main reason was a too high electronic temperature: a high magnetic field is needed in order to get a Zeeman splitting larger than the temperature-induced broadening of the Fermi level. The limitation comes from the fact that the relaxation time for a single spin scales as B^{-5}: at 1 T, $T_1 \simeq 5$ ms [27] and at 7 T, $T_1 \simeq 0.8$ ms [26], and we need to be able to measure much faster than 1 kHz. However, an alternative scheme has been presented by Hanson and co-authors [68] in order to overcome high electronic temperatures without demanding unrealistic magnetic fields. These schemes allow to measure the singlet or triplet spin state of a pair of electrons. The first one consists in pushing both singlet and triplet states well above the Fermi level of the reservoir. The full writing of the

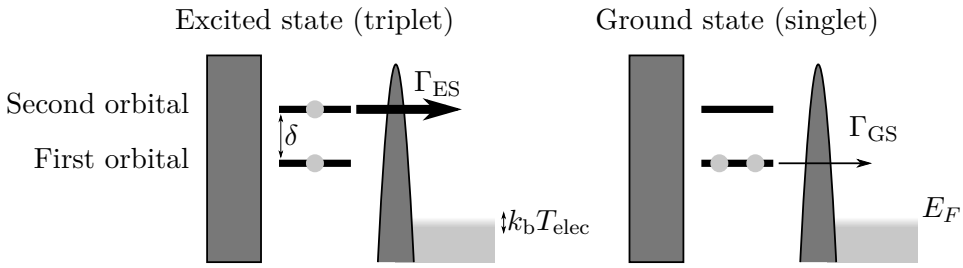

Figure 5.3: The levels represented are the single-particle orbitals of the trap. The excited orbital, populated for a triplet but not for a singlet, offers a faster tunnelling time towards the reservoir.

singlet and triplet states is:

$$\text{Singlet}: \quad |gg\rangle \otimes (|\uparrow\downarrow\rangle - |\downarrow\uparrow\rangle) \tag{5.1}$$

$$\text{Triplet}: \quad (|ge\rangle - |eg\rangle) \otimes |\uparrow\uparrow\rangle \tag{5.2}$$

$$(|ge\rangle - |eg\rangle) \otimes (|\uparrow\downarrow\rangle + |\downarrow\uparrow\rangle) \tag{5.3}$$

$$(|ge\rangle - |eg\rangle) \otimes |\downarrow\downarrow\rangle, \tag{5.4}$$

where g and e stand for the first and second single-particle orbitals of the trap. The triplet group differs from the singlet in that it occupies the first excited orbital of the trap, that is typically up to a few meV higher in energy (we measured 400 µeV of orbital splitting for the sample used in this work). Since this orbital is higher in energy, both the tunnelling barrier height and width are lowered compared to the singlet state, as schematically depicted in figure 5.3. In addition, if we model the trapping potential with a 1D harmonic trap along the direction from the dot to the reservoir, the wave function for the first and second eigenstates are respectively a Gaussian of the position x and the same Gaussian multiplied by x (we take $x = 0$ at the centre of the dot). The latter is expected to have a larger overlap with states outside the dot. As a result, a dot filled with two electrons polarised in the situation depicted in figure 5.3 will decay towards the singly-occupied state faster if the electrons are in the triplet state. We now assume that the tunnel rate for the excited state is much larger than that for the ground state. The charge state of the dot is measured after a time τ, such that $\tau_{\text{triplet}} \ll \tau \ll \tau_{\text{singlet}}$, and where $\tau_{\text{triplet(singlet)}}$ is the characteristic time for the tunnel event if the electrons were in a triplet (resp. singlet) state. This charge state allows to infer the spin state—singlet or triplet—in which the electrons *were*. Schematic QPC time traces for both cases are presented in figure 5.4. This principle allowed the authors of [68] to reach 80 % visibility for the read-out. Regarding the temperature dependence, the relevant energy scale to be compared to the temperature is the chemical potential of the dot and not the Zeeman splitting. The former can be made

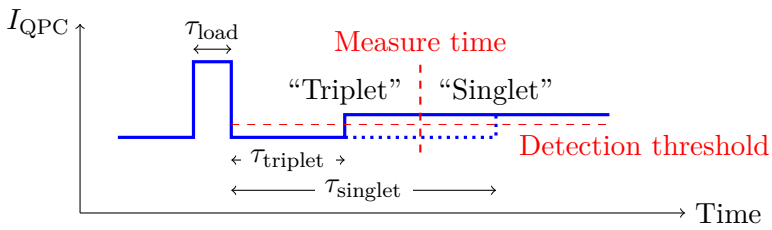

Figure 5.4: Schematic time traces for the tunnel-rate read-out. If the QPC conductance gets back up before a given measure time (solid line), the state is declared a triplet, else it is considered a singlet (dotted line). The loading event is not shown since it is usually much faster than the detection bandwidth of the setup, hence unresolved experimentally. The higher current below τ_{load} is due to the cross-talk to the gate voltage change.

as large as needed to overcome an elevated electron temperature by pushing the gates more negative, as long as the slower tunnelling time is kept much longer than the detection bandwidth. However, this read-out scheme will require the tunnelling rate for the excited state to be much larger than for the ground state and will not allow for an easy sight of spin signature otherwise, since the tunnelling traces will only get a bit longer but keep the same shape. We now turn to the estimation of the experimental tunnelling rates for the sample studied. The tunnelling rates for singlet and triplet can be estimated as follows: the dot is loaded with a single electron, then pushed in the $N = 2$ region for a time τ_{load} to load a second electron and back again in the $N = 1$ region. The average time traces for the decay of the dot towards one electron allows to extract the barrier time. By varying τ_{load}, the proportion of singlet will vary: since there are 3 triplet states and $\tau_{\mathrm{triplet}} < \tau_{\mathrm{singlet}}$, the dot has more chances to get loaded in the triplet state; a wait time in this state will then let the system decay to the singlet state. The figure 5.5 presents the average time traces for 100 µs and 25 ms load times. These two times satisfy $100\,\mu\mathrm{s} \ll T_1 \ll 25\,\mathrm{ms}$, as will be shown further, which ensures that the latter case prepares only singlets, whereas the first case prepares a mixture of singlet or triplet. The 25 ms case is hence fitted with a single exponential decay, with a time constant of 680 µs. The 100 µs case is fitted either with a single exponential decay or with the sum of two exponentials, which allows to take into account a non-negligible probability of preparing a singlet state; in the latter case, we fix $\tau_{\mathrm{singlet}} = 680\,\mu\mathrm{s}$, as previously determined. The fits, shown in figure 5.5, could however not allow to discriminate clearly between the two situations. We extract decay times of respectively 320 µs for the single decay and 211 µs for the sum of two decays. These values lead to a rate $\tau_{\mathrm{singlet}}/\tau_{\mathrm{triplet}}$ ranging from 2 to 3. In both cases, this rate is too low for the tunnel-rate read-out to be highly efficient: the expected visibility can

be determined more accurately to be 40 % by following reference [68] (the derivation takes into account the relaxation time T_1; we used $T_1 = 5\,\mathrm{ms}$, determined later in this section). Assuming the rate $\tau_{\mathrm{singlet}}/\tau_{\mathrm{triplet}}$ to be the same at the load point, the probability to load the dot in a triplet state can reach

$$P_{\mathrm{T,max}} = \frac{3\Gamma_{\mathrm{triplet}}}{\Gamma_{\mathrm{singlet}} + 3\Gamma_{\mathrm{triplet}}} \approx 90\,\%, \tag{5.5}$$

where $\Gamma = 1/\tau$ and the factor of 3 accounts for the existence of 3 triplet states. This is the higher bound for a load time infinitely shorter than T_1. Note that the factors of 3 present in equation (5.5) ensure that a triplet state can be prepared with 75 % probability, even in the case $\tau_{\mathrm{singlet}} = \tau_{\mathrm{triplet}}$.

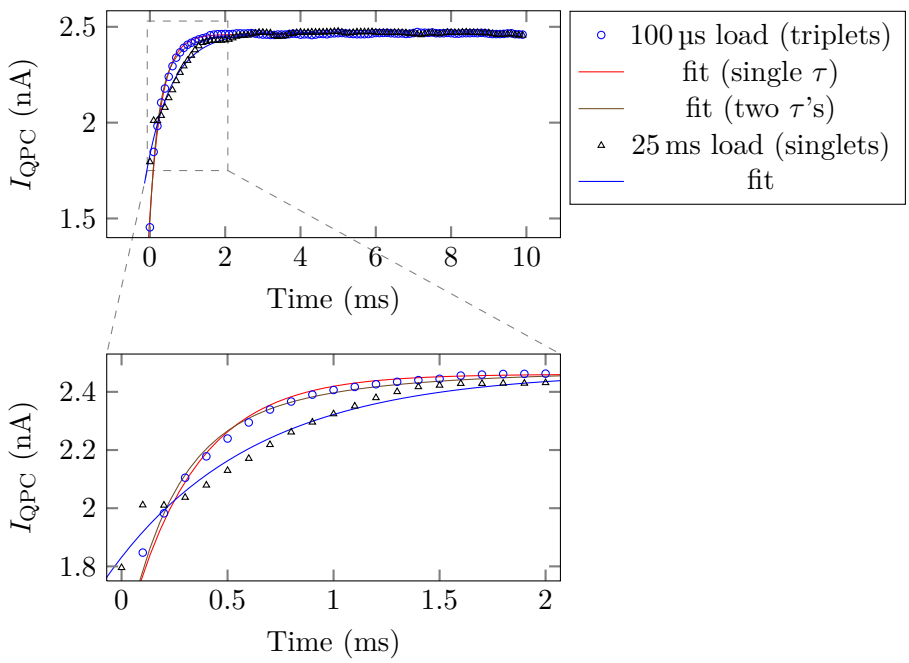

Figure 5.5: Extraction of the tunnelling times of singlet and triplets. The bottom graph is a close-up of the region defined by the dashed rectangle. The fits are detailed in the text. The curves are averaged over 50 time traces, extracted from figure 5.10, for $\delta V_{\mathrm{b,push}}$ from 20 mV to 22 mV.

Another scheme for singlet-triplet read-out was proposed by Meunier and co-workers [69]. It mixes the energy selectivity of the energy-dependent-tunnelling scheme [26] and the tunnel-rate read-out presented in the previous paragraph. This scheme once again uses the high energy splitting present between singlet and triplet states, which makes the energy-dependent tunnelling regime reachable without magnetic field. Indeed, the single-particle splitting typically ranges from 100 µeV to a few meV for a few-electron dot (measured as 400 µeV for the dots used in this thesis). The actual energy

Sylvain Hermelin, Ph.D. Thesis

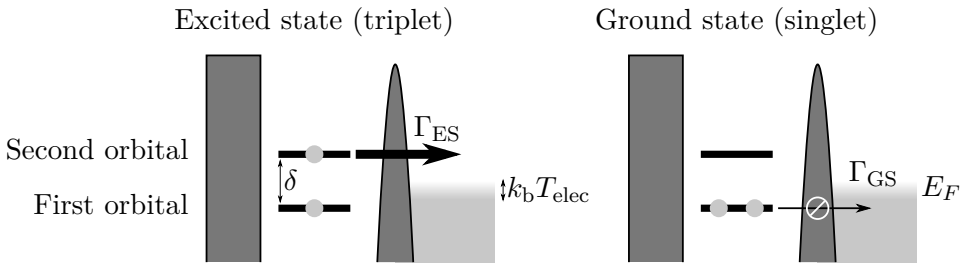

Figure 5.6: Principle of the singlet-triplet measurement scheme proposed in [69]. The use of the large single-particle splitting allows to overcome the large electronic temperature. The slow reload of the dot allows to monitor the unloading event with a low-bandwidth setup.

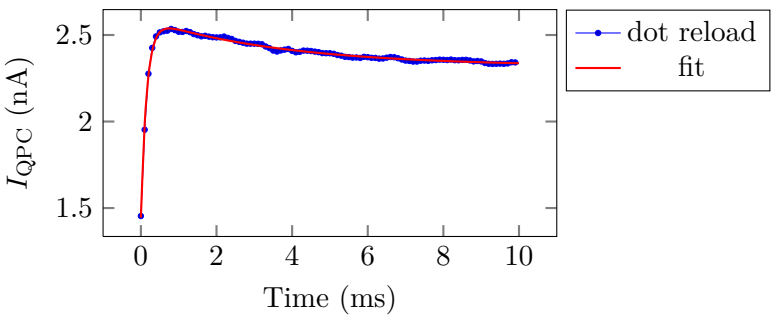

Figure 5.7: Averaged time traces of a singlet-triplet measurement in energy-selective tunnel-rate read-out. The load time is 100 µs. The fit is a sum of two exponentials (plus a constant background) with characteristic times 160 µs (due to the rise time of the amplification chain) and 3.7 ms for the dot reload time into a singlet state.

difference between the singlet and triplet state is $\delta - E_{\text{exch}} \simeq \delta/2$, where δ is the single-particle splitting and E_{exch} the exchange energy. This should allow energy-dependent tunnelling for electronic temperatures up to a few hundreds of mK, as illustrated in figure 5.6. For comparison, a Zeeman splitting of 100 µeV requires a magnetic field much larger than 4 T in GaAs.

Figure 5.7 shows 60 averaged time traces of a singlet-triplet measurement. We can extract two characteristic times from this curve: the exit time, which is faster than 160 µs (we remind that our measuring setup has a rise time of 150 µs) and the reload time (into a singlet state) which is 3.7 ms. These values seem to disagree with the factor of 3 for the tunnelling rates from excited and ground excited states determined earlier, since it now is above 20. It is to be noted however, that one is for tunnelling out of the dot and one into the quantum dot (even if these would be expected to be symmetric). Nevertheless, it is consistent with a work from Amasha and co-workers

[70] in which the authors showed that the ratio between tunnelling into the ground or excited spin states of an empty dot can vary significantly with the shape of the dot and the magnetic field. The authors note that no theoretical description of the tunnelling allows to explain their data. Anyhow, this increase allows to get a higher read-out visibility since the dot in a triplet state can be made to decay into a single-electron dot faster than T_1 and the reload time can be made long enough for the lower charge of the dot to be monitored. Using this scheme, high efficiencies, up to 97 % have been demonstrated [69]. This scheme presents a limitation compared to the tunnel-rate read-out since we need the condition $\delta \gg kT_{\text{elec}}$ in order to work. However it presents the advantage of allowing a larger visibility and makes it easier to detect the signature of spin relaxation. The expected shape for the QPC time traces are shown in figure 5.8. In figure 5.9 we show an example of experimental traces for a singlet event and a triplet event. By comparing these with traces for the tunnel-rate read-out (figure 5.4), we can see that the traces change significantly depending on the spin state of the system. This fact will make it much easier to spot a signature of spin in the system.

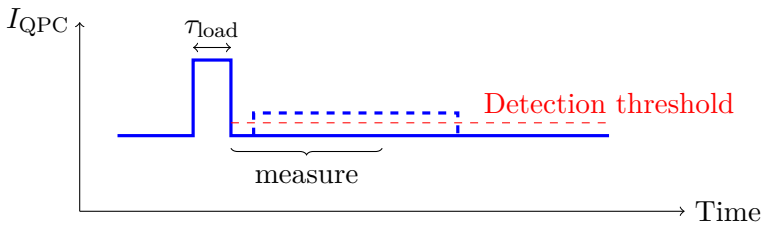

Figure 5.8: Expected time traces for singlet-triplet readout. The loading event—under τ_{load}—is not resolved with our setup. After pushing the states around the Fermi energy, a singlet state is unperturbed (solid line) while a triplet state (dashed blue line) will lose one electron. This fast tunnel event may be unresolved with our setup (the curve starts on the higher current state). The reload of the dot has to form a singlet state, which takes a longer time.

The feasibility of the measurement scheme can be quickly demonstrated. The idea is to first push the dot into a region of one electron and wait for it to reach its stable charge. Then, we push the dot into the two-electron region of the stability diagram to load a second electron. These gate movements are driven by the voltages V_{b} and V_{p}. The movements of V_{b} change significantly the tunneling times. This ensures that the loading times are faster than the times for tunnelling out of the dot. The movements of V_{p} then allows to move the chemical potential. The dot is then pushed to some measuring position. This one can be modified by $\delta V_{\text{p,measure}}$. As has been discussed at the beginning of the section (on page 127), a triplet state is preferentially

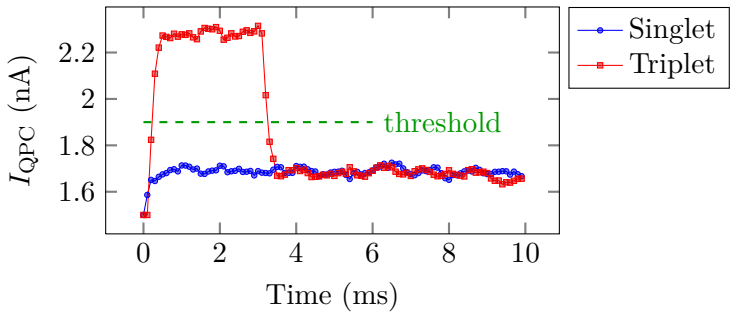

Figure 5.9: Single traces for a singlet event (blue, circles) and a triplet event (red, squares). Measurement starts after the loading time τ_{load} (see figure 5.8). In comparison with the traces shown in figure 5.8, the trace starts at a low current due to the extra movement of gate p.

loaded into the dot. Figure 5.10 shows time traces of the nearby QPC current as a function of $\delta V_{\text{p,measure}}$ for 100 µs and 25 ms load times. Note that we record the traces only after the load time is over. In figure 5.8, a time interval is designated as "measure". It starts right after the system is brought to the measurement position. If the QPC current goes higher than a given threshold during this interval, then the system is declared in a triplet state. The top panel of figure 5.10 presents measurements when the dot waits $\tau_{\text{load}} = 25$ ms at the loading point. The aim of this waiting time is to ensure that the system has had the time to decay into the singlet state before measuring it. The degeneracy 1–2 electrons is clearly seen around $\delta V_{\text{b}} = 22.5$ mV. One can see as well that the barrier is quite slow: the charge oscillations around the degeneracy show a characteristic time on the order of 5 ms to 10 ms. The exit of the second electron, for $\delta V_{\text{b,push}} \leq -22$ mV, exhibits a comparable characteristic time. These unloading traces show that the dot is actually loaded with two electrons. We now repeat the experiment but the wait time at load is shortened to $\tau_{\text{load}} = 100$ µs. The corresponding traces are reported in the lower panel of figure 5.10. The quantum dot should now be loaded most of the time with two electrons in a triplet state. Upon scanning the degeneracy from 2 electrons to 1 electron, we can see that around $\delta V_{\text{b,measure}} = 24$ mV the dot starts to lose one electron. We know from the previous scan that the dot is still well below the degeneracy point at $\delta V_{\text{b,measure}} = 24$ mV. This corresponds to the fact that when in the triplet state, a higher single-particle level is occupied and hence the quantum dot energy is augmented by the single-particle level splitting δ ($\simeq 400$ µeV) minus the exchange energy E_{exch} [71]. As a consequence, the dot reaches the Fermi level of the lead for a more positive gate voltage. The comparison of the two graphs presented in figure 5.10 gave the first traces of spin that we could measure. A comparison of the two panels of figure 5.10 shows that

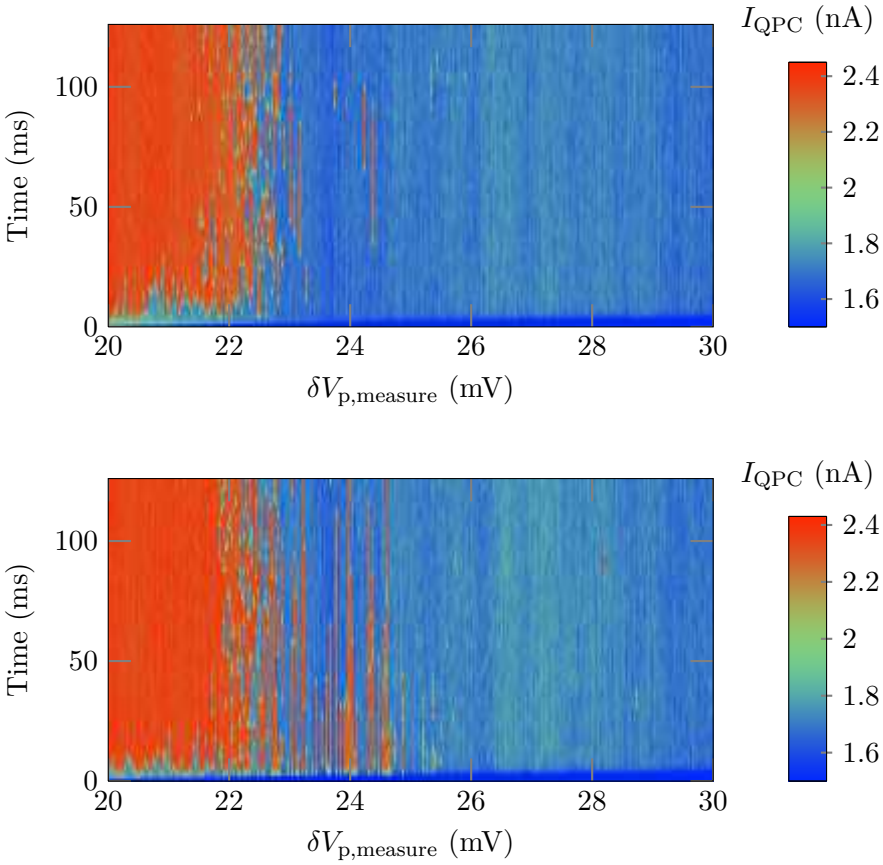

Figure 5.10: Signature of spin. The 1 to 2 electrons degeneracy is scanned after the dot has been loaded with two electrons. In the first case, we wait for 25 ms at the load point while we wait only 100 µs for the second graph. The extra lines appearing are the signature of occupied triplet states.

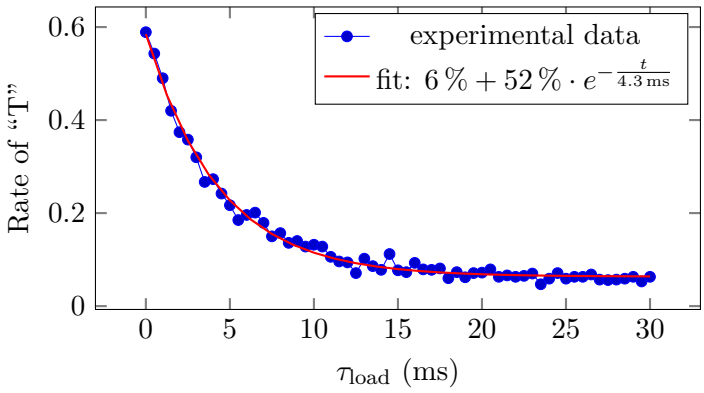

Figure 5.11: T_1 measurement. The rate of "triplet" outcome decreases exponentially with characteristic time T_1 as a function of the wait time at loading point. The determined $T_1 = 4.3\,\mathrm{ms}$.

the triplet state can be measured in an interval of around 3 mV of δV_{p}. This gives a direct estimation of the energy difference between the singlet and the triplet state in this quantum dot: $E_{\mathrm{ST}} \gtrsim 120\,\mu\mathrm{eV}$, in agreement with the literature [72, 73]. Thus, taking $\delta = 400\,\mu\mathrm{eV}$, we get the exchange energy $E_{\mathrm{exch}} \simeq 280\,\mu\mathrm{eV}$.

Finally, we determine the triplet-to-singlet relaxation time by applying the measuring scheme we developed just before: $\delta V_{\mathrm{b,measure}}$ is set around 24 mV and τ_{load} is varied from 1 µs to 30 ms. The sequence is repeated a thousand times for each loading time. The figure 5.11 presents the probability to measure the two-electron state as a triplet as a function of this waiting time. We can see a clear exponential decay of this probability, corresponding to the relaxation time for the triplet states $T_1 = 4.3\,\mathrm{ms}$. The low contrast of the exponential, 52 %, is the visibility of the measurement times the initial probability of being in a triplet state. Its low value will be an issue for future experiments: we propose a two-electron experiment in the next section in which a 33 % change in the output probability of getting a singlet is expected. It is therefore important to know why the visibility of the measurement is low. A lower bound for the visibility can be estimated from:

- the lowest probability of preparing a triplet state. The worst case should be for $\Gamma_{\mathrm{singlet}} = \Gamma_{\mathrm{triplet}}$, which yields a 75 % probability of loading a triplet (see equation (5.5) on page 130).
- counting the number of times the system is a triplet but tunnels off the dot only after the measuring window is closed. That is given by $\exp(-\Gamma_{\mathrm{triplet}} \times \tau_{\mathrm{measure}}) \approx 15\,\%$ for $\Gamma_{\mathrm{triplet}} = 210\,\mu\mathrm{s}$, determined earlier, and $\tau_{\mathrm{measure}} \approx 400\,\mu\mathrm{s}$ which corresponds to the typical value for the best visibilities.

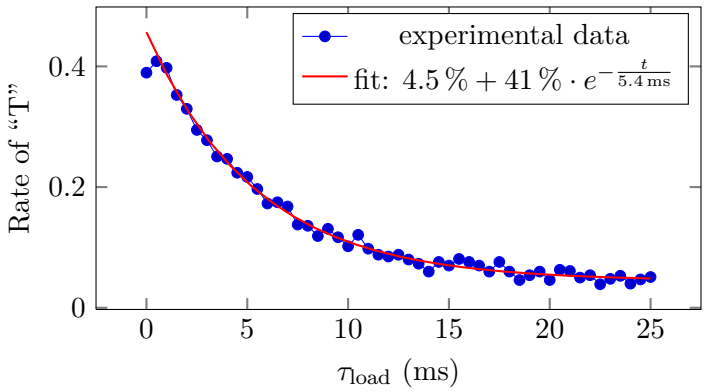

Figure 5.12: T_1 measurement with the full transfer sequence running. Note that the electrons whose spin is measured are *not* transferred, but prepared in the reception dot. The determined T_1 is around 5 ms. The first point has not been taken into account for the fit.

- the number of triplets missed because the dot reloads one electron faster than we can measure: the current peak is shorter in time than the rise time of the amplification chain. This can be estimated by $\exp(-\text{risetime} \times \Gamma_{\text{reload}}) \approx 95\,\%$, where we take a rise time of 150 µs and $\Gamma_{\text{reload}} = 1/3.7\,\text{ms}$ as discussed previously. We remind that the dot reloads in a singlet state.
- the number of triplets that decay before they could tunnel out should be negligible since $\exp(-\Gamma_{\text{triplet}} T_1) < 10^{-6}$.

These parameters give an estimate of 60 % for the visibility, which is still higher but in reasonable agreement with the 52 % visibility measured.

We now need to check if T_1 is reduced due to the transfer sequence. The figure 5.12 shows the same measurement when the spin measurement is taken between realisations of the full experimental sequence that transfers two electrons through the sample—but re-preparing each time the reception dot for the spin measurement—including the SAW burst and nanosecond gate-voltage pulses. We can see that a similar T_1 time and similar contrasts were obtained. As a consequence, we know that the spin-measurement technique used is not severely hindered by all the gate movements and the recurring SAW bursts. This result strongly supports this way of research.

However, the actual experiment that consists in sending simultaneously the two electrons and checking their final spin state could not yet be realised. We indeed discussed in the previous section the fact that we cannot trigger simultaneously the transfer of the two electrons. Nevertheless, we describe in what follows, experiments that should allow to get around this limitation.

5.3 . . . and recombination

We have seen that the two electrons could be efficiently separated into the distant dots. We have seen as well that it is possible to sequentially transfer the two electrons. In this section, we will question what happens to their spin when we first separate the two electrons and then bring them back together.

5.3.1 Theory

Let's consider the injection dot loaded with two electrons in a singlet state:

$$\text{Singlet}: \ |\uparrow\downarrow\rangle - |\downarrow\uparrow\rangle, \tag{5.6}$$

where the $\sqrt{2}$ factor is dropped for simplicity. We assume that the separation is non-adiabatic, as discussed in section 5.1. Then, once the first electron is sent, the system ends up in the state:

$$|\uparrow, \text{inj}; \downarrow, \text{rec}\rangle - |\downarrow, \text{inj}; \uparrow \text{rec}\rangle, \tag{5.7}$$

where inj and rec designate the injection and reception dot respectively. The possibility that the transported electron ends up in another orbital state than the ground state is discarded since the short charge-coherence time should get it to decay into the ground state fast compared to the experimental timings we can attain so far with our setup.

In this waiting state, the electron spin states will start to mix, due to the difference in the nuclear magnetic field in the two separated dots. Hence, the spin state of the two electrons will end up in a statistical state after a few tens of nanoseconds. The probability for two electrons prepared in a singlet state to still be in a singlet state after a separated evolution time t will then drop to $\frac{1}{3}$ following the formula [29]:

$$P_{\text{s}}(t) = \frac{1}{4} + \frac{1}{12}\left\{1 + 2e^{-\frac{1}{2}\left(\frac{t}{T_2^*}\right)^2}\left(1 - 2\left(\frac{t}{T_2^*}\right)^2\right)^2\right\}^2, \tag{5.8}$$

when there is no external magnetic field. In the case with a magnetic field $B \gg B_{\text{nuc}}$ (B_{nuc} is the typical nuclear field amplitude), the singlet probability becomes:

$$P_{\text{s}}(t) = \frac{1}{2}\left(1 + e^{-\left(\frac{t}{T_2^*}\right)^2}\right), \tag{5.9}$$

and drops to $\frac{1}{2}$ after a long separation time. The dephasing time T_2^* is typically on the order of a few tens of nanoseconds for static dots. Since the time the electrons spend in movement is only of order 1 ns, we expect T_2^* to

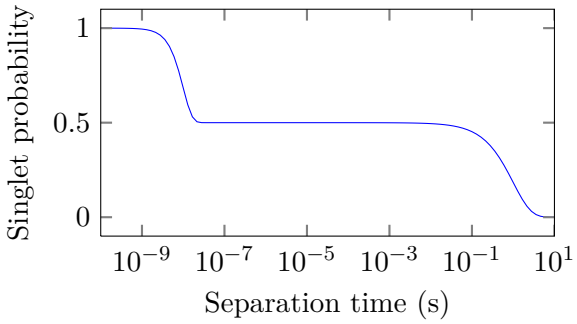

Figure 5.13: Probability to find the system in a singlet state as a function of the separation time. Plot for $T_2^* = 10\,\text{ns}$ and $T_1 = 1\,\text{s}$.

stay of the same order. In the following, we will only consider the case with an external magnetic field.

Once separated for a time longer than T_2^*, we can consider the two spins as independent. Starting from a singlet $|\uparrow\downarrow\rangle - |\downarrow\uparrow\rangle$ the system ends up, for example, in the state $|\uparrow\downarrow\rangle$, while the ground state is $|\uparrow\uparrow\rangle$ since a magnetic field is applied. The single spins will decay with the characteristic time T_1 (for a single electron spin), which, for a parallel magnetic-field configuration, varies from 1 ms at 6 T to 1 s at 1 T [27]. The probability for the system to be in a singlet state will then further drop to 0 when the separated spins will decay. A summary of the probability to find the system in a singlet state as a function of the separation time is shown in figure 5.13. From this graph, we can see two regions were the singlet probability evolves significantly as a function of the separation time: around $T_2^* = 10\,\text{ns}$ and around $T_1 = 1\,\text{s}$. This evolution allows to plan two experiments that we will now describe by order of technical difficulty.

The first experiment consists in preparing a singlet in the injection dot, send one of the two electrons and wait for a time τ_{sep} from 10 ms to 10 s in a 1 T field before sending the second electron. Once the two electrons are recombined, their spin state has to be measured. The expected variation for the rate of singlet output is the one given in the right part of figure 5.13. The expected visibility of the decay is 50 %. The observation of a decay for the singlet probability when the separation time gets longer would prove that the transfer does not induce a relaxation of a single spin during its transfer.

The second experiment is basically the same as the preceding, but the separation time is now on the order of $T_2^* = 10\,\text{ns}$. The decay for the singlet probability should now follow the left part of figure 5.13. The expected visibility for the decay is 50 %. Its observation would prove that the transfer is coherent and allows to preserve the entanglement between the two spins.

Another experiment to check if a single spin is subject to relaxation during the transfer can be designed. In this experiment, the separation time is kept fixed (longer than T_2^* but shorter than T_1) and the initial probability to be in a singlet state is varied. This is achieved by loading a triplet that is allowed to relax for a varying time τ_{load}. The figure 5.14 presents an estimate

initial state probability	Initial state	separated state	final state	final state probability
$P = 1$	$\lvert\uparrow\downarrow\rangle - \lvert\downarrow\uparrow\rangle$	$\xrightarrow{\frac{1}{2}}$ $\lvert\uparrow\downarrow\rangle$	$\xrightarrow{\frac{1}{2}}$ $\lvert\uparrow\downarrow\rangle - \lvert\downarrow\uparrow\rangle$	$P = \frac{1}{4}$
			$\xrightarrow{\frac{1}{2}}$ $\lvert\uparrow\downarrow\rangle + \lvert\downarrow\uparrow\rangle$	$P = \frac{1}{4}$
		$\xrightarrow{\frac{1}{2}}$ $\lvert\downarrow\uparrow\rangle$	$\xrightarrow{\frac{1}{2}}$ $\lvert\uparrow\downarrow\rangle - \lvert\downarrow\uparrow\rangle$	$P = \frac{1}{4}$
			$\xrightarrow{\frac{1}{2}}$ $\lvert\uparrow\downarrow\rangle + \lvert\downarrow\uparrow\rangle$	$P = \frac{1}{4}$
$P = \frac{1}{3}$	$\lvert\uparrow\uparrow\rangle$	$\xrightarrow{1}$ $\lvert\uparrow\uparrow\rangle$	$\xrightarrow{1}$ $\lvert\uparrow\uparrow\rangle$	$P = \frac{1}{3}$
$P = \frac{1}{3}$	$\lvert\uparrow\downarrow\rangle + \lvert\downarrow\uparrow\rangle$	$\xrightarrow{\frac{1}{2}}$ $\lvert\uparrow\downarrow\rangle$	$\xrightarrow{\frac{1}{2}}$ $\lvert\uparrow\downarrow\rangle - \lvert\downarrow\uparrow\rangle$	$P = \frac{1}{12}$
			$\xrightarrow{\frac{1}{2}}$ $\lvert\uparrow\downarrow\rangle + \lvert\downarrow\uparrow\rangle$	$P = \frac{1}{12}$
		$\xrightarrow{\frac{1}{2}}$ $\lvert\downarrow\uparrow\rangle$	$\xrightarrow{\frac{1}{2}}$ $\lvert\uparrow\downarrow\rangle - \lvert\downarrow\uparrow\rangle$	$P = \frac{1}{12}$
			$\xrightarrow{\frac{1}{2}}$ $\lvert\uparrow\downarrow\rangle + \lvert\downarrow\uparrow\rangle$	$P = \frac{1}{12}$
$P = \frac{1}{3}$	$\lvert\downarrow\downarrow\rangle$	$\xrightarrow{1}$ $\lvert\downarrow\downarrow\rangle$	$\xrightarrow{1}$ $\lvert\downarrow\downarrow\rangle$	$P = \frac{1}{3}$

Figure 5.14: Statistics of the recombined spin state if the two spins stay separated for a time long compared with T_2^*. The upper panel is for an initial singlet and the lower panel for an initial triplet state. The latter is supposed to be in any of the three triplet states with equal probability. Writing $\lvert\uparrow\downarrow\rangle$ for the separated case means that the electron left in the injection dot is in state $\lvert\uparrow\rangle$ and the one transferred in state $\lvert\downarrow\rangle$.

of the singlet or triplet outcome probabilities as a function of the input state. We can see that for an input in a singlet state, the probability to get a singlet in the output is 50 %, in accordance with equation (5.9). The triplet input state should lead to 17 % of singlet outcomes. Since upon scanning the load time τ_{load} around T_1 the input probability for a singlet state should

increase exponentially, the probability to have a singlet as an output state should increase exponentially as a function of τ_{load}. The expected visibility for this measurement is 33 %. This experiment would hence need a larger measurement contrast.

We will now discuss technical aspects regarding the implementation of such experiments.

5.3.2 Technical limitations

As has been discussed in the previous section, the coherence of the transfers could be tested by sending the two electrons separated by a time varying from a few nanoseconds to a few tens of nanoseconds. It is then required to trigger the two consecutive transfers on a time-scale of 1 ns.

The current status of the experiment is that the two transfers can be realised within a few tens of nanoseconds from each other, but only one (the second one) is triggered on the nanosecond time-scale. The first transfer happens within a 40 ns window. This limitation comes from the arbitrary waveform generator we use: the system has to be well protected for the first transfer to be triggered within 1 ns, but then the pulse amplitude needed to trigger the second transfer is higher than what can be achieved with our generator (see the discussion in section 5.1).

The constraints on the triggering hence need to be relaxed. We can then turn to the experiment on relaxation. This one indeed requires to trigger the two transfer events faster than approximately 10 ms. We can achieve this by using the microsecond-DACs to get bigger gate-voltage movements. However, in comparison with the previous measurement, the gate movements are made *much* larger and we did not succeed yet to keep the spin information during these configuration changes. A first limitation has been identified as the difficulty to bring back the two electrons from the catching position to the spin measuring position. We could indeed monitor that the system tends to lose one electron into the reservoir and subsequently reload with another one when getting close from the measurement configuration. This configuration change will have to be extremely fine-tuned in order for this experiment to work properly.

Another limitation will be linked to the visibility of the measurement: the expected variation of singlet probability varies from 33 % to 50 % depending on the experiment. If we take into account the 50 % visibility of the measurement shown in the previous section, the expected signal drops to the interval 16.6 %–25 %. In order to get a statistical error 10 times smaller than the signal, at least on the order of 4000 repetitions are needed for each $\tau_{\text{separation}}$ point, and at least 10 values of $\tau_{\text{separation}}$ should be measured. These values are not unreasonable, but it is quite likely that a switch in the sample will occur during such long measurement sequences.

Conclusion

In this chapter we discussed the possibility to selectively send one or two electrons out of a pair. It opens the way to the generation of distant spin-entangled electrons, but the entanglement still has to be proven. Towards this goal, a first milestone will be to measure the correlations between the two separated spins. For this it will be necessary to be able to measure a single electron spin. This will require to improve the SAW generation in order to minimise heating of the reservoirs, to increase the measurement bandwidth in order to be able to work at higher magnetic fields, which lowers the relaxation time T_1. Preliminary experiments on the triplet-to-singlet relaxation allowed to check that the intercalation of transfer sequences between spin-measurement sequences does not prevent us from measuring spin.

We described three experiments that should allow us to measure either the relaxation of a single spin during its transfer (separate transfers with long wait times in between), or its coherence (separate transfers with nanosecond delays). The two experiments that should allow to test the relaxation should be realisable in the current experimental conditions. The first tests that we realised allowed us to identify the movement from the reception position to the spin-measurement configuration as a key point that has to be addressed.

Conclusion and perspectives

The aim of my Ph.D. was to explore the feasibility of transporting a qubit coded on the spin state of a single electron in order to entangle distant qubits. During this project, we demonstrated that a single electron can be transferred on demand from one quantum dot to another distant quantum dot. This achievement is part of the global effort to realise a scalable quantum computer: single-qubit rotations have been demonstrated in lateral GaAs quantum dots, as well as two-qubit entanglement in juxtaposed dots.

For this purpose, several experimental building blocks had to be set up or developed, and put together. They include a cryogenic system, low-noise electronics, RF electronics and software to control the experiments. The sample used to demonstrate the single-electron transfer is constituted of: two quantum dots placed 3 µm apart, quantum point contacts for charge detection in each dot, a one-dimensional channel for guiding the electron and to prevent it from mixing with other electrons and an interdigitated transducer to generate the surface acoustic waves. Each of the dots is placed in the single-electron regime. We explored and demonstrated the possibility to isolate one electron from the reservoir and bring it higher in energy than the Fermi level. Such metastable states are shown to live up to time scales of the order of 1 s. Using a metastable state, the electron is brought close to the one-dimensional channel that links the two dots and it is demonstrated that a surface acoustic wave propagating along the sample can transfer this electron into the other dot. The efficiency of the transfer is as high as 90 % and suggests that the system can be used to study in more detail the propagation of electrons dragged along one-dimensional channels by surface acoustic waves. Towards the goal of transporting an electron spin qubit, we realised preliminary experiments to measure the spin state of electrons. First, the relaxation time of a two-electron dot prepared in a triplet state has been measured to be around 5 ms. It is shown that this time is not reduced when the transfer sequence of one or two electrons is intercalated in between the repetitions for the spin measurement. However, we could not yet demonstrate that the spin state survives the transfer. A first limitation has been identified as being the difficulty to bring the dot with the transferred electrons from the reception configuration to a spin-measurement configuration

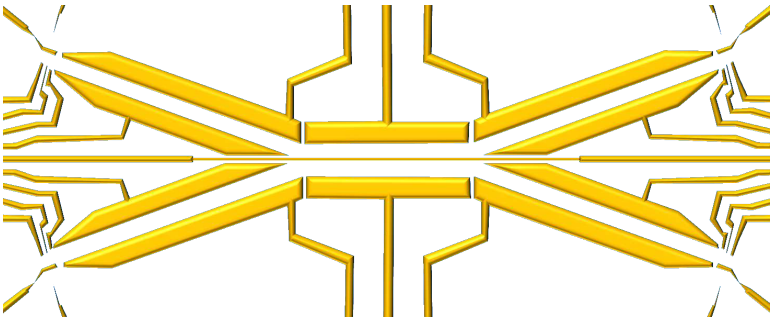

Figure 5.15: Proposed design to realise a Hanburry Brown and Twiss interferometer. The two 1DCs are set to interact through a tunnel barrier in the central part of the sample. The 4 dots will allow to trigger the injection of electrons and measure the full counting statistics of the outcomes.

without losing one of the charges. This question is presently investigated by Benoît Bertrand, a new Ph.D. student in our group who is following up my work.

The work realised during my Ph.D. opens up several perspectives. The high efficiency of the transfer should allow to retrieve the full counting statistics of the propagation. In addition, one could study the propagation through designed obstacles placed along the 1DC. For example, using two 1DCs brought close to each other, electron-electron collisions could be studied. Benoît Bertrand designed new samples in order to realise such experiments (shown in figure 5.15). The two left dots will be used as synchronised single-electron sources. Dragged by the SAW, the electrons will arrive in the central part of the sample where the two 1DCs are close to one another. The outcome of the collision can be measured event by event thanks to the two quantum dots on the right. Information on both charge and spin can be measured. In addition, the central barrier can be made smaller by changing the voltage applied to the thin central gate. It will then act as a beam splitter for the electrons, whose characteristics can be studied event by event. Using these tools, we can envision to realise quantum-optics experiments with "flying" electrons.

A long term goal is to use the transfer process that I developed in order to transport an electron-spin qubit. In order to test this transport, samples with double dots at each end of the 1DC, as presented in figure 5.16, have been designed. The double dot will allow to swap the spin states of two electrons, using well established methods exposed in chapter 1. The goal will be to transport one electron from a pair to the other side, generating an entangled pair of distant particles. The entanglement could then be swapped with two electron spins, one on each side of the 1DC. The measurement of

correlations between the latter will be a first step towards the demonstration of entanglement swapping with distant electron spins.

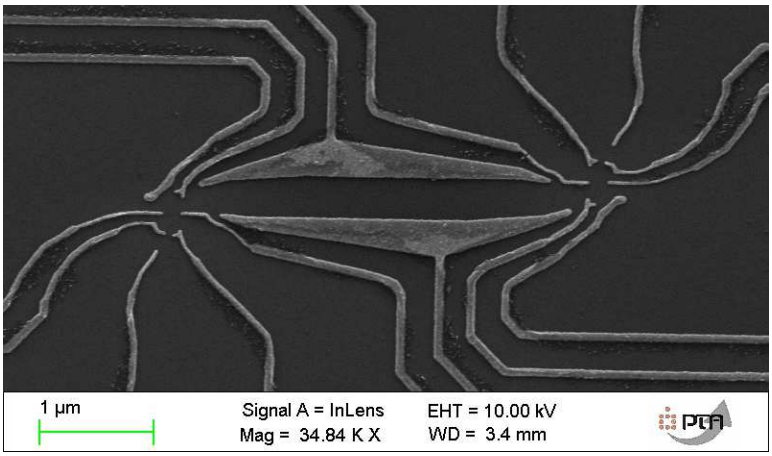

Figure 5.16: Sample proposed to test the entanglement between a separated pair of electrons. The double dots are necessary to apply logic gates on the qubits.

Another possibility opened by the single-electron transfer we demonstrated regards the scalability of a quantum computer based on electron-spin qubits. One could realise a 2D array of dots linked by 1D channels: SAWs can be generated on two orthogonal directions in GaAs, hence it should be possible to realise a square array of quantum dots. The addressability of the quantum dots in such a system has to be explored. Our results on the triggering of the transfer suggest that this point should not be an issue. If the current work suggests that it should be straightforward, the technical question of fitting all the components in a reduced surface has to be answered.

The realisation of a 2D array of qubits that can be entangled will be a major milestone towards the realisation of a scalable quantum computer. Other ideas are sought in order to realise such a device. For example, a recent proposal of Trifunovic *et al.* [74] suggests a way to couple distant double dots thanks to a direct electrostatic link.

As a last word, we can expect to see over the next years or decades very exciting developments and tests in the diverse directions mentioned here. A lot of interesting physics should be unravelled while we develop a quantum computer.

Conclusion et perpectives (Français)

Le but du travail réalisé lors de ma thèse, et décrit dans le présent mémoire, est d'explorer la faisabilité du transport d'un spin électronique unique afin d'intriquer des qubits distants. Au cours de ce projet, nous avons démontré qu'un électron unique peut être transféré à la demande d'une boîte quantique à une autre. Cette performance prend part à l'effort mondial en vue de la réalisation d'un ordinateur quantique : les rotations d'un spin électronique unique piégé dans une boîte quantique ont été démontrées, ainsi que l'intrication de deux qubits placés dans des boîtes juxtaposées.

Le dispositif expérimental nécessaire à la réalisation de cette tâche a été mis en place durant ma thèse. Il est constitué d'un dispositif cryogénique, d'électronique faible bruit, d'électronique radio-fréquence et d'un développement logiciel pour piloter les expériences. L'échantillon utilisé pour réaliser le transfert d'un électron unique est constitué de deux boîtes quantiques espacées de 3 µm, de contacts ponctuels quantiques (QPCs) qui mesurent la charge dans chaque boîte, d'un canal unidimensionnel qui guide et isole l'électron ainsi que de transducteurs interdigités (IDTs) pour générer l'onde acoustique de surface. Chacune des boîtes quantiques est amenée dans un régime où elle est peuplée par un seul électron. Nous avons exploré et démontré la possibilité d'isoler un électron des réservoirs et de l'amener plus haut en énergie que le niveau de Fermi. Il est montré que de tels états métatstables peuvent survivre jusqu'à 1 s. En utilisant un état métastable, l'électron est amené au près du canal 1D qui relie les deux boîtes. Une onde acoustique de surface peut alors transporter l'électron vers la seconde boîte quantique. Ce processus est réalisé avec une efficacité de 90 %. En vue du transport de qubits de spin, des premières mesures de spin ont été réalisées. La relaxation d'un système de deux électrons a été mesurée. Elle présente un temps caractéristique de l'ordre de 5 ms. Nous montrons que ce temps ne diminue pas lorsque des séquences de transfert d'électrons sont intercalées entre les répétitions de la mesure du spin. Cependant, la survie du spin durant le transfert reste à démontrer. Une première difficulté dans la réalisation de cette expérience a été identifiée : le changement de configuration

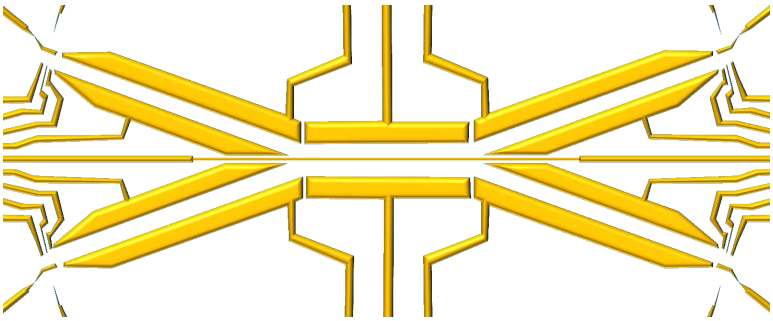

Figure 5.17: Dessin proposé pour réaliser des expériences d'optique quantique avec des électrons. Les électrons dans les deux canaux 1D interagissent à travers la barrière tunnel dans la partie centrale de l'échantillon. Les 4 boîtes quantiques permettront de synchroniser l'injection dans les deux branches et de mesurer l'intégralité de la statistique des collisions.

(réception vers mesure de spin) de la boîte de réception s'accompagne de la perte d'un au moins des électrons. Ce changement de configuration est actuellement étudié par Benoît Bertrand, un nouveau doctorant de l'équipe qui poursuit les travaux initiés lors de ma thèse.

La haute fiabilité du transfert suggère qu'il est possible d'utiliser ce système afin d'étudier plus en détails la propagation d'électrons entraînés par des SAWs : l'intégralité de la statistique liée à la propagation peut être obtenue (*full counting statistics*). Il est alors possible de placer des obstacles le long du canal 1D pour les étudier. Par exemple, il est envisageable de réaliser des collisions électron – électron. Benoît Bertrand a dessiné de nouveaux échantillons afin de réaliser une expérience de ce type (5.17). Deux boîtes quantiques seront utilisées comme sources synchronisées d'électrons uniques. Les deux canaux convergent ensuite vers la zone centrale de l'échantillon où ils sont proches l'un de l'autre. Le résultat de la collision sera alors collecté grâce aux deux boîtes de droite. L'information sur le spin et sur la charge pourra être mesurée. Une variation à cette expérience, consiste à rendre la barrière entre les deux canaux plus mince dans la région centrale en changeant la tension appliquée à la fine grille centrale. L'échantillon devrait alors devenir une lame séparatrice pour les électrons. Les propriétés de cette dernière pourront être étudiées évènement par évènement.

Un objectif à long terme est de transporter un qubit de spin. Dans cette optique, nous avons conçu des échantillons avec des doubles boîtes à chaque extrémité du canal 1D. Une image au microscope électronique à balayage de l'un d'entre eux est présentée figure 5.18. Les doubles boîtes permettront de réaliser l'échange de deux électrons (SWAP) en utilisant des méthodes connues, exposées au chapitre 1. L'idée sera de transporter un électron faisant

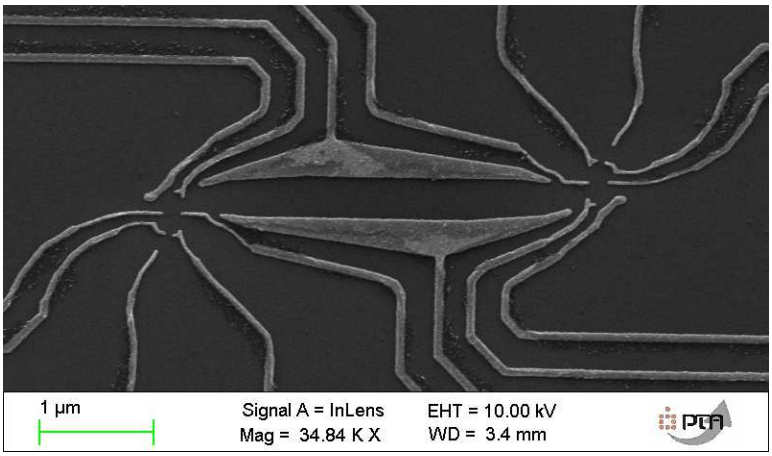

Figure 5.18: Échantillon proposé pour tester les inégalités de Bell sur une paire d'alectrons séparée. Les doubles boîtes sont nécessaires pour appliquer les rotations aux spins électroniques.

initialement partie d'un paire. Une paire d'électrons intriqués distants devrait alors être générée. L'intrication pourra alors être échangée avec deux spins électronique, un à chaque extrémité du canal 1D. La mesure des corrélations entre ces derniers devrait permettre une première mise en évidence d'échange d'intrication entre des spins électroniques distants.

Une autre possibilité ouverte par le transfer d'un unique électron que nous avons démontré touche à la possibilité d'intégrer un grand nombre de qubits de spin (*scalability*). Il doit être possible de réaliser un réseau 2D de boites quantiques reliées par des canaux 1D. Les SAWs peuvent être générées suivant deux directions orthogonales dans l'AsGa, la mise en relation des différentes boîtes placées sur un réseau carré doit donc être réalisable. L'adressage des boîtes quantiques devrait être immédiat à la vue du travail réalisé sur la synchronisation de l'envoi. La question de la mise en place de l'ensemble des éléments de lithographie nécessaires sur une surface réduite reste cependant ouverte.

La réalisation d'un réseau bidimensionnel de qubits qui puissent être intriqués sera une étape majeure vers la conception d'un ordinateur quantique à grand nombre de qubits. C'est pourquoi d'autres idées sont recherchées pour construire un tel dispositif. Par exemple, Trifunovic et coauteurs ont récemment proposé de réaliser un lien électrostatique entre des doubles boîtes distantes [74].

En conclusion, nous pouvons nous attendre au cours des années ou décennies à venir à voir de nombreux développements et tests dans les diverses directions évoquées ici. Une physique passionnante devrait être explorée et dévoilée en vue du développement d'un ordinateur quantique.

Bibliography

[1] R. Feynman, "Simulating physics with computers," *International Journal of Theoretical Physics*, vol. 21, no. 6, pp. 467–488, 1982.

[2] D. Deutsch, "Quantum Theory, the Church-Turing Principle and the Universal Quantum Computer," *Proceedings of the Royal Society of London. A. Mathematical and Physical Sciences*, vol. 400, no. 1818, pp. 97–117, 1985.

[3] P. W. Shor, "Algorithms for quantum computation: discrete logarithms and factoring.," in *Foundations of Computer Science, 1994 Proceedings., 35th Annual Symposium on*, (Los Alamitos, CA), pp. 124–134, IEEE Comp. Soc. Press, 1994.

[4] L. K. Grover, "A fast quantum mechanical algorithm for database search.," in *28th Annual ACM Symposium on the Theory of Computing*, p. 212, May 1996. p. 212.

[5] D. P. DiVincenzo, "Quantum Computation," *Science*, vol. 270, no. 5234, pp. 255–261, 1995.

[6] P. W. Shor, "Fault-tolerant quantum computation," in *Foundations of Computer Science, 1996. Proceedings., 37th Annual Symposium on* (I. C. Soc., ed.), (Burlington, VT , USA), October 1996 .

[7] L. M. K. Vandersypen, M. Steffen, M. H. Sherwood, C. S. Yannoni, G. Breyta, and I. L. Chuang, "Implementation of a three-quantum-bit search algorithm," *Applied Physics Letters*, vol. 76, no. 5, pp. 646–648, 2000.

[8] L. M. K. Vandersypen, M. Steffen, G. Breyta, C. S. Yannoni, M. H. Sherwood, and I. L. Chuang, "Experimental realization of Shor's quantum factoring algorithm using nuclear magnetic resonance," *Nature*, vol. 414, no. 6866, pp. 883–887, 2001.

[9] D. Loss and D. P. DiVincenzo, "Quantum computation with quantum dots," *Phys. Rev. A*, vol. 57, pp. 120–126, Jan 1998.

[10] S. Fasel, N. Gisin, G. Ribordy, and H. Zbinden, "Quantum key distribution over 30 km of standard fiber using energy-time entangled photon pairs: a comparison of two chromatic dispersion reduction methods," *The European Physical Journal D*, vol. 30, no. 1, p. 143, 2004.

[11] M. Trif, V. N. Golovach, and D. Loss, "Spin dynamics in InAs nanowire quantum dots coupled to a transmission line," *Physical Review B*, vol. 77, no. 4, 2008.

[12] M. J. Hoskins, H. Morkoç, and B. J. Hunsinger, "Charge transport by surface acoustic waves in GaAs," *Applied Physics Letters*, vol. 41, no. 4, pp. 332–334, 1982.

[13] J. A. H. Stotz, R. Hey, P. V. Santos, and K. H. Ploog, "Coherent spin transport through dynamic quantum dots," *Nature Materials*, vol. 4, no. 8, pp. 585–588, 2005.

[14] J. A. H. Stotz, R. Hey, P. V. Santos, and K. H. Ploog, "Enhanced spin coherence via mesoscopic confinement during acoustically induced transport," *New Journal of Physics*, vol. 10, no. 9, pp. 093013–10, 2008.

[15] M. I. D'yakonov and V. I. Perel', "Spin relaxation of conduction electrons in noncentrosymmetric semiconductors," *Soviet Physis - Solid State*, vol. 13, no. 12, pp. 3023–3026, 1972.

[16] A. W. Harrow, A. Hassidim, and S. Lloyd, "Quantum Algorithm for Linear Systems of Equations," *Phys. Rev. Lett.*, vol. 103, p. 150502, Oct 2009.

[17] A. Messiah, *Mécanique quantique*, vol. 1. 1965.

[18] M. Kataoka, R. J. Schneble, A. L. Thorn, C. H. W. Barnes, C. J. B. Ford, D. Anderson, G. A. C. Jones, I. Farrer, D. A. Ritchie, and M. Pepper, "Single-Electron Population and Depopulation of an Isolated Quantum Dot Using a Surface-Acoustic-Wave Pulse," *Phys. Rev. Lett.*, vol. 98, p. 046801, Jan 2007.

[19] M. Ciorga, A. S. Sachrajda, P. Hawrylak, C. Gould, P. Zawadzki, S. Jullian, Y. Feng, and Z. Wasilewski, "Addition spectrum of a lateral dot from Coulomb and spin-blockade spectroscopy," *Phys. Rev. B*, vol. 61, pp. –16315, Jun 2000.

[20] D. A. Wharam, T. J. Thornton, R. Newbury, M. Pepper, H. Ahmed, J. E. F. Frost, D. G. Hasko, D. C. Peacock, D. A. Ritchie, and G. A. C. Jones, "One-dimensional transport and the quantisation of the ballistic resistance," *Journal of Physics C: Solid State Physics (1968-1988)*, vol. 21, no. 8, pp. –209, 1988.

[21] C. Rössler, S. Baer, E. d. Wiljes, P. L. Ardelt, T. Ihn, K. Ensslin, C. Reichl, and W. Wegscheider, "Transport Properties of Clean Quantum Point Contacts," *New Journal of Physics*, vol. 13, p. 113006, 2011.

[22] M. Field, C. G. Smith, M. Pepper, D. A. Ritchie, J. E. F. Frost, G. A. C. Jones, and D. G. Hasko, "Measurements of Coulomb blockade with a noninvasive voltage probe," *Phys. Rev. Lett.*, vol. 70, pp. 1311–1314, Mar 1993.

[23] J. H. Davies, I. A. Larkin, and E. V. Sukhorukov, "Modeling the patterned two-dimensional electron gas: Electrostatics," *Journal of Applied Physics*, vol. 77, no. 9, pp. 4504–4512, 1995.

[24] T. Hayashi, T. Fujisawa, H. Cheong, Y. Jeong, and Y. Hirayama, "Coherent Manipulation of Electronic States in a Double Quantum Dot," *Physical Review Letters*, vol. 91, no. 22, 2003.

[25] K. Petersson, J. Petta, H. Lu, and A. Gossard, "Quantum Coherence in a One-Electron Semiconductor Charge Qubit," *Physical Review Letters*, vol. 105, no. 24, 2010.

[26] J. M. Elzerman, R. Hanson, L. H. Willems van Beveren, B. Witkamp, L. M. K. Vandersypen, and L. P. Kouwenhoven, "Single-shot read-out of an individual electron spin in a quantum dot," *nature*, vol. 430, no. 6998, pp. 431–435, 2004.

[27] S. Amasha, K. MacLean, I. Radu, D. Zumbühl, M. Kastner, M. Hanson, and A. Gossard, "Electrical Control of Spin Relaxation in a Quantum Dot," *Physical Review Letters*, vol. 100, no. 4, 2008.

[28] V. N. Golovach, A. Khaetskii, and D. Loss, "Phonon-Induced Decay of the Electron Spin in Quantum Dots," *Physical Review Letters*, vol. 93, no. 1, 2004.

[29] K. Schulten and P. G. Wolynes, "Semiclassical description of electron spin motion in radicals including the effect of electron hopping," *Journal of Chemical Physics*, vol. 68, no. 7, pp. 3292–3297, 1978.

[30] I. A. Merkulov, A. L. Efros, and M. Rosen, "Electron spin relaxation by nuclei in semiconductor quantum dots," *Phys. Rev. B*, vol. 65, p. 205309, Apr 2002.

[31] J. R. Petta, A. C. Johnson, J. M. Taylor, E. A. Laird, A. Yacoby, M. D. Lukin, C. M. Marcus, M. P. Hanson, and A. C. Gossard, "Coherent Manipulation of Coupled Electron Spins in Semiconductor Quantum Dots," *Science*, vol. 309, no. 5744, pp. 2180–2184, 2005.

[32] J. M. Taylor, J. R. Petta, A. C. Johnson, A. Yacoby, C. M. Marcus, and M. D. Lukin, "Relaxation, dephasing, and quantum control of electron spins in double quantum dots," *Phys. Rev. B*, vol. 76, p. 035315, Jul 2007.

[33] E. A. Laird, J. M. Taylor, D. P. DiVincenzo, C. M. Marcus, M. P. Hanson, and A. C. Gossard, "Coherent spin manipulation in an exchange-only qubit," *Phys. Rev. B*, vol. 82, p. 075403, Aug 2010.

[34] H. Bluhm, S. Foletti, I. Neder, M. Rudner, D. Mahalu, V. Umansky, and A. Yacoby, "Dephasing time of GaAs electron-spin qubits coupled to a nuclear bath exceeding 200 µs," *Nature Physics*, vol. 7, no. 2, pp. 109–113, 2011.

[35] F. H. L. Koppens, C. Buizert, K. J. Tielrooij, I. T. Vink, K. C. Nowack, T. Meunier, L. P. Kouwenhoven, and L. M. K. Vandersypen, "Driven coherent oscillations of a single electron spin in a quantum dot," *Nature*, vol. 442, no. 7104, pp. 766–771, 2006.

[36] K. C. Nowack, F. H. L. Koppens, Y. V. Nazarov, and L. M. K. Vandersypen, "Coherent Control of a Single Electron Spin with Electric Fields," *Science*, vol. 318, no. 5855, pp. 1430–1433, 2007.

[37] W. Coish and D. Loss, "Hyperfine interaction in a quantum dot: Non-Markovian electron spin dynamics," *Physical Review B*, vol. 70, no. 19, 2004.

[38] M. Pioro-Ladrière, T. Obata, Y. Tokura, Y.-S. Shin, T. Kubo, K. Yoshida, T. Taniyama, and S. Tarucha, "Electrically driven single-electron spin resonance in a slanting Zeeman field," *Nature Physics*, vol. 4, no. 10, p. 776, 2008.

[39] W. A. Coish and D. Loss, "Singlet-triplet decoherence due to nuclear spins in a double quantum dot," *Physical Review B*, vol. 72, no. 12, 2005.

[40] M. V. G. Dutt, J. Cheng, B. Li, X. Xu, X. Li, P. R. Berman, D. G. Steel, A. S. Bracker, D. Gammon, S. E. Economou, R.-B. Liu, and L. J. Sham, "Stimulated and Spontaneous Optical Generation of Electron Spin Coherence in Charged GaAs Quantum Dots," *Phys. Rev. Lett.*, vol. 94, p. 227403, Jun 2005.

[41] A. C. Johnson, J. R. Petta, J. M. Taylor, A. Yacoby, M. D. Lukin, C. M. Marcus, M. P. Hanson, and A. C. Gossard, "Triplet-singlet spin relaxation via nuclei in a double quantum dot.," *Nature*, vol. 435, no. 7044, pp. 925–8, 2005.

[42] F. H. L. Koppens, J. A. Folk, J. M. Elzerman, R. Hanson, L. H. W. van Beveren, I. T. Vink, H. P. Tranitz, W. Wegscheider, L. P. Kouwenhoven, and L. M. K. Vandersypen, "Control and Detection of Singlet-Triplet Mixing in a Random Nuclear Field," *Science*, vol. 309, no. 5739, pp. 1346–1350, 2005.

[43] I. van Weperen, B. D. Armstrong, E. A. Laird, J. Medford, C. M. Marcus, M. P. Hanson, and A. C. Gossard, "Charge-State Conditional Operation of a Spin Qubit," *Phys. Rev. Lett.*, vol. 107, p. 030506, Jul 2011.

[44] O. Dial, "Demonstration of entanglement of two GaAs singlet-triplet qubits," (QSPICE II, Workshop on Quantum Spintronics), October 2011. Ottiolu, Sardinia, Italy.

[45] S. Foletti, H. Bluhm, D. Mahalu, V. Umansky, and A. Yacoby, "Universal quantum control of two-electron spin quantum bits using dynamic nuclear polarization," *Nature Physics*, vol. 5, no. 12, pp. 903–908, 2009.

[46] H. Bluhm, S. Foletti, I. Neder, M. Rudner, D. Mahalu, V. Umansky, and A. Yacoby, "Dephasing time of GaAs electron-spin qubits coupled to a nuclear bath exceeding 200 μs," *Nature Physics*, vol. 7, no. 2, p. 109, 2011.

[47] L. Gaudreau, G. Granger, A. Kam, G. C. Aers, S. A. Studenikin, P. Zawadzki, M. Pioro-Ladrière, Z. R. Wasilewski, and A. S. Sachrajda, "Coherent control of three-spin states in a triple quantum dot," *Nature Physics*, vol. 8, pp. 54–58, 2011.

[48] C. Marcus, "An exchange-only spin qubit.," (QSPICE II, workshop on quantum spintronics), October 2011. Ottiolu, Sardinia, Italy.

[49] R. H. Parmenter, "The Acousto-Electric Effect," *Phys. Rev.*, vol. 89, pp. 990–998, Mar 1953.

[50] S. D. Gaalema, R. J. Schwartz, and R. L. Gunshor, "Acoustic surface wave interaction charge-coupled device," *Applied Physics Letters*, vol. 29, no. 2, pp. 82–83, 1976.

[51] J. M. Shilton, V. I. Talyanskii, M. Pepper, D. A. Ritchie, J. E. F. Frost, C. J. B. Ford, C. G. Smith, and G. A. C. Jones, "High-frequency single-electron transport in a quasi-one-dimensional GaAs channel induced by surface acoustic waves," *Journal of Physics: Condensed Matter*, vol. 8, no. 38, pp. L531–L539, 1996.

[52] A. M. Robinson, V. I. Talyanskii, M. Pepper, J. E. Cunningham, E. H. Linfield, and D. A. Ritchie, "Measurements of noise caused by switching of impurity states and of suppression of shot noise in surface-acoustic-wave-based single-electron pumps," *Phys. Rev. B*, vol. 65, p. 045313, Jan 2002.

[53] G. R. Aĭzin, G. Gumbs, and M. Pepper, "Screening of the surface-acoustic-wave potential by a metal gate and the quantization of the acoustoelectric current in a narrow channel," *Phys. Rev. B*, vol. 58, pp. 10589–10596, Oct 1998.

[54] K. Flensberg, Q. Niu, and M. Pustilnik, "Nonadiabaticity and single-electron transport driven by surface acoustic waves," *Phys. Rev. B*, vol. 60, pp. –16291, Dec 1999.

[55] M. Astley, M. Kataoka, C. Ford, C. Barnes, D. Anderson, G. Jones, I. Farrer, D. Ritchie, and M. Pepper, "Energy-Dependent Tunneling from Few-Electron Dynamic Quantum Dots," *Physical Review Letters*, vol. 99, no. 15, 2007.

[56] K. F. Graff, *Wave motion in elastic solids.* Oxford University Press, 1975.

[57] W. D. Hunt, Y. Kim, and F. M. Fliegel, "A synopsis of surface acoustic wave propagation on {100}-cut <110>-propagating gallium arsenide," *Journal of Applied Physics*, vol. 69, no. 4, pp. 1936–1941, 1991.

[58] S. Adachi, "GaAs, AlAs, and $Al_xGa_{1-x}As$: Material parameters for use in research and device applications," *Journal of Applied Physics*, vol. 58, no. 3, pp. –1, 1985.

[59] M. M. d. Lima, F. Alsina, W. Seidel, and P. V. Santos, "Focusing of surface-acoustic-wave fields on (100) GaAs surfaces," *Journal of Applied Physics*, vol. 94, no. 12, pp. 7848–7855, 2003.

[60] G. Weinreich, "Acoustodynamic Effects in Semiconductors," *Phys. Rev.*, vol. 104, pp. 321–324, Oct 1956.

[61] G. Weinreich and H. G. White, "Observation of the Acoustoelectric Effect," *Phys. Rev.*, vol. 106, pp. 1104–1106, Jun 1957.

[62] R. J. Schneble, M. Kataoka, C. J. B. Ford, C. H. W. Barnes, D. Anderson, G. A. C. Jones, I. Farrer, D. A. Ritchie, and M. Pepper, "Quantum-dot thermometry of electron heating by surface acoustic waves," *Applied Physics Letters*, vol. 89, no. 12, p. 122104, 2006.

[63] F. Pobell, *Matter and methods at low temperatures.* Springer, 2007.

[64] O. V. Lounasmaa, *Experimental Principles and Methods Below 1k.* London: Academic Press, 1974.

[65] R. Schleser, E. Ruh, T. Ihn, K. Ensslin, D. C. Driscoll, and A. C. Gossard, "Time-resolved detection of individual electrons in a quantum dot," *Applied Physics Letters*, vol. 85, no. 11, pp. 2005–2007, 2004.

[66] R. Crook, R. Schneble, M. Kataoka, H. Beere, D. Ritchie, D. Anderson, G. Jones, C. Smith, C. Ford, and C. Barnes, "Scanned gate microscopy of surface-acoustic-wave-induced current through a depleted one-dimensional GaAs channel," *Physical Review B*, vol. 82, no. 16, 2010.

[67] R. P. G. McNeil, M. Kataoka, C. J. B. Ford, C. H. W. Barnes, D. Anderson, G. A. C. Jones, I. Farrer, and D. A. Ritchie, "On-demand single-electron transfer between distant quantum dots," *Nature*, vol. 477, no. 7365, pp. 439–442, 2011.

[68] R. Hanson, L. H. W. v. Beveren, I. T. Vink, J. M. Elzerman, W. J. M. Naber, F. H. L. Koppens, L. P. Kouwenhoven, and L. M. K. Vandersypen, "Single-shot readout of electron spin states in a quantum dot using spin-dependent tunnel rates," *Physical Review Letters*, vol. 94, p. 196802, 2005.

[69] T. Meunier, K. J. Tielrooij, I. T. Vink, F. H. L. Koppens, H. P. Tranitz, W. Wegscheider, L. P. Kouwenhoven, and L. M. K. Vandersypen, "High fidelity measurement of singlet–triplet state in a quantum dot," *physica status solidi (b)*, vol. 243, no. 15, pp. 3855–3858, 2006.

[70] S. Amasha, K. MacLean, I. Radu, D. Zumbühl, M. Kastner, M. Hanson, and A. Gossard, "Spin-dependent tunneling of single electrons into an empty quantum dot," *Physical Review B*, vol. 78, p. 041306, Jul 2008.

[71] L. P. Kouwenhoven, D. G. Austing, and S. Tarucha, "Few-electron quantum dots," *Reports on Progress in Physics*, vol. 64, no. 6, p. 701, 2001.

[72] J. M. Elzerman, R. Hanson, L. H. W. v. Beveren, L. M. K. Vandersypen, and L. P. Kouwenhoven, "Excited-state spectroscopy on a nearly closed quantum dot via charge detection," *Applied Physics Letters*, vol. 84, no. 23, pp. 4617–4619, 2004.

[73] R. Hanson, J. R. Petta, S. Tarucha, and L. M. K. Vandersypen, "Spins in few-electron quantum dots," *Reviews of Modern Physics*, vol. 79, no. 4, p. 1217, 2007.

[74] L. Trifunovic, O. Dial, M. Trif, J. R. Wootton, R. Abebe, A. Yacoby, and D. Loss, "Long-distance spin-spin coupling via floating gates," *arXiv*, 2011.

[75] S. Hermelin, S. Takada, M. Yamamoto, S. Tarucha, A. D. Wieck, L. Saminadayar, C. Bäuerle, and T. Meunier, "Electrons surfing on a sound wave as a platform for quantum optics with flying electrons.," *Nature*, vol. 477, no. 7365, pp. 435–8, 2011.

Appendix A

Nanofabrication

introduction

In order to go from a 2DEG to quantum dots, small-scale patterns on the GaAs heterostructure have to be defined. As shown in section 1.2, metallic gates of size on the order of a few tens of nanometres have to be added on top of the structure. Moreover, some parts of the sample usually have to be etched. In this chapter, we will briefly discuss the different steps for sample fabrication, starting from the heterostructure.

A.1 Alignment marks

The first step in the fabrication of a sample are alignment marks. Indeed, the fabrication process is layered, hence the different steps need to be aligned up to a given resolution. The easiest way to achieve this is to start with a reference layer with marks. These marks will be used as absolute coordinate references.

Technically speaking, the layer consists of two families of marks: large ones and small ones. The former are crosses hundreds of microns long, with a line width of a few tens of micrometres. These crosses can be seen with an optical microscope and hence allow to optically align patterns on top of it. The aligning resolution will be on the order of a micron. The smaller crosses will be around ten-microns sized with a line width on the order of a few microns. They will be used to align the finer patterns, realised by electron-beam lithography, as shall be discussed further. This technique allows alignments better than 100 nm.

These crosses are all realised at once by optical lithography: a layer of resist 2 µm thick is spin-coated on the wafer. The spin coating ensures a regular thickness of the film.[1] The resist is then exposed to ultra-violet

1. Note that since high-mobility heterostructures are quite a precious material, the sample size is usually limited. As a consequence, very strong side effects alter the thickness

light through a patterned mask [2]. The UV exposure chemically weakens the resist. Hence a chemical development allows to remove the exposed parts of resist and the pattern of the mask are now duplicated on a mask made of resist, which is in direct contact with the wafer. The next step consists of evaporating metal on top of the sample, through this resist mask, under vacuum. The final process step, called lift-off, consists of removing the resist with acetone – or any adapted solvent. Only the metal that is directly stuck to the wafer should stay after this step. The overall process, shown in figure A.1, hence allowed to reproduce the patterns of the mask in metal strips on top of the sample.

A.2 Mesa

The samples we use are typically millimetre-sized. Since the physics we seek takes place in nano-structures, only the 2DEG in a smaller region is of interest. We then etch away parts of the wafer that are not interesting. Two major ways can be followed. The first consists in preparing a resist mask and etching chemically the structure. It is to be noted that the crystalline structure of the wafer causes anisotropic etching. The anisotropy will depend mostly on the chemical composition of the etchant; the temperature will lead the etching speed. For the common mixture of sulphuric acid, hydrogen peroxide and water used, it is necessary to work around ten degrees to etch at a speed of $100\,\mathrm{nm\,min^{-1}}$. An other way is to use a physical etching: an aluminium mask is prepared through the usual lithographic techniques and the wafer is then bombarded with an argon plasma. The ions of the plasma etch the structure during the collision. The etching rate we usually reach are on the order of $5\,\mathrm{nm\,min^{-1}}$.The aluminium mask is subsequently etched by caustic soda. In both cases, the actual etch rate is determined by trial and error by regularly measuring the depth etched. The part of the sample that is not etched is commonly called the mesa.

A.3 Ohmic contacts

As mentioned in section 1.2, the 2DEG needs to be electrically contacted to measuring apparatus. This is realised by ohmic contacts. They consist of an annealed alloy or mix of nickel, gold and germanium. The annealing usually is fast (1 min) under a controlled atmosphere of hydrogen and nitrogen. The high-temperature step allows for the germanium to migrate through the wafer to the 2DEG layer, hence allowing the electrical contact.

of the resist around the sample edges.

2. The masks used for my Ph.D. were either home made in the university of Tokyo or commercial, from Toppan Photomasks inc., using electron-beam lithography.

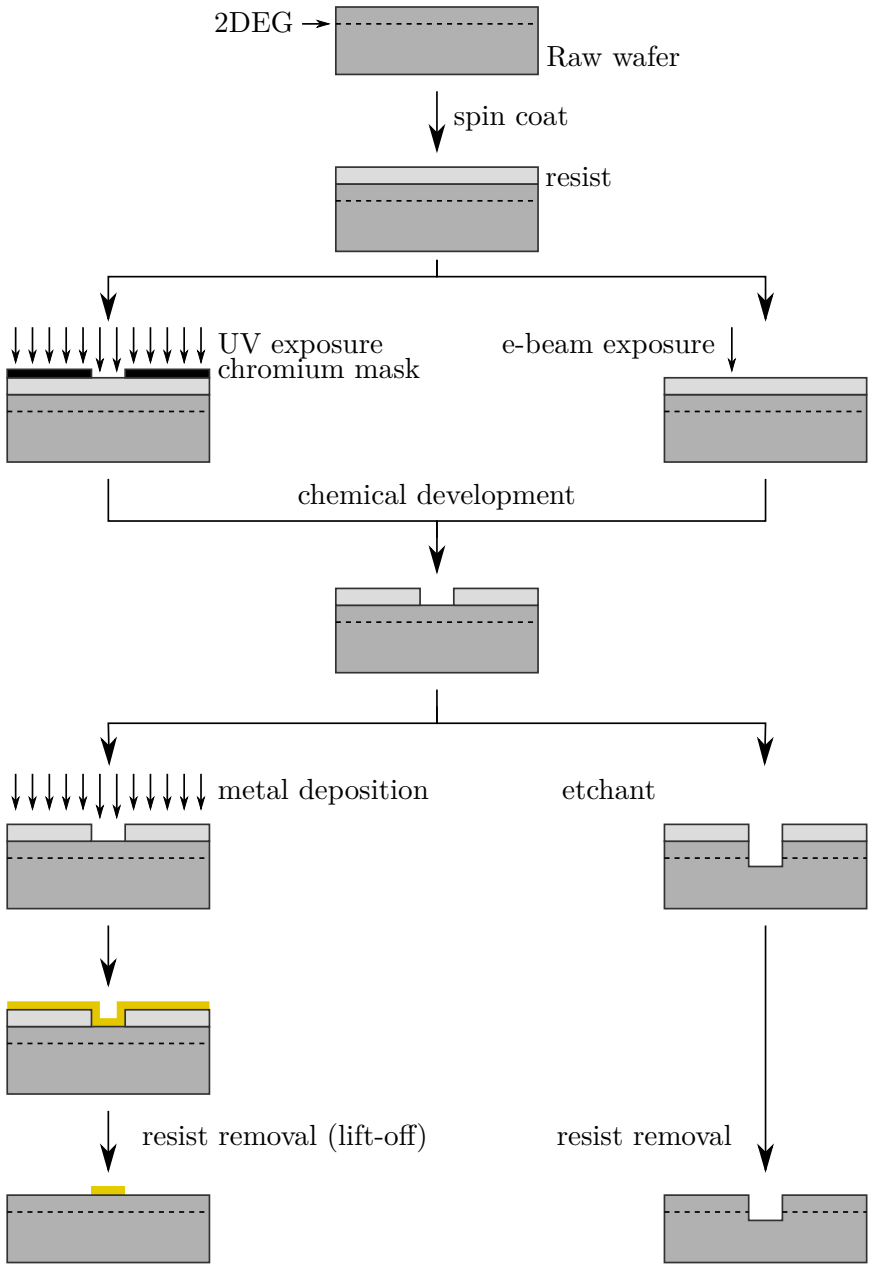

Figure A.1: Main fabrication techniques. Starting from a raw wafer, one can pattern metallic strips (bottom left) or etch parts of the wafer (bottom right). The resolution for any will depend on the technique used: optical lithography for patterns bigger than a micron (top left) or electron-beam lithography for patterns down to 20 nm (top right). For etching, the etch method will also have an influence on the resolution.

A.4 Gates

The metallic gates, made of gold [3], are realised in two steps. First, the finer parts are realised with e-beam lithography. Later, the bigger parts are realised by optical lithography. The two steps allow for thicker metal gates on the outer parts of the sample, thus lowering the number of cut gates, especially when going from the etched part of the wafer onto the mesa. The step height is indeed more than 100 nm and metal thickness greater than 100 nm is used to better ensure electrical contact throughout the step.

A.5 Micro-bonding

The sample, once ready is glued using GE Varnish to a chip carrier. The latter features gold-plated copper strips from a central part towards macroscopic connectors to allow rapid mounting on the fridge. Thus, the gates, ohmic contacts and IDT pads have to be wired to these metal strips. This is achieved with aluminium wires, micro-bonded using ultrasound.

A.6 Recipes

We will here list the recipes used in Grenoble to realise similar samples.

A.6.1 Optical lithography (thin plating)

The resist used is a bilayer of LOR3A (400 nm) and UV3 (300 nm). LOR3A is a general purpose layer to get undercut under other resists. Its use makes the lift-off step much easier and help to get "cleaner" edges for the deposited metal. This recipe allows for metal depositions up to 200 nm. Proceed as follows:

Clean the sample.

Resist:

- spin coat LOR3A, 2000 rpm, 2000 rpm/s, 30 s
- hotplate bake, 170 °C, 30 s
- spin coat UV3, 4000 rpm, 2000 rpm/s, 30 s
- hotplate bake, 130 °C, 1 min

Exposure: deep UV, 15 to 16 s

Post-exposure bake: hotplate, 130 °C, 1 min

Development: LDD26W or MFCD26 for 55 to 60 s

Metal deposition (up to $\simeq$200 nm)

Lift-off: acetone followed by PG remover at 70 °C for 1 h30 min

Dry: N_2 blow dry.

3. and titanium as a sticking layer

A.6.2 Optical lithography (thick plating)

The resist used is a mono-layer S1818 (1.8 µm). The deposited metal thickness can be up to 600 nm.

Clean the sample.

Resist:
- spin coat S1818, 4000 rpm, 2000 rpm/s, 60 s
- hotplate bake, 80 °C, 60 s

Exposure: UV, 20 s

Development

Metal deposition (up to $\simeq$ 600 nm)

Lift-off: overnight acetone, Pasteur pipette agitation if needed

Dry: N_2 blow dry.

A.6.3 Alignment marks

Clean: no ultrasound (fine gates already patterned and fragile)

Resist: LOR3A/UV3 (cf. A.6.1).

Deposition:
- 20nm titanium
- $\geq$100nm gold

Lift-off: proceed as for fine gate, except without the ultrasound.

A.6.4 Ion-beam etching of the mesa

Clean:
- ultrasound in acetone, 10 min.
- ultrasound in IPA [4], 5 min.
- IPA rinse
- N_2 blow dry.

Resist: LOR3A/UV3 (cf. A.6.1)

Deposition: 75 nm aluminium mask deposition.

Ion beam etching (IBE) etching (argon):
- RF power: 600 W
- Ar pressure: 1.5×10^{-4} Torr
- incidence angle for the ions beam: 35°
- $\simeq 0°4'30''$ to etch 50 nm
- profilometer check of depth etched (etching of Al much slower than that of GaAs)

Aluminium mask removal:
- $\simeq$1 min in caustic soda ($> 1\,\mathrm{mol\,l^{-1}}$)
- DI water rinse
- oven dry (optional): 115 °C, 5 to 10 min

4. isopropyl alcohol

Clean:
- ultrasound in acetone, 5 min.
- ultrasound in IPA, 5 min.
- IPA rinse.
- N_2 blow dry.

A.6.5 Chemical etching of the mesa

Preparation: – ultrasound in acetone, 5 min.
- ultrasound in IPA, 5 min.
- IPA rinse.
- N_2 blow dry.

Resist:
- AZ27, 500 rpm, 30 s, 7 s slope to 4000 rpm, 40 s,
- hotplate bake, 80 °C, 5 min.

UV Insulation.
Oven bake: 110 °C, 20 min.
Chemical etch: – H_2O_2:H_2SO_4:H_2O 1:5:25 at 10 °C, 1 min for $\simeq$ 100 nm
- DI water stop
- check etch depth, repeat if necessary (resist is not etched by the acidic solution)

Clean: – ultrasound in acetone, 5 min.
- ultrasound in IPA, 5 min.
- IPA rinse
- N_2 blow dry.

A.6.6 Ohmic contacts

Resist: S1818 (cf. A.6.1)
Deposition:
- 10 nm nickel
- 60 nm germanium
- 120 nm gold
- 20 nm nickel
- 200 nm gold

Rapid thermal annealing:
- under H_2 atmosphere [5],
- 400 °C, 1 min

A.6.7 Fine gates

Clean: without ultrasound, oven dry 115 °C, 10 min
Resist:

5. the oven has to be flushed of air—oxygen—with N_2

- OEBR 1000:OFPR 800 3:2[6], 4000 rpm, 50 s,
- hotplate bake, 180 °C, 3 min.

Exposure: electron beam, 650 to 800 µC cm^{-2}
Development:
- MIBK[7]:IPA 1:3, 60 s,
- stop with IPA, 60 s.
- no N_2 blow dry (or extremely soft), since it can push the resist edges in the defined patterns.

Deposition: – 5 to 10 nm titanium
- 20 to 25 nm gold

Lift-off: – overnight dip in acetone,
- soft ultrasound for around 5 second
- Pasteur pipette-agitation,
- acetone rinse,
- IPA rinse,
- very soft N_2 blow dry.

A.6.8 Large gates

Clean: no ultrasound (fine gates already patterned and fragile)
Resist: LOR3A/UV3 (cf. A.6.1).
Deposition:
- 20nm titanium
- ≥100nm gold

Lift-off: proceed as for fine gate, except without the ultrasound.

6. 3 for 2 in volume
7. Methyl IsoButyl ketone

Appendix B

Article

We include here the letter to Nature, published September, 2011, related to the results discussed in chapter 4.

LETTER

doi:10.1038/nature10416

Electrons surfing on a sound wave as a platform for quantum optics with flying electrons

Sylvain Hermelin[1], Shintaro Takada[2], Michihisa Yamamoto[2,3], Seigo Tarucha[2,4], Andreas D. Wieck[5], Laurent Saminadayar[1,6], Christopher Bäuerle[1] & Tristan Meunier[1]

Electrons in a metal are indistinguishable particles that interact strongly with other electrons and their environment. Isolating and detecting a single flying electron after propagation, in a similar manner to quantum optics experiments with single photons[1,2], is therefore a challenging task. So far only a few experiments have been performed in a high-mobility two-dimensional electron gas in which the electron propagates almost ballistically[3–5]. In these previous works, flying electrons were detected by means of the current generated by an ensemble of electrons, and electron correlations were encrypted in the current noise. Here we demonstrate the experimental realization of high-efficiency single-electron source and detector for a single electron propagating isolated from the other electrons through a one-dimensional channel. The moving potential is excited by a surface acoustic wave, which carries the single electron along the one-dimensional channel at a speed of 3 μm ns^{-1}. When this quantum channel is placed between two quantum dots several micrometres apart, a single electron can be transported from one quantum dot to the other with quantum efficiencies of emission and detection of 96% and 92%, respectively. Furthermore, the transfer of the electron can be triggered on a timescale shorter than the coherence time T_2* of GaAs spin qubits[6]. Our work opens new avenues with which to study the teleportation of a single electron spin and the distant interaction between spatially separated qubits in a condensed-matter system.

Quantum electron optics is a field aiming at the realization of photon experiments with flying electrons in nanostructures at the single-electron level. Important tools with which to infer complex photon correlations inaccessible from ensemble measurements are single-photon sources and single-photon detectors. In contrast with photons, electrons are strongly interacting particles and they usually propagate in a Fermi sea filled with other electrons. Each electron therefore inevitably mixes with the others of the Fermi sea, which implies that the quantum information stored within the charge or the spin of the single electron will be lost over short lengths. To perform quantum electron-optical experiments at the single-electron level, one therefore needs a source of single electrons, a controlled propagating medium and a single-electron detector. It has been proposed that edge states in the quantum Hall effect can serve as a one-dimensional (1D) propagating channel for flying electrons. As a result of Coulomb blockade, quantum dots have been demonstrated to be a good source of single electrons[7,8] and can also serve as a single-electron detector. Indeed, once an electron has been stored in a quantum dot, its presence can be inferred routinely by charge detection[9]. Nevertheless, re-trapping the electron in another quantum dot after propagation in an edge state turns out to be extremely difficult, and currently all the information extracted from such experiments is coming from ensemble measurements[10,11]. Here we show that a single flying electron—an electron surfing on a sound wave—can be sent on demand from a quantum dot by means of a 1D quantum channel and re-trapped in a second quantum dot after propagation. The 1D quantum channel consists of a depleted region several micrometres long in a two-dimensional electron gas (2DEG). The electron is dragged along by exciting a surface acoustic wave (SAW) and propagates isolated from the other electrons inside the 1D channel[12]. The processes of loading and unloading of the flying electron from the quantum channel into a quantum dot turn out to be highly efficient. Moreover, we show that the transfer of the electron can be triggered with a timescale smaller than the coherence time T_2* of GaAs spin qubits[6]. Because both electron spin directions are treated on the same foot in the SAW quantum channel, one expects that the spin coherence during the transport is conserved. Naturally, new possibilities will emerge to address the question of scalability in spin qubit systems[6,13,14].

To transport a single electron from one quantum dot to the other separated by a 3-μm 1D channel (see Fig. 1 and Methods), the following procedure is applied. First, the region between the two electrodes, which define the 1D channel, is fully depleted. As a consequence, direct linear electron transport from one end of the channel to the other is blocked because the Fermi energy lies below the potential induced by the gates. Second, by applying microwave excitation to the interdigitated transducer (IDT), SAW-induced moving quantum dots are generated[12] as a result of the piezoelectric properties of GaAs (see also Supplementary Information). By adding a quantum dot to each side of the 1D channel and tuning both quantum dots into the single electron regime, it is then possible to transport a single electron from one quantum dot across the 1D channel and catch it inside the second quantum dot. Stability diagrams for both quantum dots as a function

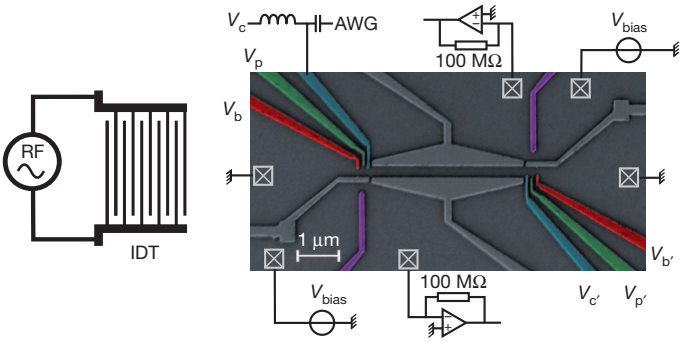

Figure 1 | Experimental device and measurement setup. Scanning electron microscope image of the single-electron transfer device, and diagram of the experimental setup. Two quantum dots, which can be brought into the single-electron regime, are separated by a 1D channel 3 μm long, as shown. Each quantum dot is capacitively coupled to a QPC close by that is used as an electrometer[9]. By applying a microwave burst 65 ns long on the IDT (see Methods for details), a train of about 150 moving quantum dots is created in the 1D channel. Gate V_c is connected to a home-made bias tee to allow nanosecond manipulation of the dot potential. RF, radio frequency.

[1]Institut Néel, CNRS, and Université Joseph Fourier, 38042 Grenoble, France. [2]Department of Applied Physics, University of Tokyo, Tokyo, 113-8656, Japan. [3]ERATO-JST, Kawaguchi-shi, Saitama 331-0012, Japan. [4]ICORP (International Cooperative Research Project) Quantum Spin Information Project, Atsugi-shi, Kanagawa, 243-0198, Japan. [5]Lehrstuhl für Angewandte Festkörperphysik, Ruhr-Universität Bochum, Universitätsstrasse 150, 44780 Bochum, Germany. [6]Institut Universitaire de France, 103 boulevard Saint-Michel, 75005 Paris, France.

©2011 Macmillan Publishers Limited. All rights reserved

of the applied voltage on the two gates controlling the two barriers of the quantum dot are shown in Fig. 2a, b. They demonstrate that the system can be tuned into a regime consisting of few electrons[15]. As expected, the charge degeneracy lines disappear when the barrier height between each dot and the reservoir is increased (corresponding to increasingly negative voltages V_b and $V_{b'}$). This also changes the position of the quantum-dot minimum and brings the electron closer to the 1D channel, to a position where a better transfer to SAW quantum dots is expected.

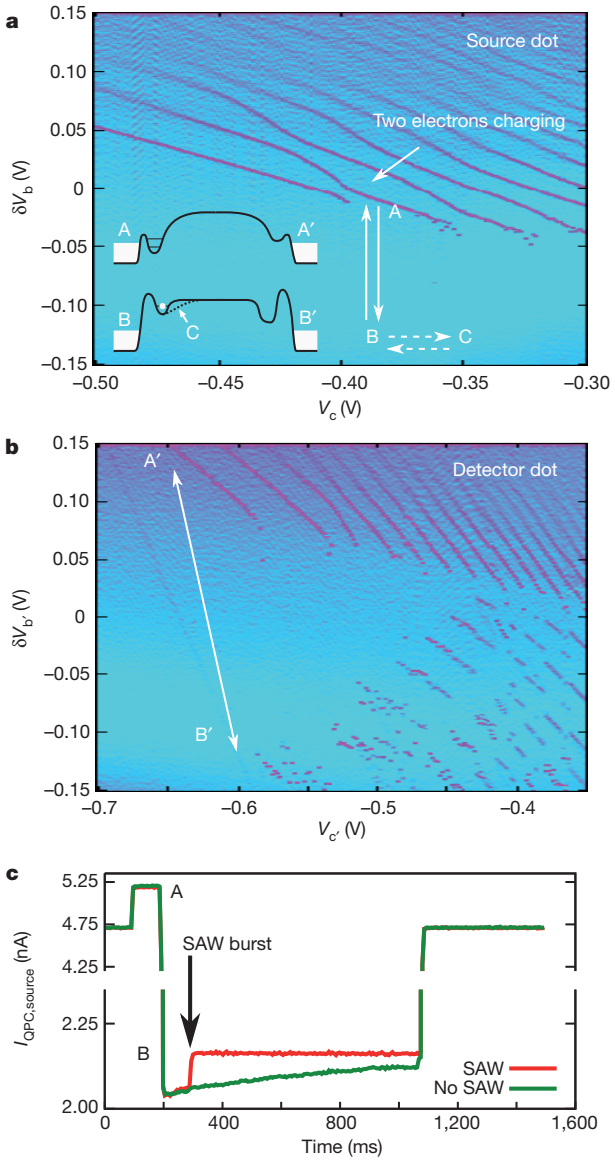

Figure 2 | Stability diagrams of the two quantum dots and charge detection. **a**, **b**, Stability diagram of the left (**a**) and right (**b**) dot obtained via charge detection by varying respectively gate voltages (V_b or V_c) and ($V_{b'}$ or $V_{c'}$) (see Fig. 1). Sweeps in V_b and $V_{b'}$ are fast and are performed within 1 s from +0.15 V to −0.15 V (3 ms per point). When the barrier height is made higher (V_b or $V_{b'}$ more negative), metastable charge states with timescales longer than the V_b or $V_{b'}$ sweep time are observed. In the very negative $V_{b'}$ part of the diagram for the right dot, the electrons will finally tunnel out. When the sweep direction of $V_{b'}$ is reversed, these charge detection steps are absent. Inset to **a**: schematic diagram of the dots and channel electrostatic potential applied by the gates to the electron at different points in the stability diagram (see the text). **c**, Average QPC time trace along the voltage sequence of the single-electron source. Without the microwave burst applied on the IDT, we observe a lifetime for the metastable one-electron charge state of 700 ms. Applying a microwave burst, the electron in the metastable state is forced to quit the quantum dot with very high probability.

The protocol of the single-electron source for a SAW quantum channel is a sequence made of three dot-gate voltage steps (see Fig. 2a). At working point A on Fig. 2a, the left quantum dot (the single-electron source) is loaded with one electron on a timescale close to microseconds and unresolved with the setup detection bandwidth. It is then brought rapidly to working point B, where the chemical potential of the single electron state lies above the Fermi energy and the coupling to the 1D channel is expected to be large. The actual position of B is not crucial as long as the electron is sufficiently protected from tunnelling out of the dot and the dot potential is high enough to facilitate the charging of the electron into the moving SAW dot (see inset to Fig. 2a). For each sequence, the quantum point contact (QPC) conductance time-trace is recorded to observe single-shot loading and unloading of the dot. This sequence is repeated 1,000 times to obtain measurement statistics; the resulting averaged time-traces are shown in Fig. 2c. An exponential decay of the presence of the electron in the dot as a function of the time spent at working point B is observed in the experimental data, corresponding to a tunnelling time close to 1 s as indicated by the green line. This gate pulsing sequence is then repeated by adding a burst of microwaves to the IDT with a pulse length of several tens of nanoseconds, applied 100 ms after the system is brought into position B. The microwave burst creates a moving quantum dot, which lifts the electron, initially trapped in the left quantum dot, above the tunnel barrier and drags it out of the quantum dot. This results in a jump in the QPC current, as shown by the red line.

To demonstrate that the electron has been loaded into a moving quantum dot and not expelled into the reservoir, it is essential to detect the coincidence between events when the electron leaves the single-electron source (left dot) and when it is trapped in the single-electron detector (right dot). This is realized by a second voltage pulse sequence on the right dot: when the single-electron source is brought in position B, the detector dot is armed by pulsing its gates to working point B′, where the steady state is the zero-electron state and the coupling to the channel is large. At this working point both QPC traces are recorded simultaneously. No charge variation is observed during the first 50 ms where the system is kept in position B. A microwave pulse is sent with a time lag of 50 ms. After the recording, the detector is reinitialized to zero electron at working point A′, where the captured electron can tunnel efficiently into the reservoir. Typical single-shot readout curves are presented in Fig. 3a–d. Coincidences are observed between events when an electron leaves the source quantum dot and an electron is detected in the receiver quantum dot within the same time slot (Fig. 3a). These events correspond to the situation in which one electron has been loaded in the electron source (left dot), is then transferred in the quantum channel (the moving quantum dots) and is received in the detector (right dot). In contrast with photon detectors, here the electron still exists after detection. A set of experiments described in Fig. 3 allows the full characterization of the high quantum efficiency of both the single-electron source and the single-electron detector observed in the experiment: 96% for the single-electron source and 92% for the single-electron detector (see Fig. 3e).

In quantum dots it is possible to load not just one but two electrons. By waiting long enough[16], the two electrons will be in a singlet state at zero magnetic field and are hence entangled in the spin degree of freedom. The ability to separate the two electrons and to bring only one of them to the second quantum dot is of potential interest for the transfer of quantum information and is the essence of the quantum teleportation protocol[2,17–19]. By analogy with photons, this is the equivalence of a two-photon entangled source[20]. Moreover, in contrast with a photon detector, the electron detector can discriminate easily whether one, two or more electrons have left the single-electron source and are captured in the single-electron detector (see Fig. 2a). The protocol consists of loading the left dot with exactly two electrons by moving gate voltages V_b and V_c into the two-electron regime of the stability diagram. The quantum dot is then tuned towards the working point where loading of the moving quantum dots is possible (point B).

©2011 Macmillan Publishers Limited. All rights reserved

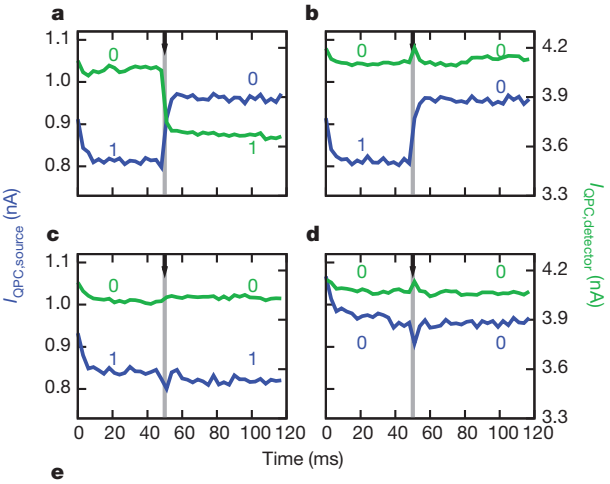

e

Event	SAW On	SAW Off	SAW On	SAW On	SAW On
N_{1xxx}	9,841	10,001	16	5,154	1,462
N_{10xx}	9,408 (95.6%)	0 (0%)	15 (94%)	4,954 (96.1%)	1,395 (95.4%)
N_{100x}	9,128	0	14	4,807	1,349
N_{1001}	8,393 (91.9%)	0 (0%)	14 (100%)	4,417 (91.9%)	1,244 (92.2%)
$\Sigma N_{\alpha\beta\gamma\delta}$	0	1	0	0	0

Figure 3 | Coincidence between emission and detection of a single electron. **a–d**, Coincidence between the two single-shot QPC time traces at voltage working points B and B′ corresponding to the different events N_{1001} (**a**), N_{1000} (**b**), N_{1100} (**c**) and N_{0000} (**d**). The position in time of the RF burst is indicated by the black arrow. At this specific time, the small peak or dip observed on time traces is the result of the SAW-induced enhancement or reduction, respectively, of the QPC current. The notation $N_{\alpha\beta\gamma\delta}$ corresponds to the number of events with α or β electrons in the source dot before or after the microwave burst, respectively, and to γ or δ electrons in the receiver dot before or after the microwave burst, respectively. When one index is replaced by x, the corresponding output result is disregarded. Event N_{1000} corresponds to the situation in which the electron has been transferred from the source to the detector and is immediately kicked out of the detector dot by the same RF burst and is therefore not detected. Events for which $\beta + \delta > \alpha + \gamma$ are called 'bad' events. **e**, Summary table for the different events over 10,001 traces for different source dot loading probabilities (N_{1xxx}) with or without the RF burst. The loading probability can be tuned on demand by changing the voltage gate position A in the stability diagram around the charge degeneracy point. The summation at the bottom table is for $(\beta + \alpha) > \delta + \gamma$.

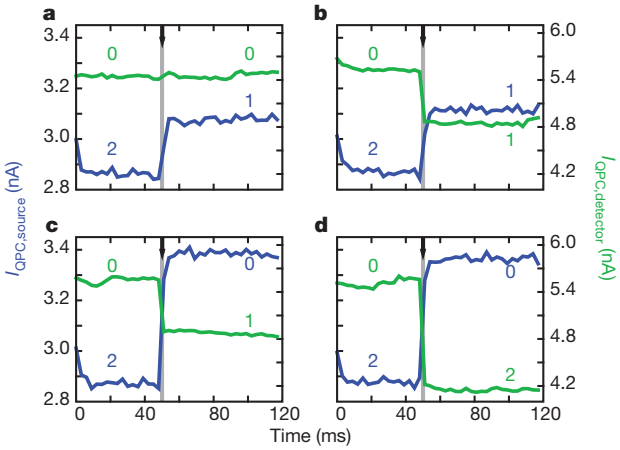

e

Event	V_c (mV) −388	V_c (mV) −322
N_{21xx}	445 (44.3%)	970 (96.5%)
N_{2101}	443 (99.6%)	878 (90.5%)
N_{20xx}	558 (55.5%)	30 (3%)
N_{2001}	62 (11%)	4 (13%)
N_{2002}	496 (88.9%)	26 (87%)

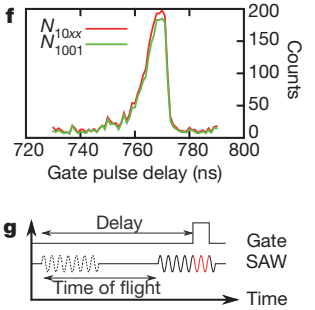

Figure 4 | Coincidence between emission and detection of two electrons and triggered nanosecond electron transfer. **a–d**, Coincidence between the two single-shot QPC time traces at voltage working points B and B′ corresponding to the different events N_{2100} (**a**), N_{2101} (**b**), N_{2001} (**c**) and N_{2002} (**d**). **e**, Summary table of the different events over 1,005 traces for dot configurations $V_c = -0.388$ V and $V_c = -0.322$ V. **f**, Evolution of the number of N_{1001} and N_{10xx} events as a function of the delay between the 1-ns gate pulse and the 65-ns microwave burst when a single electron is loaded into the single-electron source. **g**, Schematic diagram of the timing sequence between the 1-ns gate pulse and the microwave burst applied to the IDT.

Different possibilities for the emission of electrons into the quantum channel are observed. Indeed, when starting with exactly two electrons in the source dot, one can achieve the outcome that either exactly one or both electrons are emitted from the source and received in the detector dot, as shown by the single-shot traces for QPC detection of the two dots (see Fig. 4a–d). The probability of each event varies with the working voltage at point B. For very negative gate voltage V_c, about half of the time the two electrons are separated, meaning that only one electron is transferred, and the other half of the time both electrons are transported (see Fig. 4e). For the events in which both electrons leave the dot, the electrons are most probably loaded into two different moving quantum dots. More interestingly, when pulsing gate voltage V_c more positively, a situation can be realized in which only one of the two electrons of the left dot is efficiently emitted and consequently captured by the right dot (see Fig. 4e). In this case, the probability of sending the two electrons is markedly reduced, to less than 3%, and the probability of effectively separating the two electrons approaches 90%.

To use single-electron transfer in quantum operations using spin qubits, one has to show that coherence of the electron spin after electron transfer is preserved. Measurement and coherent manipulations of electron spins can be straightforwardly implemented in our setup, and the spin coherence time T_2* of an ensemble of electrons stored in SAW-assisted moving quantum dots has been shown to be as long as 25 ns (ref. 21). A necessary condition for investigating coherent transport of a single electron spin is to be able to trigger the electron transfer within a timescale that is short compared with T_2*. Indeed, a microwave pulse 250 ns in duration corresponds to about 700 moving quantum dots, and the experiments described above demonstrate the ability to load the electron into one of the moving quantum dots produced by each SAW microwave burst. We now show that the number of minima of the microwave burst in which the electron is loaded can be reduced to two. For this purpose, the single-electron source voltage sequence is slightly modified. After charging of the quantum dot, the system is brought to position B (see Fig. 2a) slightly on the more negative side with respect to V_c, and the duration of the microwave pulse is shortened to a minimum of 65 ns. At this voltage position, the barrier height to the quantum channel is increased and the transfer probability of an electron into the quantum channel is as low as 5% when excited with the SAW microwave burst. To trigger single-electron transfer, a 1-ns voltage pulse on V_c with a positive value (voltage position C in Fig. 2a) is added to this sequence. In Fig. 4f the evolution of the number of events in which one electron leaves the single-electron source and one electron is detected in the single-electron detector (N_{1001}) is plotted as a function of the delay between the 1-ns gate pulse and the 65-ns microwave burst. High transfer probabilities reaching 90% are observed only for time delays of roughly 765 ns, corresponding to the propagation time of the surface acoustic wave from the IDT to the dot region. Taking into account the pulse

©2011 Macmillan Publishers Limited. All rights reserved

length of the gate and the distance between two minima of the SAW, only two moving quantum dots can then be the hosts of the transported electron during the gate pulse, as indicated schematically in Fig. 4g. This demonstrates the ability to load on demand and in a very reproducible manner one of the two minima of the train of moving quantum dots with a single electron during the 1-ns gate pulse. The use of a faster arbitrary waveform generator should allow the electron to be loaded on demand into the same moving quantum dot.

These experiments represent the first milestone on the road to a new experimental platform for realizing quantum optics with flying electrons implemented in gated 2DEG heterostructures and transported by surface acoustic waves. High quantum efficiency of both the single-electron detector and the single-electron source are shown and potentially enable the measurement of all moments of the electron correlations[22]. In comparison with other implementations in similar systems, the propagating electron is physically isolated from the other conduction electrons of the heterostructure. In bringing together two propagating quantum buses separated by a tunnel barrier, a beam splitter for flying electrons can be implemented[23,24] and Hanbury Brown and Twiss-type experiments in which there are stronger Coulomb interactions between electrons could be realized. Future experiments should allow coherent spin transfer and provide new insight into the feasibility of quantum teleportation protocols and on the potential scalability of spin qubits.

METHODS SUMMARY

The device is defined by Schottky gates in an n-AlGaAs/GaAs 2DEG-based heterostructure (the properties of the 2DEG are as follows: $\mu \approx 10^6\,\mathrm{cm^2\,V^{-1}\,s^{-1}}$, $n_s \approx 1.4 \times 10^{11}\,\mathrm{cm^{-2}}$, depth 90 nm) with standard split-gate techniques. The charge configuration of both dots is measured by means of the conductance of both QPCs by biasing it with a direct-current voltage of 300 μV; the current is measured with a current-to-voltage converter with a bandwidth of 1.4 kHz. The voltage on each gate can be varied on a timescale down to microseconds. In addition, the gate biased with voltage V_c, controlling the coupling between the left dot and the 1D channel, is connected to a homemade bias tee to allow nanosecond manipulation of the dot potential by means of an arbitrary function generator (Tektronix AWG 5014). The IDT, which is placed about 2 mm to the left of the sample, is made of 70 pairs of lines 70 μm in length and 250 nm in width with a 1-μm spacing. The IDT is orientated perpendicular to the direction of the 1D channel defined along the crystal axis [110] of the GaAs wafer; it has a frequency bandwidth of about 20 MHz.

Received 26 April; accepted 4 August 2011.

1. Aspect, A., Grangier, P. & Roger, G. Experimental tests of realistic local theories via Bell's theorem. *Phys. Rev. Lett.* **47,** 460–463 (1981).
2. Bouwmeester, D. *et al.* Experimental quantum teleportation. *Nature* **390,** 575–579 (1997).
3. Neder, I. *et al.* Interference between two indistinguishable electrons from independent sources. *Nature* **448,** 333–337 (2007).
4. Henny, M. *et al.* The fermionic Hanbury Brown and Twiss experiment. *Science* **284,** 296–298 (1999).
5. Liu, R. C., Odom, B., Yamamoto, Y. & Tarucha, S. Quantum interference in electron collision. *Nature* **391,** 263–265 (1998).
6. Petta, J. R. *et al.* Coherent manipulation of coupled electron spins in semiconductor quantum dots. *Science* **309,** 2180–2184 (2005).
7. Splettstoesser, J., Ol'khovskaya, S., Moskalets, M. & Büttiker, M. Electron counting with a two-particle emitter. *Phys. Rev. B* **78,** 205110 (2008).
8. Fève, G. *et al.* An on-demand coherent single-electron source. *Science* **316,** 1169–1172 (2007).
9. Field, M. *et al.* Measurements of Coulomb blockade with a noninvasive voltage probe. *Phys. Rev. Lett.* **70,** 1311–1314 (1993).
10. Ji, Y. *et al.* An electronic Mach–Zehnder interferometer. *Nature* **422,** 415–418 (2003).
11. Roulleau, P. *et al.* Direct measurement of the coherence length of edge states in the integer quantum Hall regime. *Phys. Rev. Lett.* **100,** 126802 (2008).
12. Talyanskii, V. I. *et al.* Single-electron transport in a one-dimensional channel by high-frequency surface acoustic waves. *Phys. Rev. B* **56,** 15180–15184 (1997).
13. Koppens, F. H. L. *et al.* Driven coherent oscillations of a single electron spin in a quantum dot. *Nature* **442,** 766–771 (2006).
14. Bluhm, H. *et al.* Dephasing time of GaAs electron-spin qubits coupled to a nuclear bath exceeding 200 μs. *Nature Phys.* **7,** 109–111 (2011).
15. Buks, E., Schuster, R., Heiblum, M., Mahalu, D. & Umansky, V. Dephasing in electron interference by a 'which-path' detector. *Nature* **391,** 871–874 (1998).
16. Meunier, T. *et al.* Experimental signature of phonon-mediated spin relaxation in a two-electron quantum dot. *Phys. Rev. Lett.* **98,** 126601 (2007).
17. Barrett, M. D. *et al.* Deterministic quantum teleportation of atomic qubits. *Nature* **429,** 737–739 (2004).
18. Riebe, M. *et al.* Deterministic quantum teleportation with atoms. *Nature* **429,** 734–737 (2004).
19. Nielsen, M. A. & Chuang, I. L. *Quantum Computation and Quantum Information* (Cambridge Univ. Press, 2000).
20. Stevenson, R. M. *et al.* A semiconductor source of triggered entangled photon pairs. *Nature* **439,** 179–182 (2006).
21. Stotz, J. A. H., Hey, R., Santos, P. V. & Ploog, K. H. Coherent spin transport through dynamic quantum dots. *Nature Mater.* **4,** 585–588 (2005).
22. Gustavsson, S. *et al.* Counting statistics of single-electron transport in a quantum dot. *Phys. Rev. Lett.* **96,** 076605 (2006).
23. del Alamo, J. & Eugster, C. C. Quantum field-effect directional coupler. *Appl. Phys. Lett.* **56,** 78–80 (1990).
24. Tsukada, N., Wieck, A. D. & Ploog, K. Proposal of novel electron wave coupled devices. *Appl. Phys. Lett.* **56,** 2527–2529 (1990).

Supplementary Information is linked to the online version of the paper at www.nature.com/nature.

Acknowledgements We thank Y. Launay and P. Perrier for technical support. We acknowledge technical support from the 'Pôles Électroniques' of the 'Départment Nano et MCBT' from the Institut Néel. M.Y. acknowledges financial support by Grant-in-Aid for Young Scientists A (no. 20684011) and ERATO-JST (080300000477). S.T. acknowledges financial support from Special Coordination Funds for Promoting Science and Technology (NanoQuine), Japan Science and Technology Agency Strategic International Cooperative Program, Japanese Ministry of Education, Culture, Sports, Science, and Technology KAKENHI 'Quantum Cybernetics', and Intelligence Advanced Research Projects Activity project 'Multi-Qubit Coherent Operations' through Harvard University. A.D.W. acknowledges expert help from D. Reuter and support of the Deutsche Forschungsgemeinschaft (SPP1285) and the Bundesministerium für Bildung und Forschung (QuaHLRep 01BQ1035). C.B. acknowledges financial support from Centre National de la Recherche Scientifique (DREI) – Japan Society for the Promotion of Science (nos PRC 424 and L08519). T.M. acknowledges financial support from Marie-Curie European Reintegration Grant 224786. We are grateful to the Nanoscience Foundation of Grenoble for partial financial support of this work.

Author Contributions S.H. and T.M. conceived and performed the experiments and analysed the data. Sh.T., M.Y. and S.T. were in charge of the sample fabrication and early stages of the experiment. A.D.W. performed the molecular beam epitaxy growth of the high-mobility GaAs/AlGaAs heterostructure. C.B and T.M. wrote the manuscript. All authors contributed to the manuscript and discussed the results extensively.

Author Information Reprints and permissions information is available at www.nature.com/reprints. The authors declare no competing financial interests. Readers are welcome to comment on the online version of this article at www.nature.com/nature. Correspondence and requests for materials should be addressed to C.B. (bauerle@grenoble.cnrs.fr) or T.M. (tristan.meunier@grenoble.cnrs.fr).

©2011 Macmillan Publishers Limited. All rights reserved

Abstract

A global effort is pursued to realise a quantum computer. Such a device will allow to implement faster algorithms for tasks like integer factoring and database search. It will also allow to simulate quantum system much more efficiently than a classical system. This power gain necessitates to entangle a large number of qubits. This in turn requires the ability to transport a qubit in space. In this thesis, we demonstrate a first step: a single electron is transported on demand from one quantum dot to another quantum dot, micrometers away. The transport is realised thanks to a Surface Acoustic Wave (SAW) that drags the electron. The transfer is realised with an efficiency of 90 % and triggered within one nanosecond. These results open the way to the realisation of electron quantum optics experiments with an event per event detection. A work on the separation of two electron initially present in the quantum dot will lead to the generation of distant entangled particles.

Résumé

Un effort mondial existe actuellement dans le but de réaliser un ordinateur quantique. Un tel dispositif permettrait d'implémenter des algorithmes plus rapides que les algorithmes classiques pour certaines tâches (recherche dans des bases de données, factorisation d'entiers). Il permettrait également de simuler des systèmes quantiques de manière beaucoup plus efficace qu'un ordinateur classique. L'obtention de ce gain en puissance nécessite d'intriquer un grand nombre de bits quantiques (qubits). Celle ci suppose de pouvoir déplacer un qubit d'un point à un autre de l'espace. Dans cette thèse, nous démontrons une première étape vers le déplacement d'un qubit de spin électronique : un électron unique est déplacé, à la demande, entre deux boîtes quantiques distantes de quelques microns. Le transport est réalisé à l'aide d'une onde acoustique de surface qui entraîne l'électron. Le transfert a été réalisé avec une efficacité de 90 Ces résultats ouvrent la voie à la réalisation d'expériences d'optique quantique électronique avec une détection évènement par évènement. L'envoi d'un électron sur deux initialement présents ouvre la voie à la génération de paires d'électrons distants et intriqués.